CENTRO FEDERAL DE EDUCAÇÃO TECNOLÓGICA DE MINAS GERAIS
PROGRAMA DE PÓS-GRADUAÇÃO EM ENGENHARIA ELÉTRICA

ANALYSIS OF RESONANT WIRELESS POWER TRANSFER SYSTEMS WITH MAGNETIC METASURFACE LENSES

ÍCARO VELOSO SOARES

Orientadora: Profª. Drª. Úrsula do Carmo Resende

BELO HORIZONTE
AGOSTO DE 2020

ÍCARO VELOSO SOARES

ANALYSIS OF RESONANT WIRELESS POWER TRANSFER SYSTEMS WITH MAGNETIC METASURFACE LENSES

Dissertação apresentada ao Programa de Pós-graduação em Engenharia Elétrica do Centro Federal de Educação Tecnológica de Minas Gerais, como requisito parcial para a obtenção do título de Mestre em Engenharia Elétrica.

Área de concentração: Sistemas Elétricos.

Linha de pesquisa: Eletromagnetismo Aplicado.

Orientadora: Profª. Drª. Úrsula do Carmo Resende

CENTRO FEDERAL DE EDUCAÇÃO TECNOLÓGICA DE MINAS GERAIS
PROGRAMA DE PÓS-GRADUAÇÃO EM ENGENHARIA ELÉTRICA
BELO HORIZONTE
AGOSTO DE 2020

Soares, Ícaro Veloso
S676a Analysis of resonant wireless power transfer systems with magnetic metasurface lenses / Ícaro Veloso Soares. – 2020.
xii, 97 f.: il., gráfs, tabs., fotos.

Dissertação de mestrado apresentada ao Programa de Pós-Graduação em Engenharia Elétrica em associação ampla entre a UFSJ e o CEFET-MG.
Orientadora: Úrsula do Carmo Resende.
Banca examinadora: Úrsula do Carmo Resende, Sandro Trindade Mordente Gonçalves, Elson José da Silva.
Dissertação (mestrado) – Centro Federal de Educação Tecnológica de Minas Gerais.

1. Campos elétricos – Teses. 2. Equações – Soluções numéricas – Teses. 3. Linhas de transmissão de microondas – Teses. 4. Metamateriais – Teses. 5. Dispositivos eletromagnéticos – Teses. I. Resende, Úrsula do Carmo. II. Centro Federal de Educação Tecnológica de Minas Gerais. III. Universidade Federal de São João del-Rei. IV. Título.

CDD 621.34

Elaboração da ficha catalográfica pela bibliotecária Jane Marangon Duarte, CRB 6ª 1592 / Cefet/MG

UNIVERSIDADE FEDERAL DE SÃO JOÃO DEL REI
PRÓ-REITORIA DE PESQUISA E PÓS-GRADUAÇÃO

CENTRO FEDERAL DE EDUCAÇÃO TECNOLÓGICA DE MINAS GERAIS
DIRETORIA DE PESQUISA E PÓS-GRADUAÇÃO

PROGRAMA DE PÓS-GRADUAÇÃO EM ENGENHARIA ELÉTRICA

Ícaro Veloso Soares

"Analysis of Resonant Wireless Power Transfer Systems with Metamaterial Lenses through the Method of Moments."

Dissertação nº 238 apresentada ao Programa de Pós-Graduação em Engenharia Elétrica – Associação Ampla entre a Universidade Federal de São João Del-Rei e o Centro Federal de Educação Tecnológica de Minas Gerais em 10 de Agosto de 2020 como requisito parcial para obtenção do título de Mestre em Engenharia Elétrica, aprovada pela Banca Examinadora constituída pelos professores:

Profª. Drª. Úrsula do Carmo Resende (Orientadora)
Centro Federal de Educação Tecnológica de Minas Gerais

Prof. Dr. Sandro Trindade Mordente Gonçalves
Centro Federal de Educação Tecnológica de Minas Gerais

Prof. Dr. Elson José da Silva
Universidade Federal de Minas Gerais – UFMG

This work is dedicated to all the masters that guided me into the light of science and knowledge.

Acknowledgements

I would like to express my deepest gratitude to God, Light of light, from Whom all things come from and in Whom all things converge.

To my parents, Valdemar and Zulma, for their support and dedication, and for having taught me that it is worth believing in my dreams and fighting for them. They are, to me, examples of the virtues that make a good researcher: dedication, patience, humbleness, and perseverance.

To my advisor, Prof. Dr. Úrsula do Carmo Resende. To me, it is an honour and a blessing to work with such dedicated, caring and hard-working professional. More than an advisor, she is a motivation and inspiration for me. I am looking forward to collaborating and researching together in many future projects.

To Felipe Machado, for his friendship, partnership, optimism, strength and patience. His presence and his help were extremely important in this work, and without him, this work would not be possible.

To my friends and colleagues, who are part of my human and professional journey. In special to Guilherme Brandão, for all the help and collaboration.

To the CEFET-MG, my *alma mater*, that has been my second home for the past twelve years. To me, to be part of this institution is like a dream that came true. I am grateful for having allowed me to use all its infrastructure, offering free and high-quality public education. To its professors who, throughout different academic levels, share their knowledge and experiences. And to the university staff, for always being willing to help.

To the IBBx Inovação, for changing the industrial paradigm in Brazil by focusing on research and development, encouraging the initiative of its collaborators, and for giving me the conditions to develop this work.

To the IEEE Magnetic Society for sponsoring the presentation of this project in the 2019 Magnetics Society Summer School.

To CNPq, CAPES and FAPEMIG, for promoting the scientific research in Brazil and Minas Gerais, and for partially supporting this project.

"The particles of light can exhibit different characteristics depending on the speed and the arrangements of the tejas *(fire) atoms."*
Vaisheshika - ancient Indian philosophic school (6th-5th century BC)

Resumo

Das várias técnicas existentes para transferência de energia sem fio, uma das mais eficientes em termos de faixa de potência e distância é por ressonância magnética. Nesta técnica, as bobinas transmissora e receptora são acopladas indutivamente, e esse acoplamento é intensificado quando ambas estão sintonizadas na mesma frequência de ressonância. Uma maneira de aumentar a eficiência da transferência de energia e também de controlar a direção do campo magnético é utilizando lentes metamateriais capazes de superar o limite de difração. Nestes materiais engenheirados, as propriedades eletromagnéticas efetivas são funções da composição química e do arranjo geométrico das células unitárias que os compõem.

A análise da transferência de energia sem fio ressonante com lentes metamateriais é um problema complexo e computacionalmente dispendioso. Portanto, neste trabalho, uma abordagem alternativa para a análise qualitativa dessas estruturas é proposta aplicando a aproximação de fio fino e sua solução numérica através do Método dos Momentos. Além disso, a técnica de Óptica Transformacional é aplicada para determinar o perfil do índice de refração de uma lente metamaterial que conduz à desejada colimação de campo magnético.

Dessa forma, diferentes lentes metassuperficiais magnéticas são projetadas e seu comportamento é verificado computacional e experimentalmente. Finalmente, sistemas de transferência de energia sem fio ressonante de duas e quatro bobinas são projetados, construídos e testados com e sem a inclusão de lentes metamateriais.

Palavras-chave: Equações Integrais de Campo Elétrico, Lentes Metamateriais, Método dos Momentos, Transferência de Energia sem Fio Ressonante, Aproximação de Fio Fino, Óptica Transformacional.

Abstract

From the various existing techniques to wirelessly transfer energy, one of the most efficient in terms of power and distance range is through magnetic resonance. In this technique, the transmitter and receiver coils are inductively coupled, and this coupling is intensified when both coils are tuned at the same resonant frequency. One way to enhance the power transfer efficiency and also to control the magnetic field direction is by applying metamaterial lenses which are able to overcome the diffraction limit. In this engineered material, the effective electromagnetic properties are functions of the chemical composition and geometrical arrangement of the unit cells that compose it.

The analysis of a resonant wireless power transfer with metamaterial lenses is a complex and computationally costly problem. Therefore, in this work, an alternative approach for the qualitative analysis of these structures is proposed by applying the thin-wire approximation and its numerical solution through the Method of Moments. In addition, the Transformation Optics technique is applied to determine the refractive index profile of a metamaterial lens that leads to a desired magnetic field collimation.

In this way, different magnetic metasurface lenses are designed, and their behaviour is computationally and experimentally verified. Finally, two-coil and four-coil resonant wireless power transfer systems are designed, built and tested with and without the inclusion of metamaterials lenses.

Keywords: Electric Field Integral Equations, Metamaterial Lenses, Method of Moments, Resonant Wireless Power Transfer, Thin-wire Approximation, Transformation Optics.

List of Figures

List of Tables

Contents

1 Introduction

1.1 Background

The seminal work that unified the laws of electricity and magnetism presented by James Clerk Maxwell in 1873, the mathematical modelling of the energy propagation dynamics by electromagnetic fields published by John Henry Poynting in 1884 and the Hertz's experiments from 1885 to 1889, that proved their theory and presented a way of transmitting and receiving electromagnetic waves, are the fundamental scientific developments that made wireless technology possible. Even though it has been mainly focused on communications, this technology also opens up a possibility to transmit and receive energy through electromagnetic waves propagating in the space. Nikola Tesla was the first engineer to propose and to develop an apparatus to transmit energy wirelessly. However, it was only after the second half of the 20^{th} century that this concept started to be further investigated.

For the past 20 years, there has been a remarkable increase in the number of publications and patents related to wireless power transfer. The evolution of electronics that enabled the design of ultra-low-power devices, the modern techniques of applied electromagnetism that led to the physical realization of materials with properties that were not found in nature, and the boost in the computational capacity of processors that favours high-performance computer-aided designs and high-precision simulations can be listed as some of the main factors that allowed this fast development. In addition to them, the concept of Internet of Things (IoT) with many electronic devices and sensors connected in a network applied for both industrial and consumer electronics makes wireless energy not only a desire but a requirement for its full establishment.

Wireless Power Transfer (WPT) is the technology that applies time-varying electromagnetic fields as an energy carrier from a transmitter to a receiver, without using wired and physical connections. Although this definition is straightforward, different techniques embody this concept, and the application of each one depends on the requirements of the project such as frequency, power level, transmission distance range, among others. The flowchart in Figure 1.1 presents a classification of the main WPT techniques. Firstly, they can be divided into two groups: near-field or non-radiative techniques and far-field or radiative techniques (HOURAN; YANG; CHEN, 2018).

The radiative techniques are applied when the distance range is larger than the wavelength, and the load at the receiver does not affect the transmitter characteristics. There are three main approaches to this technique: microwave power transfer, laser power

transfer and solar power transfer. The size of antennas used for WPT in the microwave band is generally in the order of the wavelength. Moreover, it is preferred to use highly directive antennas in order to reduce the amount of energy dispersed into space and thus, increase the power transfer efficiency (SONG; BELOV; KAPITANOVA, 2017). Another method is to apply high-intensity laser beams to transmit high power level; however, its efficiency is firmly dependent on the alignment between transmitter and receiver, that must be in line-of-sigh (JIN; ZHOU, 2019). Another technique that has been investigated is by using solar panels installed in satellites that orbit the Earth. In these satellites, the collected energy is transferred to a terrestrial base through a high power microwave beam (CHAUDHARY; KUMAR, 2018). Although the radiative techniques allow WPT in large distances, most of them still have low efficiency and high installation complexity.

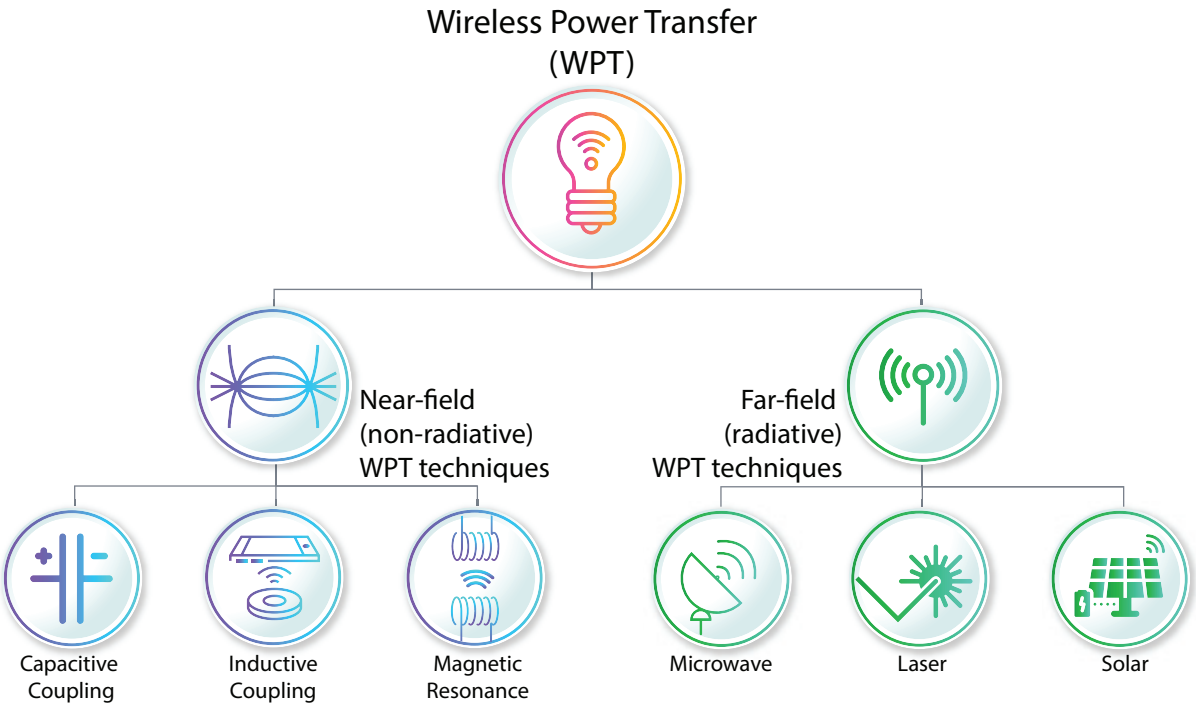

Figure 1.1 – Wireless Power Transfer main techniques classification.

On the other hand, the near-field or resonant techniques are applied when this distance between transmitter and receiver is much less than the wavelength and, in this case, the load impedance at the receiver affects the transmitter input impedance. In this technique, the power is transferred through the electric field in the capacitive coupling type or magnetic field in the inductive coupling. Both methods can achieve high power transfer levels as well as high efficiency, there being already various commercial applications. However, their efficiency sharply decreases with the separation between transmitter and receiver, and in most of the applications, this distance is not greater than a few centimetres .

To overcome this limitation, an alternative approach to wireless power transfer for mid-

range applications, that is, for applications in which the distance between transmitter and receiver is from two to five times the transmitter size, is called Magnetic Resonant Wireless Power Transfer, or directly, Resonant Wireless Power Transfer (RWPT). In this case, the coupling between transmitter and receiver is not only inductive, but it is also resonant, which allows stronger coupling even with higher separations (SHINOHARA, 2018).

Each one of these techniques has advantages and disadvantages that make them suitable or not depending on the nature and characteristics of the application. Therefore, in order to choose the appropriate approach to transfer power wirelessly, one must have an in-depth knowledge of the requirements and limitations of the application.

1.2 Scope

Due to the commercial appeal of mid-range wireless power transfer and the potentialities of the magnetic resonance technique, it has been investigated from different aspects by a vast number of research institutions, universities, and technology corporations. In this way, there are enhancement methods focused on electromagnetic analysis (BINGLER et al., 2019), power electronic circuits (PRIES et al., 2020), novel materials development (CORREA; RESENDE; BICALHO, 2019), control system (TAN et al., 2020), electromagnetic compatibility (CRUCIANI et al., 2019), among other fields.

An innovative approach that has gained visibility over time is the application of metamaterial structures for increasing the coupling between transmitter and receiver resonators in an RWPT system. This class of novel electromagnetic artificial materials presents remarkable properties that cannot be found in conventional structures, for instance, they can exhibit negative refractive index, perfect absorbing effects, and overcome the diffraction limit by collimating evanescent waves (PENDRY, 2000). Particularly for RWPT systems, this last phenomenon is used to focus the magnetic field from the transmitter to the receiver coil, enhancing the coupling between them, leading to higher efficiency levels (AHN; KIANI; GHOVANLOO, 2014).

Although the RWPT systems, with or without metamaterials, are generally simple from the constructive point of view, their design can be a challenging task. Basically, these systems are constituted by wire or microstrip coils connected to signal generators, power amplifiers, impedance matching networks, and rectifier circuits. Each stage of the system imposes its own complexities. Particularly, the computer-aided electromagnetic design of these coils and metamaterials is a computationally costly task, once it involves the meshing of large structures with small details, the presence of lumped elements, lossy materials, treatment of complex media, and the separation between the coils.

Even though nowadays different commercial software can be used to design these systems, each one applying different methods and being updated continuously with the most recent numerical techniques, the computational simulation and optimisation of the entire RWPT system still is a time-consuming task even with a computer with high computational capability.

In this scope, the present work proposes an alternative approach to the analysis and the design of printed RWPT systems and metamaterial lenses for this application, by applying numerical methods and approximations in order to reduce the computational complexity and the processing time.

1.3 Objectives

This work initiates a broader project of numerical modelling of RWPT devices and magnetic metasurface lenses. Therefore, as a starting point, the objective of this work is to explore theoretically, computationally, and experimentally the characteristics of these structures, which permits to identify the challenges and to define the subsequent steps of this project. For this reason, it is not sought in this work a fully quantitative numerical model, rather than that, the analysis and models proposed in this work allows a qualitative description of these structures which corroborates with the results from the experiments performed.

Several secondary aims allow achieving the primary goal:

- First, a literature review focused on RWPT systems must be conducted in order to characterise and comprehend all factors that affect the efficiency of this technique as well as the enhancement methods proposed in the literature;
- Then, a mathematical model that accounts for the dynamic of electromagnetic fields must be proposed, considering the characteristics of thin microstrip structures and the presence of lumped elements. All the aspects regarding the computational implementation of the proposed model shall be described as well as evaluated through parametric analysis of its main numerical parameters. Besides, the accuracy and validity range of the proposed model must be defined by comparison with commercial software results and experimental measurements;
- Furthermore, the effects of metamaterial lenses in RWPT systems must be analysed. To this end, a literature review must be carried out, and a design guideline must be developed, taking into account the characteristics of the magnetic resonant coupling to achieve a converging and diverging field manipulation. Finally, the electromagnetic behaviour of these structures must be qualitatively analysed with the proposed numerical implementation;
- Afterwards, an extensive experimental analysis of an RWPT system prototype

shall be performed in order to validate the proposed electromagnetic model and the metamaterial lens design approach. Finally, based on all the analysis developed from the results obtained, improvements must be indicated as well as future works subsequent to this one.

1.4 Methodology

As a starting point for the efficiency analysis of RWPT systems, a literature review is carried out, and the circuit model for two-coil and four-coil RWPT systems are presented to elucidate the main characteristics of these systems as well as the main factor that affects the RWPT efficiency. Then, this model is used to motivate the efficiency enhancement by the effective magnetic permeability manipulation.

However, as the circuit model is not able to describe all electromagnetic interactions between the RWPT structures and the metamaterial lenses, a mathematical model and its numerical implementation are proposed. In general, RWPT systems and metamaterial structures have much smaller sizes than the wavelength at their operating frequency. They are formed by thin wire or thin microstrip coils with their cross-section much shorter than their length. These two characteristics motivate the application of thin wire approximation for their electromagnetic analysis, which has already been applied for RWPT wire coils. However, due to the properties of the dielectric substrate and the rectangular cross-section of the conductive line, in order to use this approximation to thin microstrip structures, some adaptations must be proposed.

Based on these characteristics and requirements, in the present work, the integro-differential formulation in a tridimensional space is reduced to an unidimensional problem through the thin-wire approximation. Therefore, by applying the Method of Moments, the current along the wire can be numerically evaluated. This model and its implementation are then used for modelling thin microstrip structures by considering the RWPT resonators immerse in a homogeneous medium with an effective electric permittivity. In addition, the contribution of lumped impedances is included in the integro-differential formulation.

Then, the main theoretical aspects, as well as experimental characterisation methods for magnetic metasurface lenses, are investigated and proposed. Furthermore, to design the metamaterial lenses, the Transformation Optics technique is applied in order to find the unit cell arrangement that leads to the desired magnetic field collimation profile for a diverging and converging metasurface lens. Based on this technique, the lenses are optimised and qualitatively analysed with the proposed numerical implementation.

Finally, to validate the proposed electromagnetic model and to verify the behaviour

of the designed lenses, prototypes are built and experimentally evaluated through scattering parameters matrix and power transfer measurements. Based on these measurements, it is possible to characterise the RWPT system as well as the metasurface lenses. Moreover, different experiments and analysis are carried out to investigate the properties of RWPT system with metasurface lenses theoretically discussed in this work.

1.5 Outline

This dissertation is structured in the following way. In chapter 2, the main concepts regarding the RWPT system are presented as well as its efficiency, which is analysed through the circuit model for a two and four-coil system. All factors that affect this efficiency are studied, and the improvement techniques are presented. In the end, the basis of the efficiency enhancement with metamaterial resonators is presented.

Subsequently, in chapter 3, the integro-differential formulation for the problem under analysis is developed along with the thin wire approximation that simplifies this formulation and the inclusion of the lumped element contribution. Then, the aspects related to the computational implementation of the proposed method is discussed. At this point, the numerical results of thin wire formulation and implementation are evaluated and compared with the results obtained with a commercial electromagnetic simulator. After that, the model is extended to thin microstrip structures with the rectangular cross-section treatment and the inclusion of the dielectric properties through the multipole Debye model. Finally, the numerical results are validated with experimental measurements and simulations.

Chapter 4 is dedicated to the analysis of metamaterial lenses and their contribution to the RWPT efficiency enhancement. The mechanism of evanescent field collimation is studied, and the Transformation Optics technique is applied as a qualitative tool to determine the unit cell arrangement in converging and diverging lenses. Then, the magnetic metasurface lens prototypes are described and qualitatively analysed with the proposed numerical implementation.

Furthermore, chapter 5 presents the experimental setup description and the measured results of efficiency and power transfer obtained with two and four-coil prototypes, with and without metamaterial lenses, as well as the lenses experimental characterisation.

To summarise, the conclusion of the results discussed in the dissertation, the future works and improvement proposals, and the scientific publications produced during this project are presented in chapter 6.

2 Resonant Wireless Power Transfer

In this chapter, the definition of Resonant Wireless Power Transfer systems and the main conceptual aspects regarding this technology are presented. Then, using a two and four-coil system as case studies, their efficiencies are analysed as well as the factors that affect them, with particular attention to the frequency splitting phenomenon. Finally, the theoretical basis of the efficiency enhancement with the magnetic coupling strengthening caused by metamaterial resonators are discussed.

2.1 Definition of Resonant Wireless Power Transfer

In the vast majority of non-radiative WPT applications, the coupling between transmitter and receiver is magnetic in its nature, and the applied techniques, in this case, can be classified as Inductive Wireless Power Transfer (IWPT) and Resonant Wireless Power Transfer (RWPT). Even though both techniques have a similar operating principle behind, the way it is applied is fundamentally different.

In the IWPT technique, the time-varying current flowing in the transmitter coil generates an alternate magnetic flux that, in its turn, induces a time-varying current in the receiver coil, according to the Faraday's Law. This technique can also be understood as a transformer in which the air replaces the ferromagnetic-core (SONG; BELOV; KAPITANOVA, 2017). Therefore, the coupling between transmitter (primary) and receiver (secondary) coil is significantly lower in IWTP, and it decreases even more as the distance between both coils increases or if there is a misalignment between them. It is due to the fact that, operating in the reactive near-field region, there is not propagating modes, and the field has an evanescent character (ALMEIDA; FEITOZA, 2018). For this reason, IWPT is mostly applied in short-range applications, i.e., when the distance between transmitters and receivers is not greater than the size of the coils. However, this limitation does not preclude its application, and this technique has been applied in most of the commercial applications, such as wireless charging pads (LU et al., 2016), RFID tags (KIANI; GHOVANLOO, 2010), bio-implantable devices (LIN; TANG, 2016), among others.

On the other hand, in the RWPT technique the transmitter and receiver coils are themselves LC resonant circuits. It can be accomplished either through the inclusion of a lumped capacitance or by the self-capacitance of each coil (KURS et al., 2007). Thus, if both transmitter and receiver coil are resonant in the same frequency, the coupling between them is markedly increased, thus increasing power transfer efficiency.

The general structure of an RWPT system is shown in the block diagram presented in Figure 2.1 (SHINOHARA, 2018). It consists basically of two couplers, one for transmission and the other one for reception, both of them are coupled via the magnetic field. In order to achieve resonance, the inductive reactance of each coupler shall be compensated either through their self-capacitance or by a lumped capacitance added to the coupler. Therefore, a resonator can be defined as a coupler and its reactance compensating elements. The transmitting resonator is connected to a power generator that supplies the required power level at the system resonant frequency, whereas the receiving resonator is connected to the load. In both of them, a matching impedance network may be required to match the impedance of the resonator to the source or load impedance.

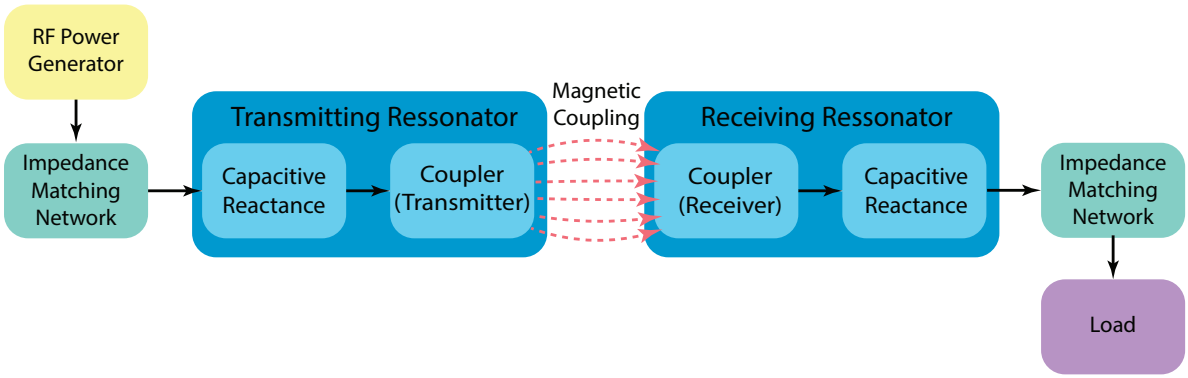

Figure 2.1 – General structure of an RWPT system.

Besides this general structure, RWPT can be physically implemented in different ways. In the most straightforward arrangement, two coils are used as indicated in Figure 2.2a, one for transmission and the other one for reception. However, the use of multiples coils has been proposed in order to increase efficiency (KACZMARCZYK et al., 2020). For instance, the most common multiple coil system employs four coils: the transmitting and receiving resonator coils which are coupled, and two other coils connected to them. This four-coil system is presented in Figure 2.2b. The driver coil makes the interface between the transmitting resonator and the power generator; and the sink coil, in its turn, the interface between the receiving resonator and the load (F.JOLANI; YU; CHEN, 2014). In addition to enhancing efficiency, the driver and sink coils can be designed to match the impedance of the resonators to the source and load, respectively besides assuring the isolation between them (ZHOU et al., 2018).

Moreover, different techniques of reactance compensation have been investigated. The primary compensation topologies are with the lumped capacitor connected in series or parallel to the transmitting and receiving coils, and the combinations between them as shown in Figure 2.3. However, hybrid structures based on different topologies of impedance matching networks are also employed. In all of them, the compensation

network is designed to achieve power factor minimization at the input, power transfer maximization at the output and the feeding requirements for the load, such as constant current or constant voltage (HOURAN; YANG; CHEN, 2018).

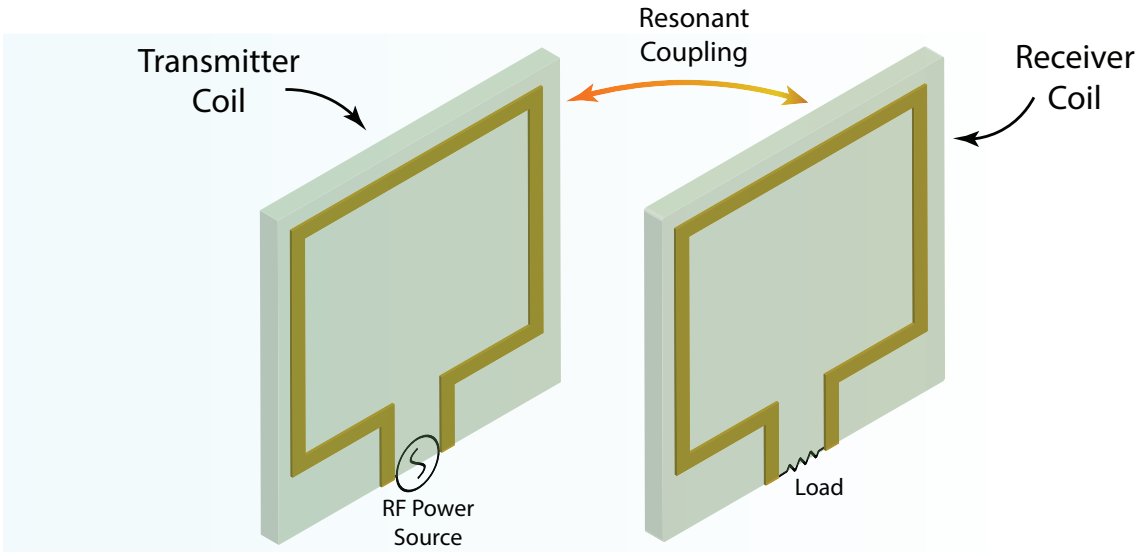

(a) Two-coil RWPT System.

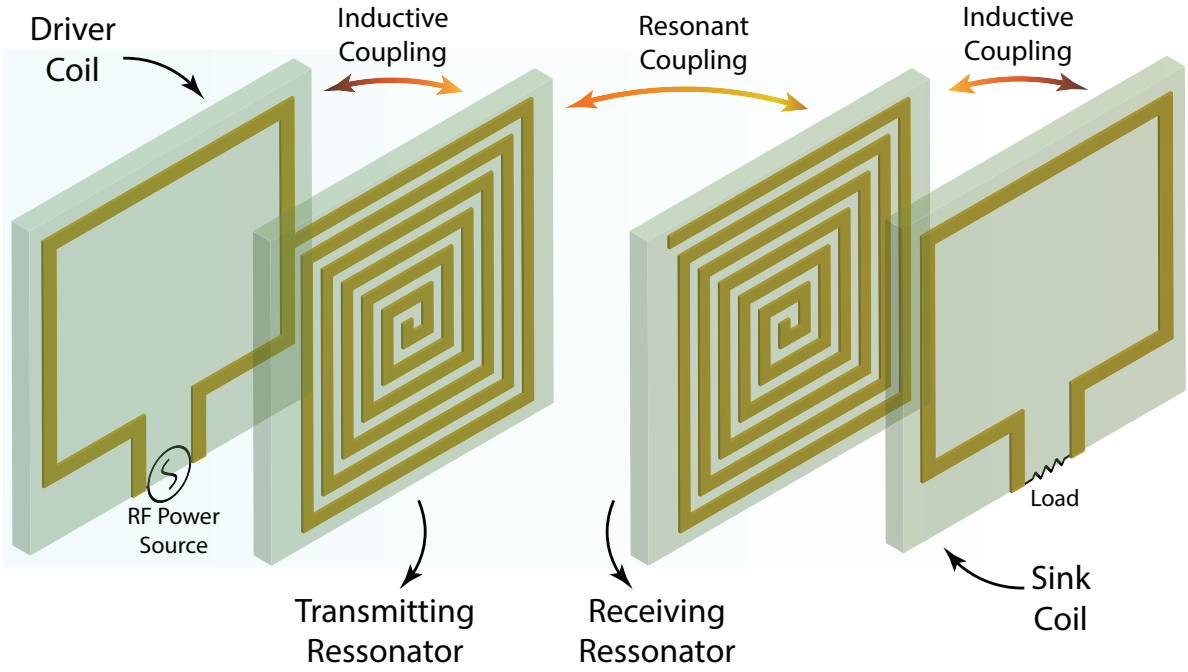

(b) Four-coil RWPT System.

Figure 2.2 – Physical implementations of the RWPT technique.

In the next section, the RWPT efficiency is modelled through its circuit model, and the factors that affect it are analysed. Even though the circuit model disregards many aspects of the interaction between electromagnetic fields, it is able to elucidate the overall RWPT principle of operation, and it can be used as a starting point for the system design.

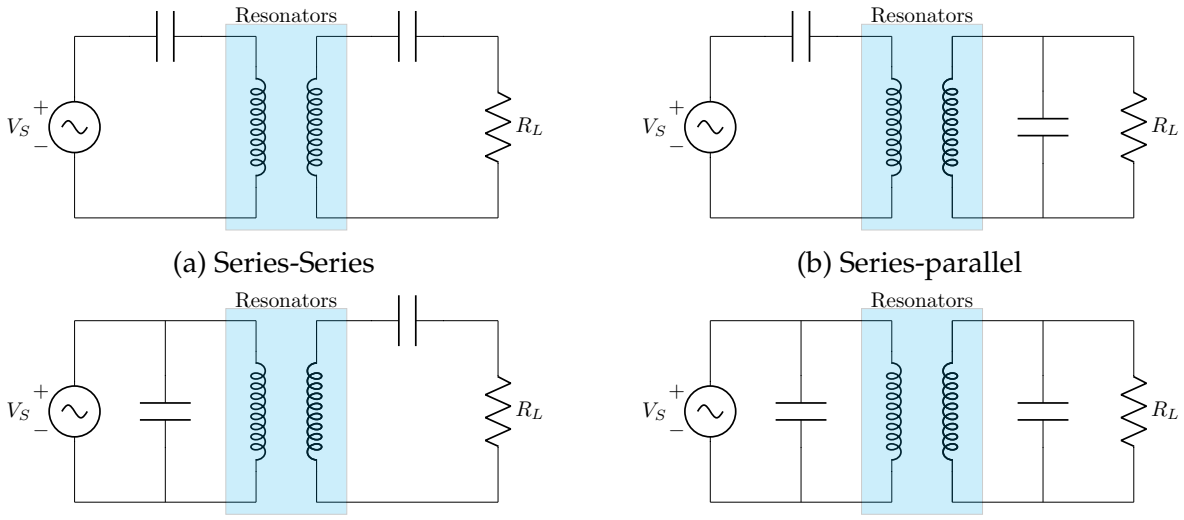

(a) Series-Series

(b) Series-parallel

(c) Parallel-series

(d) Parallel-parallel

Figure 2.3 – Basic reactance compensation topologies for RWPT systems.

2.2 Efficiency analysis of RWPT systems

One way to analyse RWPT systems is from its equivalent circuit analysis. Even though it is a simplified analysis that cannot provide precise information about the system behaviour, it is proved to be useful to model the power transfer efficiency, to determine the factors that potentially degrade it and how to mitigate them. In the present section, circuit models for two and four-coil RWPT systems are presented and analysed and, in the sequence, the main factors related to power transfer efficiency are discussed.

2.2.1 Two-coil RWPT efficiency

The circuit model for a two-coil RWPT system is presented in Figure 2.4a. In this circuit, each coil is described by a series RLC circuit in which the L is the coil inductance, R represents the ohmic and skin effect losses, and C accounts for the coil self-capacitance and lumped capacitances. The parameters related to the transmitter are indicated by the subscript 1 and 2 for the receiver. Consequently, the mutual inductance M_{12} describes the inductive coupling between them, and it is given by:

$$M_{12} = \kappa_{12}\sqrt{L_1 L_2}, \tag{2.1}$$

where κ_{12} is the coupling factor between them, such that $0 \leq \kappa_{12} \leq 1$.

In order to analyse this circuit model, an equivalent circuit is proposed in Figure 2.4b. Thus, the coupling between coils can be represented by a voltage-dependent source at the receiver and by reflecting the receiver coil impedance to the transmitter Z_{12}^{ref}, in

such a way that (ZHANG, 2018):

$$Z_{12}^{ref} = \frac{(\omega M_{12})^2}{R_2 + j\omega L_2 + \dfrac{1}{j\omega C_2} + R_L}. \tag{2.2}$$

Since for RWPT systems both transmitter and receiver coil must be tuned in the same resonant frequency, the inductive and capacitive reactances cancel each other and Z_{12}^{ref} can be simplified as:

$$Z_{12}^{ref} = \frac{(\omega M_{12})^2}{R_2 + R_L}. \tag{2.3}$$

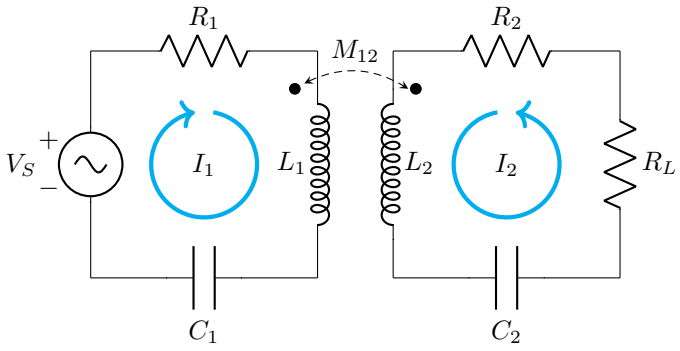

(a) Circuit model

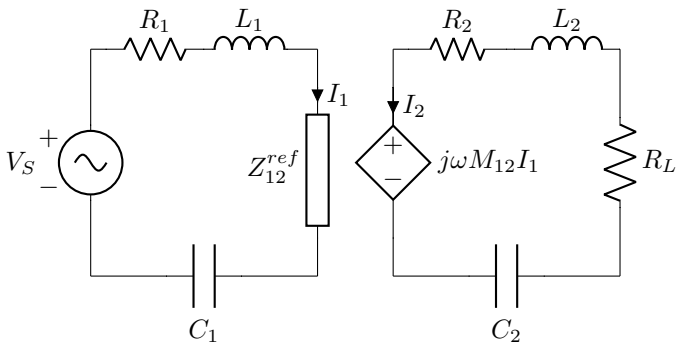

(b) Equivalent circuit

Figure 2.4 – Two-coil RWPT.

The RWPT efficiency η_{RWPT} can be defined as the ratio between the power delivered to the load R_L and the power supplied by the source, in this way:

$$\eta_{\text{RWPT}} = \frac{T_Q^2}{1 + \frac{R_L}{R_2} + T_Q^2} \cdot \frac{\frac{R_L}{R_2}}{1 + \frac{R_L}{R_2}}, \tag{2.4}$$

where T_Q is the transfer quality factor given by (ZHANG, 2018):

$$T_Q = \frac{\omega M_{12}}{\sqrt{R_1 R_2}}. \tag{2.5}$$

2.2.2 Four-coil RWPT efficiency

The circuit model and the efficiency calculation for a four-coil RWPT system can be carried out by applying the same approach used for the two-coil system. However, as in general the drive and sink coils have fewer turns than the transmitting and receiving resonators, their losses can be neglected as well as their self-capacitances. Besides, the mutual inductance between non-adjacent coils are much lesser than between adjacent coils, and they also can be disregarded. Thus, the resulting four-coil system circuit model is represented in Figure 2.5a and its equivalent circuit in 2.5b.

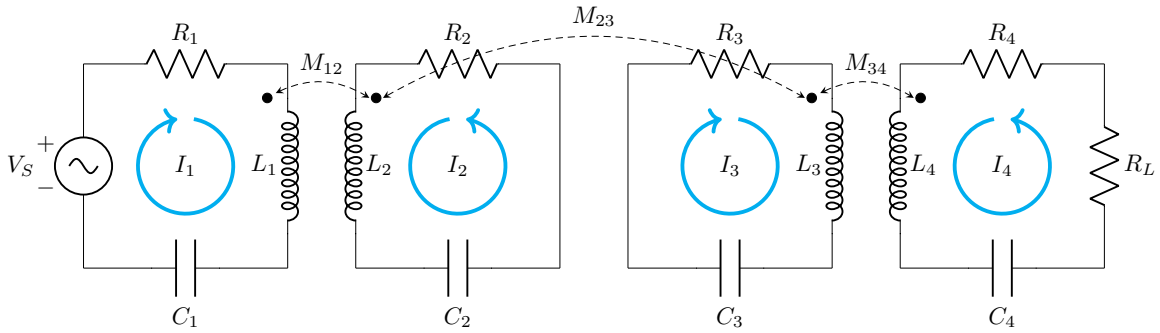

(a) Circuit model

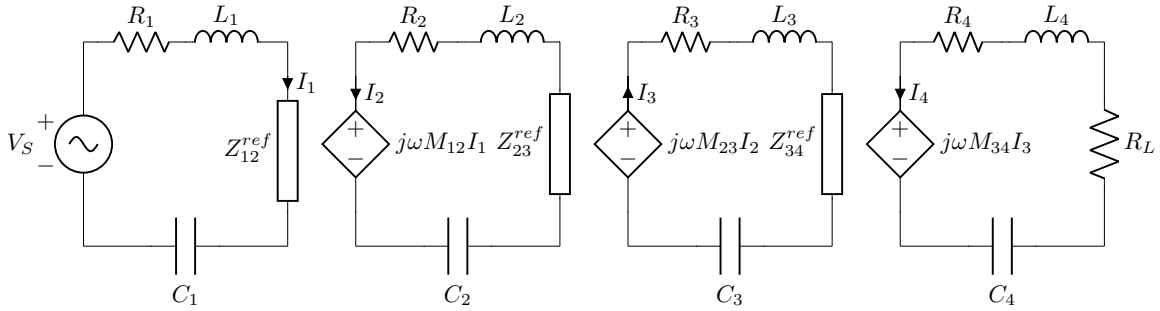

(b) Equivalent circuit

Figure 2.5 – Four-coil RWPT

If the whole system is tuned in the same resonant frequency, the reflected impedances can be defined as:

$$Z_{34}^{ref} = \frac{(\omega M_{34})^2}{R_L}, \tag{2.6a}$$

$$Z_{23}^{ref} = \frac{(\omega M_{23})^2}{R_3 + \frac{(\omega M_{34})^2}{R_L}}, \tag{2.6b}$$

$$Z_{12}^{ref} = \frac{(\omega M_{12})^2}{R_2 + \frac{(\omega M_{23})^2}{R_3 + \frac{(\omega M_{34})^2}{R_L}}}. \tag{2.6c}$$

By applying the same definition for efficiency used in the two-coil system, the power

transfer efficiency of a four-coil RWPT system is given by:

$$\eta_{\text{RWPT}} = \frac{T_Q^2}{1 + \frac{(\omega M_{34})^2}{R_3 R_L} + T_Q^2} \cdot \frac{\frac{(\omega M_{34})^2}{R_3 R_L}}{1 + \frac{(\omega M_{34})^2}{R_3 R_L}}, \tag{2.7}$$

where the transfer quality factor T_Q is:

$$T_Q = \frac{\omega M_{23}}{\sqrt{R_2 R_3}}. \tag{2.8}$$

2.2.3 Factors affecting RWPT efficiency

By observing the power transfer efficiency in equations 2.4 and 2.7, it can be noticed that both have a similar expression. So, the RWPT efficiency can be written more generally as:

$$\eta_{\text{RWPT}} = \frac{T_Q^2}{1 + L_M + T_Q^2} \cdot \frac{L_M}{1 + L_M}, \tag{2.9}$$

where the L_M is directly related with the impedance matching with the load at the receiver (ZHANG, 2018). The load matching factor for a two-coil RWPT system L_{M2} and for a four-coil system L_{M4} are given by:

$$L_{M2} = \frac{R_L}{R_2}, \tag{2.10a}$$

$$L_{M4} = \frac{(\omega M_{34})^2}{R_3 R_L}. \tag{2.10b}$$

Explicitly, the load matching factor L_M and the transfer quality factor T_Q are the two main factors that rule the RWPT efficiency. For instance, by inspection, an increase in L_M leads to a decrease in $\frac{T_Q^2}{1+L_M+T_Q^2}$ and an increase in $\frac{L_M}{1+L_M}$; thus, there is L_M^{opt} value in which the maximum efficiency is achieved. It can be found by calculating L_M that satisfies $\frac{\partial \eta_{RWPT}}{\partial L_M} = 0$, so:

$$L_M^{opt} = \sqrt{1 + T_Q^2}. \tag{2.11}$$

Consequently, there is an optimum load that leads to the maximum efficiency. Thereby, for a two-coil system, the optimum load is:

$$R_{L2}^{opt} = \sqrt{R_2 + \frac{R_2}{R_1}(\omega M_{12})^2}. \tag{2.12}$$

From this result, it can be verified that, as the receiver coil moves away from the transmitter and, consequently, the coupling between them decreases, the load that leads to the maximum efficiency also decreases, tending to $\sqrt{R_2}$. Alternatively, in a four-coil RWPT system the optimum load is given by:

$$R_{L4}^{opt} = \frac{(\omega M_{34})^2}{\sqrt{R_3 + \frac{R_3}{R_2}(\omega M_{23})^2}}. \tag{2.13}$$

In contrast to the behaviour verified for a two-coil system, when four coils are used, as the distance between receiver and transmitter increases, M_{23} decreases and the optimum load increases, reaching a maximum value of $\frac{(\omega M_{34})^2}{\sqrt{R_3}}$. However, in this case, there is a possibility to adjust this optimum impedance by varying M_{34}, that is, by changing the separation between the receiving resonator and the sink coil.

The condition for the load matching factor that leads to maximum efficiency indicated in equation 2.11 also establishes the dependence of maximum efficiency on the transfer quality factor. In this condition, the maximum efficiency can be written as:

$$\eta_{RWPT}^{max} = \left(\frac{T_Q}{1 + \sqrt{1 + T_Q^2}} \right)^2 . \tag{2.14}$$

The relationship between maximum RPWT efficiency and transfer quality factor expressed in the equation 2.14 is illustrated in Figure 2.6. As it can be seen, η_{RWPT}^{max} sharply rises for low T_Q values, whereas for higher T_Q it asymptotically approaches one (ZHANG, 2018).

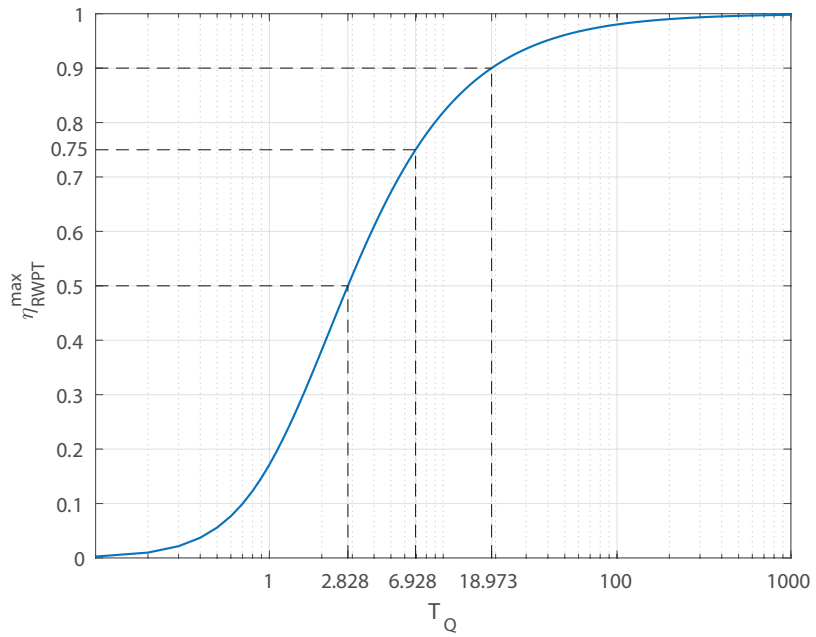

Figure 2.6 – Maximum RWPT efficiency (η_{RWPT}^{max}) as a function of the transfer quality factor (T_Q).

Another factor that significantly affects the RWPT efficiency but it is not explicitly presented in the previous analysis is the mismatching between source and system input impedance. When the internal impedance Z_S of a real power source, as shown in Figure 2.7 for a two-coil RWPT system is taken into account, the efficiency for this system can

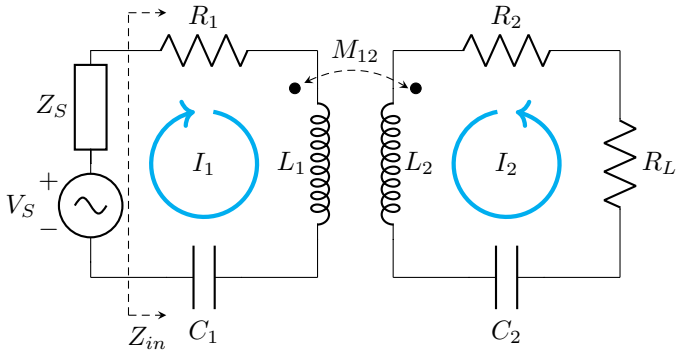

Figure 2.7 – Circuit model for the two-coil RWPT system with the source impedance (Z_S) and the input impedance (Z_{in}) viewed by the source.

be written as (ZHANG, 2018):

$$\eta_{\text{RWPT}} = \frac{T_Q^2}{(1+S_M)(1+L_M)+T_Q^2} \cdot \frac{L_M}{1+L_M}, \tag{2.15}$$

where $S_M = Z_S/R_1$. Note that when the source impedance is neglected, that is, $Z_S = 0$ the equation 2.15 takes the form of 2.9. However, this is not physically realizable, thus, the efficiency will always be reduced. Conversely, the output power P_{out} is given by:

$$P_{out} = \frac{V_S^2}{R_1} \frac{T_Q^2 L_M}{\left[(1+S_M)(1+L_M)+T_Q^2\right]^2} \tag{2.16}$$

In this case, the optimum value for R_{L2}^{opt} that leads to maximum output power is given by:

$$L_M^{opt} = \frac{1+S_M+T_Q^2}{1+S_M}. \tag{2.17}$$

By expanding the equation 2.17 in terms of the equation 2.5, it can be found that the maximum output power is achieved when:

$$Z_S = R_1 + \frac{(\omega M_{12})^2}{R_2 + R_L} \tag{2.18}$$

which is the maximum power transfer condition $Z_S = Z_{in}^*$. Moreover, applying the condition in equation 2.17 in the efficiency equation 2.15 and taking its limit when T_Q tends towards infinity, the result is that the efficiency equals to 50%, as expected for the maximum power transfer condition.

The same results can be obtained from the analysis of the four-coil RWPT system. In this case, the efficiency and output power are given by (ZHANG, 2018):

$$\eta_{\text{RWPT}} = \frac{S_M L_M}{(1+S_M)(1+L_M)+T_Q^2} \cdot \frac{T_Q^2}{1+L_M+T_Q^2}, \tag{2.19}$$

$$P_{out} = \frac{V_S^2}{Z_S} \frac{T_Q^2 L_M S_M}{\left[(1+S_M)(1+L_M)+T_Q^2\right]^2}, \tag{2.20}$$

in which $S_M = \frac{(\omega M_{12})^2}{Z_S R_2}$.

2.3 Frequency splitting

In the efficiency analysis accomplished up to this point, it was considered that the RWPT system operates in its resonant frequency so that the inductive and capacitive reactance cancel each other. However, if the operating frequency deviates from the resonant frequency, these reactances must be taken into account in the efficiency analysis. For instance, in a four-coil RWPT system, the frequency deviation f_d is characterized by:

$$f_d = \frac{\omega L_2 - \frac{1}{\omega C_2}}{R_2} = \frac{\omega L_3 - \frac{1}{\omega C_3}}{R_3}. \tag{2.21}$$

In this case, the RWPT efficiency can be written as (ZHANG, 2018):

$$\eta_{RWPT} = \frac{S_M L_M T_Q^2}{(f_d^2 + \xi)^2 + \left[(1+S_M)(1+L_M) + T_Q^2\right](1 + L_M + T_Q^2) - \xi^2} \tag{2.22}$$

where the parameter ξ is defined by:

$$\xi = \frac{(1+S_M) + (1+L_M)^2}{2} - T_Q^2. \tag{2.23}$$

The frequencies in which the RWPT efficiency is maximum can be found by taking $\frac{\partial \eta_{RWPT}}{\partial f_d} = 0$. Then, it can be shown that the efficiency peak happens in three conditions: for $f_d = 0$ and $f_d = \pm\sqrt{-\xi}$. In the resonant frequency, $f_d = 0$ and the RWPT efficiency is equal to equation 2.19. In order to analyse the physical meaning of the other conditions, it is convenient to define a critical transfer quality factor T_Q^c in which $\xi = 0$. Therefore:

$$T_Q^c = \sqrt{\frac{(1+S_M) + (1+L_M)^2}{2}}. \tag{2.24}$$

In this case, when $T_Q \leq T_Q^c$, $\xi \geq 0$, that is, for small T_Q values the condition, $\pm\sqrt{-\xi}$ is undefined, and the maximum efficiency is achieved at the resonant frequency f_r. On the other hand, if $T_Q > T_Q^c$, $\xi < 0$ and there are two efficiency peaks in $f_d = f_r - \sqrt{-\xi}$ and $f_d = f_r + \sqrt{-\xi}$, both of them less intense than those achieved at the previous cases.

This phenomenon in which the RWPT efficiency peaks simultaneously at frequencies below and above the resonant frequency is called **frequency splitting**. Due to this phenomenon, as the distance between transmitter and receiver coil is reduced they become overcoupled, and the maximum efficiency is split into two smaller peaks in frequencies around, but not in the resonant frequency, as it is shown in Figure 2.8.

When the same analysis is carried out for the two-coil RWPT system efficiency (ZHANG, 2018):

$$\eta_{RWPT} = \frac{T_Q^2}{(1+S_M)(1+L_M) + T_Q^2 + \left(\frac{1+S_M}{1+L_M}\right) f_d^2} \cdot \frac{L_M}{1+L_M} \tag{2.25}$$

it can be demonstrated that the maximum efficiency is achieved only at the resonant frequency, and the frequency splitting phenomenon does not happen for two-coil RWPT efficiency. Furthermore, it can be verified in equation 2.25 that the efficiency decreases as the frequency deviation increases, and no other peak can occur outside $f_d = 0$. However, when performing the same analysis for other parameters, it can be observed that the frequency splitting phenomenon affects the voltage gain, output current, and output power for both two-coil or multiple coil RWPT system (ZHANG; ZHAO, 2014; ZHANG; ZHAO; CHEN, 2014; HUANG et al., 2014).

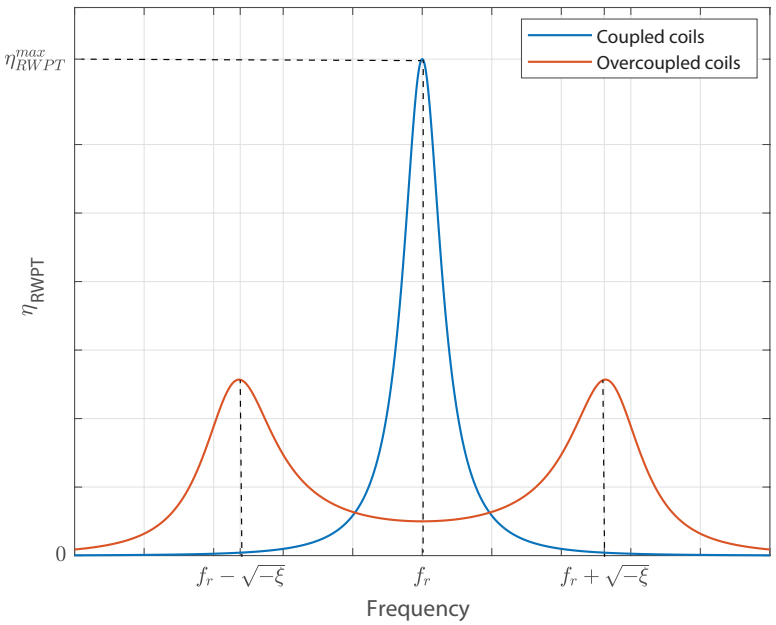

Figure 2.8 – RWPT efficiency for coupled and overcoupled coils evidencing the frequency splitting phenomenon.

Frequency splitting is intrinsically related to the impedance mismatching between RWPT system and source. For instance, in a two-coil system, the input impedance can be written as:

$$Z_{in} = R_1 \left[1 + \frac{T_Q^2 (1 + L_M)}{(1 + L_M)^2 + f_d^2} \right] + jR_1 \left[f_d - \frac{T_Q^2 f_d}{(1 + L_M)^2 + f_d^2} \right]. \tag{2.26}$$

In this equation, it is noticed that at the resonant frequency, and considering that the maximum power transfer condition is met, the frequency deviation is null, and the input impedance is purely real and equal to source impedance. As the distance between the transmitter and receiver coils decreases, the coupling between them is increased, increasing the transfer quality factor and the frequency deviation as well. Therefore, the input reactance increases faster than the input resistance, and the input impedance tends to be purely imaginary. Thus, since the resistance at the source coil is low, a large current is drained from the source, resulting in a high power loss at

the source impedance. Concomitantly, a large input reactance results in the power being mostly stored in the magnetic field rather than delivered to the load. Then, RWPT efficiency is significantly reduced (ZHANG; ZHAO; CHEN, 2013). However, by calculating the zeros of the imaginary part of Z_{in}, it can be found that the input impedance is purely resistive at the resonant frequency in which $f_d = 0$, as expected, but also at $f_d = \pm\sqrt{-\left[(L_M + 1)^2 - T_Q\right]}$ which are the two efficiency peaks below and above the resonant frequency that characterize the frequency splitting phenomenon.

Therefore, an option to attenuate the frequency splitting is by using an impedance matching network as an interface between the power source and the RWPT system. Then, as the distance between coils is changed, the network automatically matches Z_{in} to Z_S, increasing the RWPT efficiency (ANOWAR et al., 2017). Another alternative to mitigate the frequency splitting effects is by tracking the resonant frequency at close distances and automatically retuning the power source frequency (FENG; SIT, 2020). This can also be achieved by changing the orientation of the coils in order to smooth the mutual coupling increasing (LEE et al., 2013).

2.4 RWPT efficiency enhancement via effective permeability manipulation

Different techniques have been proposed to increase the efficiency of RWPT systems based on the affecting factors previously discussed. For instance, there are enhancement techniques related to the resonator structure with novel topologies (ZHANG; LIN; HUI, 2018), using magnetic materials (WANG et al., 2019), and increasing the number of resonators (XU et al., 2018). Furthermore, efficiency improvement can also be achieved with optimized reactance compensation circuits (LU et al., 2017), automatic impedance matching (JEONG; LIN; TENTZERIS, 2019) and efficiency tracking algorithms (YEO et al., 2017).

In addition to it, a manner to significantly improve the RWPT efficiency is by manipulating the effective magnetic permeability of the transmitting stage. According to this technique proposed in (AHN; KIANI; GHOVANLOO, 2014), an additional resonator is included in the vicinity of the transmitting resonator in such a way that they are linked by an intense magnetic flux. This flux induces a current in the additional resonator, creating a magnetic dipole moment. When the excitation frequency of the RWPT system ω is lower than the resonator frequency ω_M, the magnetic dipole moments of both structures are in phase. In this case, the real part of the effective magnetic permeability μ_{eff} of the overall system is greater than the unit. As ω increases, the real and the imaginary part of μ_{eff} also increase, until the phase difference between the magnetic dipole moments reaches 90°at ω_M. At these points, the real part of μ_{eff} is maximum, as

well as its imaginary part which is associated with the losses in the added resonator. By further increasing ω, the magnetic dipole moments become out of phase, thus sharply decreasing the real part of μ_{eff}. The described behaviours of the real μ'_{eff} and imaginary μ''_{eff} parts of the effective permeability as a function of the excitation frequency are illustrated in Figure 2.9.

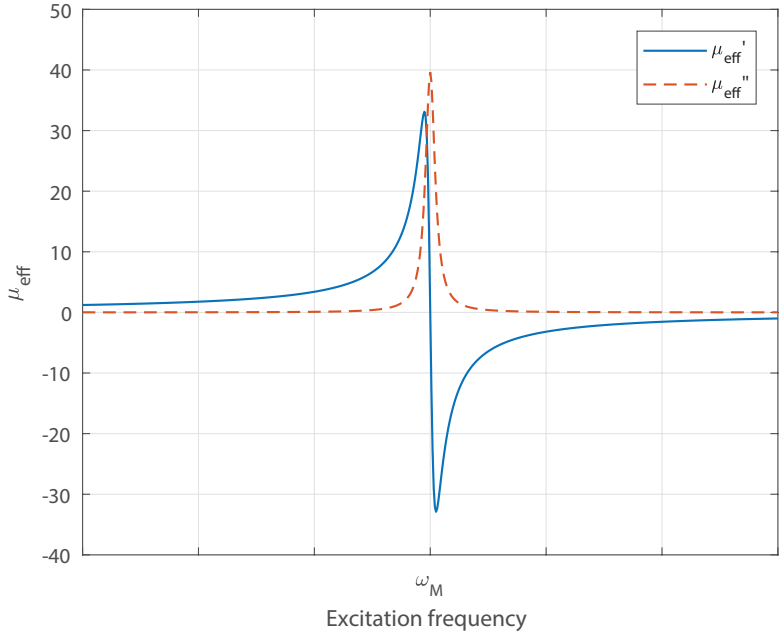

Figure 2.9 – Effective magnetic permeability behaviour of the RWPT system with the additional resonator as a function of the excitation frequency.

The way in which the added resonator manipulates the effective magnetic permeability can be modelled based on the electric circuit in Figure 2.9, in which the inductor L_1 is the transmitter coil inductance, the $R_M L_M C_M$ series stage represents the additional resonator, and M_{1M} is the mutual inductance between them. Therefore, the input impedance of this circuit is given by:

$$Z_{in} = j\omega L_1 + \frac{(\omega M_{1M})^2}{R_M + j\omega L_M - \frac{j}{\omega C_M}}. \tag{2.27}$$

As the magnetic permeability of an inductor is proportional to its inductance (AHN; KIANI; GHOVANLOO, 2014), it is convenient to rewrite 2.27 as a function of the transmitter reactive inductance:

$$Z_{in} = j\omega L_1 \left(1 + \frac{k_{1M}^2}{\frac{1}{Q_M} + \frac{\omega_M^2}{\omega^2} - 1}\right), \tag{2.28}$$

where k_{1M} is the coupling factor, $Q_M = \frac{\omega L_M}{R_M}$ is the resonator quality factor, and $\omega_M = \frac{1}{\sqrt{L_M C_M}}$ is its resonant frequency. In this way, the effective magnetic permeability is

given by:

$$\mu_{eff} = \underbrace{\left(\frac{\phi k_{1M}^2 Q_M^2}{\phi^2 Q_M^2 + 1}\right)}_{\mu'_{eff}} - j\underbrace{\left(\frac{k_{1M}^2 Q_M}{\phi^2 Q_M^2 + 1}\right)}_{\mu''_{eff}}, \tag{2.29}$$

where $\phi = \frac{\omega_M^2}{\omega^2} - 1$.

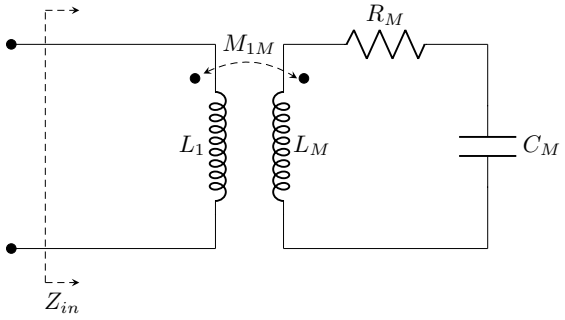

Figure 2.10 – Circuit model for the coupling between transmitter inductance and the added resonator.

By carrying out the derivation for RWPT efficiency proposed in (AHN; KIANI; GHOVANLOO, 2014), it is verified that in the optimum operation condition, the efficiency for an RWPT with the additional resonator can be approximated by:

$$\eta_{\text{RWPT}} = \frac{2T_Q^2}{1 + L_M + 2T_Q^2} \cdot \frac{L_M}{1 + L_M}. \tag{2.30}$$

When compared to the equation for the RWPT efficiency in 2.9, the enhancement with the inclusion of the additional resonator becomes evident. It is important to notice that this is a conservative approximation since, for the purpose of simplicity, it assumes that the quality factor of the added resonator is equal to the transmitter coil while, in practice, it is higher because the resonator is not physically connected to the RF power source. Besides, it is considered that the coupling factor between the resonator and the receiver coil is equal to the transmitter and receiver coils, when, in fact, it is slightly larger. Therefore, the efficiency improvement is even greater than estimated (AHN; KIANI; GHOVANLOO, 2014).

Hitherto, it was described only the operation principle of the RWPT efficiency enhancement by manipulating the effective magnetic permeability, and an approximation for this enhancement was presented. However, the physical realization of this principle and how to design this additional resonator still needs to be discussed. This discussion is left to the chapter 4,that is dedicated to the analysis and design of these structures.

2.5 Partial conclusions

In this chapter, the operating principle of RWPT system was discussed and the factors that influence its efficiency were analysed through the circuit model of two-coil and four-coil RWPT systems. The main factors that define the power transfer efficiency are the coupling between resonators and the impedance matching of the whole system with the source and load impedances. Thereby, as the coupling between coils increase, so does the efficiency. However, when the separation between resonators is such that the system is in the overcoupled region, the maximum efficiency is deviated from the resonant frequency and split into two other frequencies around it, decreasing the RWPT efficiency. Therefore, in order to design an efficient RWPT system, the operation conditions such as distance range, operation frequency, source and load impedances must be carefully optimised. In addition to it, it is discussed a manner to enhance the RWPT efficiency by manipulating the effective magnetic permeability of the overall system, which is accomplished by the insertion of an additional resonator close to the transmitting one. Thus, the interaction between the magnetic dipole moments of both resonators increases the coupling between transmitter and receiver, consequently increasing the RWPT system efficiency.

3 Electromagnetic Analysis of Thin Microstrip Structures

In this chapter, the electromagnetic problem concerning RWPT systems is described and formulated by applying the scattering and radiation integro-differential equation framework. Then, this tridimensional formulation is reduced to an unidimensional problem through the thin-wire approximation, and it is numerically formulated with the application of the Method of Moments. In this approach, the unknown current along the wire is represented by a finite weighted sum of known basis functions with weighting values obtained with a linear system solution. The computational aspects related to the implementation of the developed model is discussed and, then, the calculated results are compared with a commercial software also based on the Method of Moments.

Furthermore, the contribution of lumped impedances are accounted into the thin-wire integro-differential formulation, and some approximations are introduced to model a thin microstrip structure. Therefore, an equivalent radius is defined to model the rectangular microstrip cross-section, and the substrate electric permittivity is treated as an effective homogeneous medium. Finally, the thin wire microstrip model is experimentally validated with reflection coefficient measurements.

3.1 Problem description

The problem under consideration in this chapter is the electromagnetic analysis of RWPT structures and its numerical solution. By taking into account the operation frequency of these systems, their structures are in general much smaller than the wavelength and their topology is filamentary, which may be physically realized through conductive wires or printed microstrips. These characteristics motivate the application of thin-wire approximation, which considerably simplifies the mathematical modelling and reduces the computational cost of its implementation.

Therefore, in this case, the problem can be understood as a filamentary Perfect Electric Conductor (PEC) structure immersed in a homogeneous medium with an effective electric permittivity ε_{eff} and magnetic permeability μ_{eff} which are a function of the substrate properties, as shown in Figure 3.1. This structure is illuminated by an electromagnetic wave characterized by its incident electric and magnetic fields components.

For this analysis to be done, the scattering and radiation integral equations, as well as the thin-wire approximation, are applied to formulate the mathematical modelling for

this problem. Then, the numerical solution of these equations is implemented through the Method of Moments. In addition, some approximations are adopted to include the contribution of dielectric properties and lumped elements, which makes it possible to extend the thin-wire approach to thin microstrip structures.

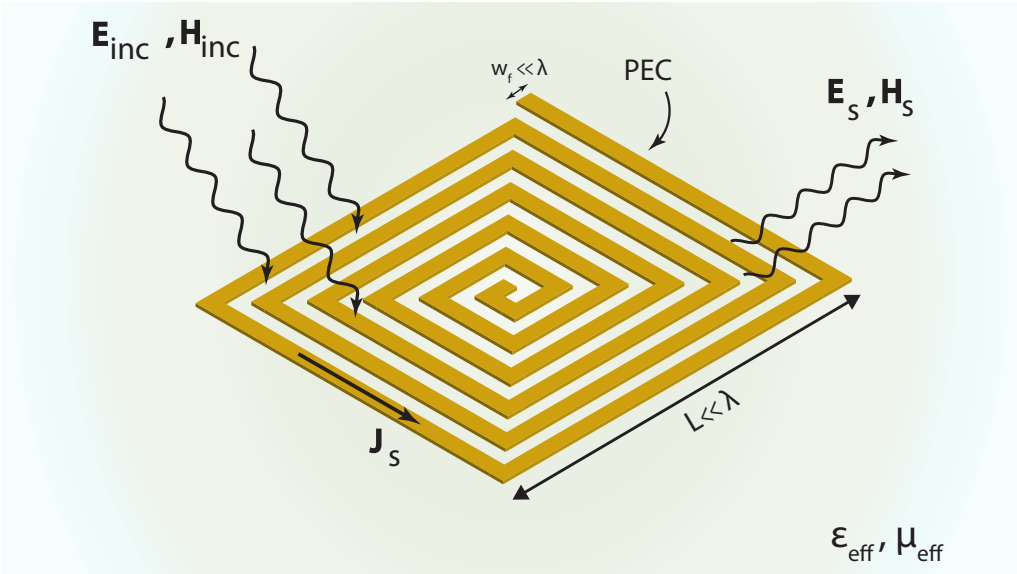

Figure 3.1 – Representation of the problem under analysis.

3.2 Scattering and radiation equations

When an electromagnetic wave, characterized by its electric $\mathbf{E}_{inc}$ and magnetic $\mathbf{H}_{inc}$ fields, reaches a PEC obstacle, these incident fields induce electric and magnetic currents (mathematically represented by the densities of electric $\mathbf{J}_s$ and magnetic $\mathbf{M}_s$ currents) on the surface of this body, which in turn radiates the scattered electric $\mathbf{E}_s$ and magnetic fields $\mathbf{H}_s$. The total electric $\mathbf{E}_T$ and magnetic $\mathbf{M}_T$ fields are, therefore, those resulting from the incident and scattered fields:

$$\mathbf{E}_T = \mathbf{E}_{inc} + \mathbf{E}_s, \tag{3.1}$$

$$\mathbf{H}_T = \mathbf{H}_{inc} + \mathbf{H}_s. \tag{3.2}$$

Thus, to find the total fields, it is first needed to calculate the fields generated by the superficial currents and then, to impose the proper boundary conditions.

In scattering and radiation problems, once the sources are known, the scattered or radiated field can be calculated through two different paths. In the first one, the electric $\mathbf{J}_s$ and magnetic $\mathbf{M}_s$ currents are directly integrated, whereas, in the second path, the magnetic $\mathbf{A}$ and electric $\mathbf{F}$ vector potentials can be found by integrating the same currents. Then, the electric $\mathbf{E}_s$ and magnetic $\mathbf{H}_s$ fields are calculated by differentiating

the respective potentials. Even though the second path requires more calculation steps, the integrating function, in this case, is simpler. In both cases, the integrals are limited by the source boundaries; therefore, the radiated field, as well as the potentials from them, are functions of the observation points (BALANIS, 2016).

As shown in Figure 3.1, the problem under analysis consists of finding the electric $\mathbf{E}_s$ and magnetic $\mathbf{H}_s$ fields scattered on a filamentary PEC obstacle which is illuminated by a wave with incident fields $\mathbf{E}_{inc}$ and $\mathbf{H}_{inc}$. A general strategy to solve this kind of problem is to divide it into an inner and an outer problem. However, as in the presented case, the obstacle is PEC there are not inner fields and, therefore, only the outer problem is taken into account. Furthermore, the magnetic current density is null. So, the integral equations for the total electric $\mathbf{E}(\mathbf{r}, \mathbf{r}')$ and magnetic $\mathbf{H}(\mathbf{r}, \mathbf{r}')$ fields can be written as (SOARES, 2017):

$$\mathbf{E_0}(\mathbf{r}, \mathbf{r}') = \eta\mathcal{L}(\mathbf{J_s}) + \mathbf{E_{inc}}(\mathbf{r}), \tag{3.3}$$

$$\mathbf{H_0}(\mathbf{r}, \mathbf{r}') = -\mathcal{K}(\mathbf{J_s}) + \mathbf{H_{inc}}(\mathbf{r}), \tag{3.4}$$

where η is the intrinsic impedance of the medium, and $\mathbf{r}$ and $\mathbf{r}'$ are the vector position for the observer and source, respectively. The integro-differential operators $\mathcal{L}(\mathbf{J_s})$ and $\mathcal{K}(\mathbf{J_s})$ are defined as (RESENDE, 2007):

$$\mathcal{L}(\mathbf{J_s}) = -\frac{j}{4\pi k}\iint_S k^2\mathbf{J_s}(\mathbf{r}')\Psi(\mathbf{r}, \mathbf{r}') - [\boldsymbol{\nabla}\cdot\mathbf{J_s}(\mathbf{r}')]\boldsymbol{\nabla}\Psi(\mathbf{r}, \mathbf{r}')\,\mathrm{d}s', \tag{3.5}$$

$$\mathcal{K}(\mathbf{J_s}) = \frac{1}{4\pi}\iint_S \mathbf{J_s}(\mathbf{r}')\times\boldsymbol{\nabla}\Psi(\mathbf{r}, \mathbf{r}')\,\mathrm{d}s', \tag{3.6}$$

where k is the propagation constant and $\Psi(\mathbf{r}, \mathbf{r}')$ is the Green's function for the free space given by:

$$\Psi(\mathbf{r}, \mathbf{r}') = \frac{e^{-jk|\mathbf{r}-\mathbf{r}'|}}{|\mathbf{r}-\mathbf{r}'|}. \tag{3.7}$$

The tangential components of the electric and magnetic fields on a PEC obstacle are subjected to the following boundary conditions:

$$\hat{n}\times\mathbf{E_0}(\mathbf{r}, \mathbf{r}') = 0, \tag{3.8}$$

$$\hat{n}\times\mathbf{H_0}(\mathbf{r}, \mathbf{r}') = \mathbf{J}_s(\mathbf{r}). \tag{3.9}$$

By imposing these boundary conditions on the equations 3.8 and 3.9, the Electric Field Integro-differential Equation (EFIE) and the Magnetic Field Integro-differential Equation (MFIE) are defined as:

$$\hat{\mathbf{n}}\times\mathbf{E_{inc}}(\mathbf{r}) = -\hat{\mathbf{n}}\times[\eta\mathcal{L}(\mathbf{J_s})]\,, \tag{3.10}$$

$$\hat{\mathbf{n}} \times \mathbf{H_{inc}} = \mathbf{J_s}(\mathbf{r}') + \hat{\mathbf{n}} \times \mathcal{K}(\mathbf{J_s}). \tag{3.11}$$

However, the MFIE is valid only for closed surfaces (BONDESON; RYLANDER; INGELSTROM, 2012) that is not the case for the problem under analysis. Therefore, only the EFIE is considered henceforward.

3.3 Thin-wire approximation

As in the analysed problem the radius a of the wire cross-section is much lesser than the wavelength ($a \ll \lambda$) and the wire length ($a \ll L$), the surface current density $\mathbf{J_s}(\mathbf{r})$ can be approximated by a filamentary current indicated in Figure 3.2 that flows on the direction $\hat{t}$ tangential to the wire, according to the equation:

$$\mathbf{J}_s(\mathbf{r}') = \frac{I(t')}{2\pi a}\hat{t}. \tag{3.12}$$

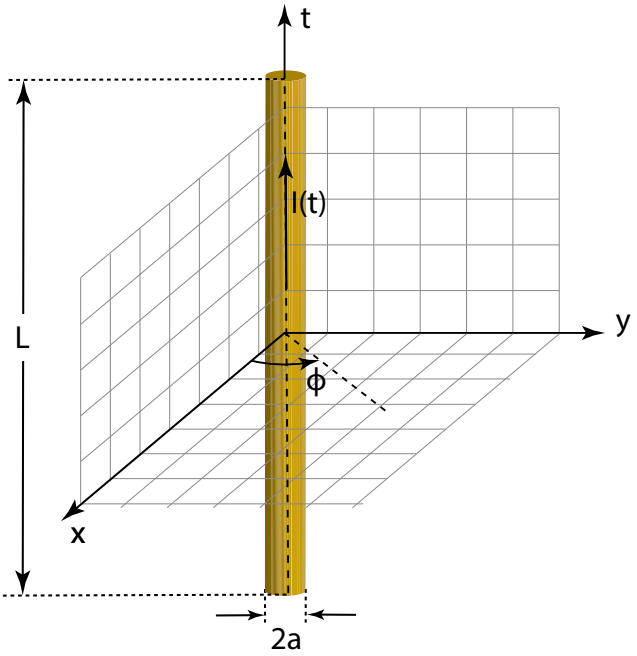

Figure 3.2 – Coordinate system definition for the thin-wire approximation.

In this case, it is assumed that the current does not vary in the $\hat{\phi}$ direction and that it goes to zero at the wire extremities (GIBSON, 2015). Therefore, by applying this approximation into the equation 3.5, it is possible to define the thin-wire approximation for the integro-differential operator $\mathcal{L}(\mathbf{J_s})$ as:

$$\mathcal{L}\left[\mathbf{I}(t')\right] = -\frac{j}{4\pi k}\int_{t'} k^2\mathbf{I}(t')\Psi(\mathbf{r},\mathbf{r}') - [\boldsymbol{\nabla}\cdot\mathbf{I}(t'))]\boldsymbol{\nabla}\Psi(\mathbf{r},\mathbf{r}')\,\mathrm{d}t', \tag{3.13}$$

where $\mathbf{I}(t') = I(t')\hat{t}$. With this approximation, the EFIE can be expanded as follow:

$$\hat{\mathbf{n}} \times \mathbf{E_{inc}}(\mathbf{r}) = \hat{\mathbf{n}} \times \left[\frac{j}{4\pi\omega\varepsilon}\int_{t'} k^2\mathbf{I}(t')\Psi(\mathbf{r},\mathbf{r}') - [\boldsymbol{\nabla}\cdot\mathbf{I}(t'))]\boldsymbol{\nabla}\Psi(\mathbf{r},\mathbf{r}')\,\mathrm{d}t'\right]. \tag{3.14}$$

3.4 Formulation of the Method of Moments

In general, an integro-differential equation can be understood as a linear operator $\mathfrak{L}$ that acts on the function $\boldsymbol{f}$ to be determined, resulting in the known function $\boldsymbol{g}$:

$$\mathfrak{L}(\boldsymbol{f}) = \boldsymbol{g}. \tag{3.15}$$

The unknown function $\boldsymbol{f}$ can be expanded into a series of known functions f_n multiplied by the unknown coefficients α_n:

$$\boldsymbol{f} = \sum_{n=1}^{N} \alpha_n \boldsymbol{f}_n, \tag{3.16}$$

where N is the total number of known functions. The functions $\boldsymbol{f}_n$ are called **basis functions**. In this way, as N is finite and the operator $\mathfrak{L}$ is linear, the equation 3.15 can be written as:

$$\sum_{n=1}^{N} \alpha_n \mathfrak{L}(\boldsymbol{f}_n) \approx \boldsymbol{g}. \tag{3.17}$$

From 3.15, a residue R can be defined as:

$$R = \boldsymbol{g} - \sum_{n=1}^{N} \alpha_n \mathfrak{L}(\boldsymbol{f}_n). \tag{3.18}$$

To reconstruct the function $\boldsymbol{f}$, the coefficients α_n in the equation 3.17 must be found. So, this can be understood as an equation with N unknowns. Therefore, it is necessary to develop a strategy to calculate α_n.

Consider $\mathcal{E}\{\boldsymbol{f}_n\}$ as the subspace of the basis functions and $\mathcal{E}\{\boldsymbol{w}_m\}$ the subspace of the orthonormal **weighting functions (or testing functions)** $\boldsymbol{w}_m$. An inner product or **moment** between a weighting function and a basis function can be defined as:

$$\langle \boldsymbol{w}_m, \boldsymbol{f}_n \rangle = \int_S \boldsymbol{w}_m(\mathbf{r}) \cdot \int_{S'} \boldsymbol{f}_n(\mathbf{r}') \ \mathrm{d}\mathbf{r}'\mathrm{d}\mathbf{r}, \tag{3.19}$$

with the integrals being defined in a line, surface or volume, depending on the discretization of the problem domain. Consider $\mathcal{E}\{\mathfrak{L}(\boldsymbol{f}_n)\}$ as the subspace formed by the application of the operator $\mathfrak{L}$ in the basis functions, by imposing the moment of each weighting functions with the residue to be equal to zero (GIBSON, 2015):

$$\sum_{n=1}^{N} \alpha_n \langle \boldsymbol{w}_m, \mathfrak{L}(\boldsymbol{f}_n) \rangle = \langle \boldsymbol{w}_m, \boldsymbol{g} \rangle \quad , m = 1, 2, ..., N. \tag{3.20}$$

The equation 3.20 can also be found by another approach. By defining the projection of the function $\mathfrak{L}(\boldsymbol{f}_n)$ in the subspace of the weighting functions $\mathcal{E}\{\boldsymbol{w}_m\}$ as:

$$\mathbf{pr}_w [\mathfrak{L}(\boldsymbol{f}_n)] = \sum_{m=1}^{N} \langle \boldsymbol{w}_m, \mathfrak{L}(\boldsymbol{f}_n) \rangle \cdot \boldsymbol{w}_m. \tag{3.21}$$

The MoM equalizes the projection of the approximation $\mathfrak{L}(\boldsymbol{f}_n)$ with the exact value $\boldsymbol{g}$ (HARRINGTON, 1993), so:

$$\sum_{n=1}^{N} \alpha_n \left\langle \boldsymbol{w}_m, \mathfrak{L}(\boldsymbol{f}_n) \right\rangle = \langle \boldsymbol{w}_m, \boldsymbol{g} \rangle \quad , m = 1, 2, ..., N \tag{3.22}$$

The equation 3.20 is, in fact, a linear system with N equations and N unknowns α_n. Consequently, it can be written in matrix notation:

$$\mathbb{L}_{(N\times N)} \cdot \mathbb{A}_{(N)} = \mathbb{G}_{(N)}, \tag{3.23}$$

where:

$$\mathbb{L} = \begin{bmatrix} \langle \boldsymbol{w}_1, \mathfrak{L}(\boldsymbol{f}_1) \rangle & \langle \boldsymbol{w}_1, \mathfrak{L}(\boldsymbol{f}_2) \rangle & \cdots & \langle \boldsymbol{w}_1, \mathfrak{L}(\boldsymbol{f}_N) \rangle \\ \langle \boldsymbol{w}_2, \mathfrak{L}(\boldsymbol{f}_1) \rangle & \langle \boldsymbol{w}_2, \mathfrak{L}(\boldsymbol{f}_2) \rangle & \cdots & \langle \boldsymbol{w}_2, \mathfrak{L}(\boldsymbol{f}_N) \rangle \\ \vdots & \vdots & \ddots & \vdots \\ \langle \boldsymbol{w}_N, \mathfrak{L}(\boldsymbol{f}_1) \rangle & \langle \boldsymbol{w}_N, \mathfrak{L}(\boldsymbol{f}_2) \rangle & \cdots & \langle \boldsymbol{w}_N, \mathfrak{L}(\boldsymbol{f}_N) \rangle \end{bmatrix}, \tag{3.24a}$$

$$\mathbb{A} = \begin{bmatrix} \alpha_1 \\ \alpha_2 \\ \vdots \\ \alpha_N \end{bmatrix}, \quad \mathbb{G} = \begin{bmatrix} \langle \boldsymbol{w}_1, \boldsymbol{g} \rangle \\ \langle \boldsymbol{w}_2, \boldsymbol{g} \rangle \\ \vdots \\ \langle \boldsymbol{w}_N, \boldsymbol{g} \rangle \end{bmatrix}. \tag{3.24b}$$

If the matrix $\mathbb{L}$ is invertible, so the coefficient matrix $\mathbb{A}$ is given by:

$$\mathbb{A} = \mathbb{L}^{-1}\mathbb{G}. \tag{3.25}$$

By defining $\mathbb{F}$ as the matrix formed by all the basis functions:

$$\mathbb{F} = \begin{bmatrix} \boldsymbol{f}_1 & \boldsymbol{f}_2 & \cdots & \boldsymbol{f}_N \end{bmatrix}, \tag{3.26}$$

from the equation 3.16, the unknown function $\boldsymbol{f}$ can be found as (HARRINGTON, 1993):

$$\boldsymbol{f} = \mathbb{F}\mathbb{L}^{-1}\mathbb{G}. \tag{3.27}$$

In this work, the Galerkin Method is applied to choose the basis and weighting functions. Specifically for MoM, this method is applied by using the same kind of basis and weighting functions, that is, $\boldsymbol{w}_m = \boldsymbol{f}_n$. This choice makes the computational implementation faster and more accurate, in addition to ensuring the energy conservation of the solution (RESENDE, 2007).

3.5 Application of the Method of Moments in the EFIE

In order to apply the MoM to the EFIE in the equation 3.14, the current $\mathbf{I}(t')$, which is the unknown function, must be expanded into a finite sum of known basis functions

$\mathbf{u}_j(t') = u_j(t')\hat{t}'$:

$$\mathbf{I}(t') = \sum_{j=1}^{N} I_j \mathbf{u}_j(t'), \tag{3.28}$$

where I_j are the unknown coefficients to be determined and N is the number of basis functions. By replacing 3.28 into the equation 3.14:

$$\hat{\mathbf{n}} \times \mathbf{E_{inc}}(\mathbf{r}) = \hat{\mathbf{n}} \times \left\{ \sum_{j=1}^{N} \left[\frac{j}{4\pi\omega\varepsilon} \int_{t'} k^2 \mathbf{u}(t')\Psi(\mathbf{r},\mathbf{r}') - [\boldsymbol{\nabla}\cdot\mathbf{u}_j(t'))]\boldsymbol{\nabla}\Psi(\mathbf{r},\mathbf{r}')\, \mathrm{d}t' \right] I_j \right\}. \tag{3.29}$$

Once the basis functions are known, the unknown coefficients I_j can be determined by taking the inner product with the weighting function $\mathbf{w}_i(t) = w_i(t)\hat{t}$ on both sides of the equation 3.29 and by integrating it along the observer:

$$\begin{aligned} \sum_{i=1}^{N} \int_t \mathbf{w}_i(t) \cdot [\hat{\mathbf{n}} \times \mathbf{E_{inc}}(\mathbf{r})]\, \mathrm{d}t = \frac{j}{4\pi\omega\varepsilon} \left\{ \sum_{i,j=1}^{N} \int_t \int_{t'} \mathbf{w}_i(t) \cdot \hat{\mathbf{n}} \times \times \left[k^2 \mathbf{u}(t')\Psi(\mathbf{r},\mathbf{r}') \right.\right. \\ \left.\left. - [\boldsymbol{\nabla}\cdot\mathbf{u}(t'))]\boldsymbol{\nabla}\Psi(\mathbf{r},\mathbf{r}')\, \mathrm{d}t'\mathrm{d}t \right] \right\} I_j. \end{aligned} \tag{3.30}$$

For the purpose of notation simplicity, the use of apostrophe (′) indicates quantities and operations related to the sources, while the others are related to the observer. The equation 3.30 can be written in matrix form:

$$\mathbb{V}_{(N\times 1)} = \mathbb{Z}_{(N\times N)} \cdot \mathbb{I}_{(N\times 1)}, \tag{3.31}$$

where the elements of the excitation matrix $\mathbb{V}$ are given by:

$$\mathbb{V}_i = \int_t \mathbf{w}_i(t) \cdot [\hat{\mathbf{n}} \times \mathbf{E_{inc}}(\mathbf{r})]\, \mathrm{d}t \tag{3.32}$$

After some algebraic and vector manipulations (RESENDE, 2007), the equation for the elements of the impedance matrix $\mathbb{Z}$ can be rewritten as:

$$\mathbb{Z}_{i,j} = \frac{j}{4\pi\omega\varepsilon} \int_t \int_{t'} k^2 w_i(t) u_j(t') \left(\hat{t}\cdot\hat{t}'\right) \Psi(\mathbf{r},\mathbf{r}') - \frac{\mathrm{d}w_i(t)}{\mathrm{d}t} \frac{\mathrm{d}u_j(t')}{\mathrm{d}t'} \Psi(\mathbf{r},\mathbf{r}')\, \mathrm{d}t'\mathrm{d}t. \tag{3.33}$$

Finally, the elements of the current matrix $\mathbb{I}$, that is, the unknown coefficients, can be found by solving the linear system in equation 3.31.

3.6 Numerical implementation

In order to solve the problem under analysis through the mathematical model developed in the previous sections, a treatment of the problem geometry and the integrals that

constitute this model must be held. Therefore, the next subsections present the geometry parametrization and discretization, the basis and weighting functions choice and the treatment of the equations for the impedance and excitation matrices elements. Overall, a trade-off between accuracy and computational cost is aimed. In this way, it is possible to develop a numerical method that is capable of dealing with costly problems and, at the same time, accurately describe the physical results obtained through experiments.

3.6.1 Geometry parametrization and discretization

A filamentary structure with arbitrary geometry that starts at a point A and ends at a point B in the tridimensional space $\mathbb{R}^3$ can be modelled as a parametric function $\mathbf{f}(t) = [A, B] \mapsto \mathbb{R}^3$ such as:

$$\mathbf{f}(t) = f_x(t)\hat{x} + f_y(t)\hat{y} + f_z(t)\hat{z}, \tag{3.34}$$

where $f_x(t)$, $f_y(t)$, and $f_z(t)$ are the parametric equations that define the curve $\mathbf{f}(t)$ (PRESSLEY, 2012).

Thus, a unit vector tangent to the curve $\mathbf{f}(t)$ at point s is given by:

$$\hat{t}(s) = \frac{\dfrac{\mathrm{d}\mathbf{f}(s)}{\mathrm{d}t}}{\left|\dfrac{\mathrm{d}\mathbf{f}(s)}{\mathrm{d}t}\right|}. \tag{3.35}$$

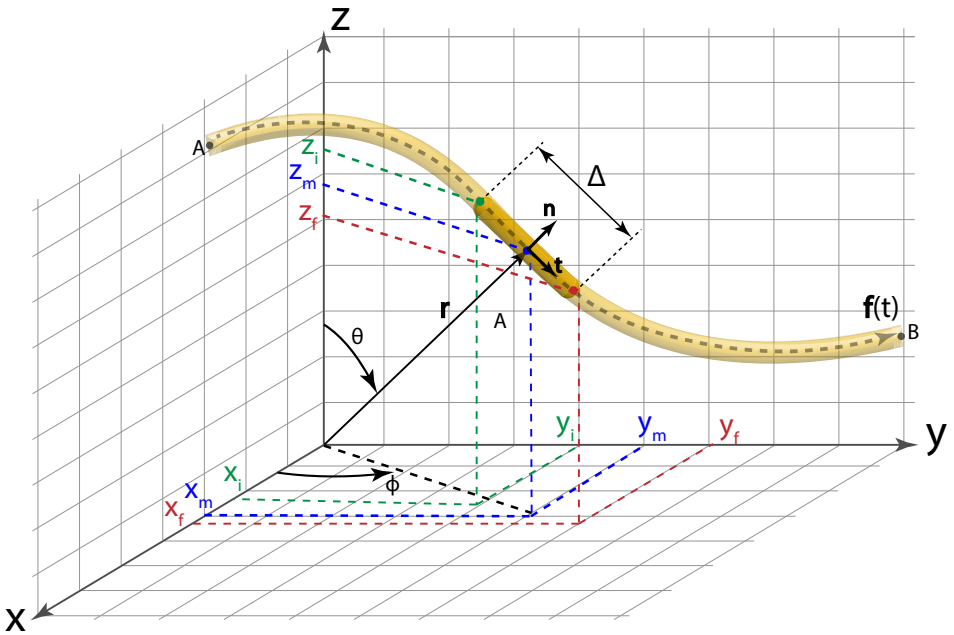

Figure 3.3 – Linear discretization of a parametric curve in the tridimensional space.

As shown in Figure 3.3, a manner to discretize a parametric curve is by dividing it into linear segments that start at the points (x_i, y_i, z_i) and end at (x_f, y_f, z_f), with a length Δ

such as:

$$\Delta = \sqrt{(\Delta x)^2 + (\Delta y)^2 + (\Delta z)^2} = \sqrt{(x_f - x_i)^2 + (y_f - y_i)^2 + (z_f - z_i)^2}. \tag{3.36}$$

Thus, by applying this discretization in the tangent vector definition in equation 3.35:

$$\hat{t} = \frac{\Delta x}{\Delta}\hat{x} + \frac{\Delta y}{\Delta}\hat{y} + \frac{\Delta z}{\Delta}\hat{z}. \tag{3.37}$$

In order to fully describe the discretized geometry, it is also convenient to define the angles θ and ϕ associated with each segment (MOREIRA, 2012):

$$\cos\phi = \frac{\Delta x}{\Delta xy}, \tag{3.38a}$$

$$\sin\phi = \frac{\Delta x}{\Delta xy}, \tag{3.38b}$$

$$\cos\theta = \frac{\Delta z}{\Delta xy}, \tag{3.38c}$$

where $\Delta xy = \sqrt{(\Delta x)^2 + (\Delta y)^2}$.

3.6.2 Choice of basis and weighting functions

Once the geometry is discretized, the next step to the numerical and computational implementation of the MoM is to choose the kind of known function to be used as basis and weighting functions.

There are several types of function that could be applied. The unitary pulse function simplifies the integrals and, thus, decreases the computational cost of calculating the elements of the impedance matrix. However, it leads to a rough approximation that can hide many aspects of the unknown function (GIBSON, 2015). In the case under analysis, choosing this type of function would lead to information losses related to the derivative of the basis and weighting functions since, for this type of basis function, the derivative is null.

In this work, the linear-piecewise function represented in Figure 3.4, also known as triangle function $T_n(t)$, is applied. It is composed of two functions, one defined by the linear variation from 0 to 1 in a segment and the other one from 1 to 0 in the adjacent segment. Therefore, each function is defined by two straight line segments, an increasing and a decreasing one, in such a way that it can be mathematically described by:

$$T_n(t) = \begin{cases} \dfrac{t - t_{n-1}}{t_n - t_{n-1}} & , t_{n-1} \leq t \leq t_n \\ \dfrac{t_{n+1} - t}{t_{n+1} - t_n} & , t_{n-1} \leq t \leq t_n \\ 0 & , \text{otherwise} \end{cases}. \tag{3.39}$$

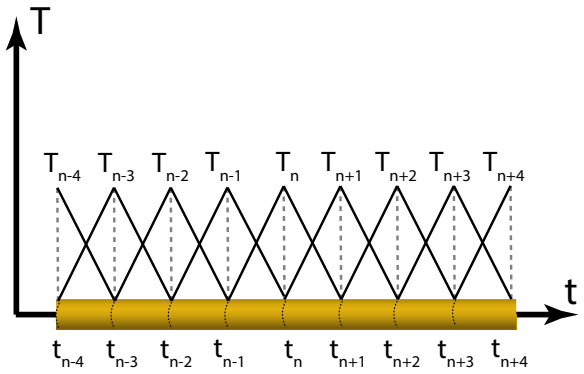

Figure 3.4 – Linear-piecewise (triangle) function.

Unlike the unitary pulse, this kind of function allows all terms of the impedance matrix integral to be considered. Furthermore, the evaluation of this integral is not unduly complicated, since the derivative of this type of function is simple. It is also considered a nodal function since the current at a node is associated with the vertex height of the triangle at this point (GUREL; SERTEL; ŞENDUR, 1999).

By applying the same approach used in equation 3.39, piecewise sinusoidal and cosinusoidal functions can be defined. However, the computational cost of evaluating the MoM integrals with these functions is significantly higher (GIBSON, 2015), and it is not worthy once the triangle function is able to suitably describe the behaviour of the current that flows in the filamentary structure.

In order to reduce the computational cost involved in the numerical evaluation of the integrals, it is convenient to define a variable transformation in such a way that a segment that goes from a point t_i to t_f, in the new variable α, goes from $\alpha_i = -1$ to $\alpha_f = +1$. This transformation can be defined as (MOREIRA, 2012):

$$t(\alpha) = t_m + \alpha\frac{\Delta}{2}\sin\theta\cos\phi, \tag{3.40}$$

where t_m is the segment midpoint. Therefore, the Cartesian coordinates of any point can be written based on this transformation:

$$x(\alpha) = x_m + \alpha\frac{\Delta}{2}\sin\theta\cos\phi, \tag{3.41a}$$

$$y(\alpha) = y_m + \alpha\frac{\Delta}{2}\sin\theta\cos\phi, \tag{3.41b}$$

$$z(\alpha) = z_m + \alpha\frac{\Delta}{2}\cos\phi. \tag{3.41c}$$

This transformation can be applied to both observer and source coordinates. The triangle function can also be redefined in the variable α as:

$$T_n(\alpha) = \frac{1-(-1)^{sgn}\alpha}{2}, \tag{3.42}$$

where sgn defines the piece of the function, that is, $sgn = 1$ indicates the half-triangle from the right (increasing function) and $sgn = 2$ indicates the half-triangle from the left (decreasing function). Thereby, the derivative of the triangle function is given by:

$$\frac{\mathrm{d}T_n}{\mathrm{d}t} = -\frac{(-1)^{sgn}}{\Delta}. \tag{3.43}$$

3.6.3 Numerical evaluation of the excitation and impedance integrals

Considering the triangle function defined in the variable α. Applying the substitution method, the equation 3.32 for the excitation matrix elements can be written as:

$$\mathbb{V}_i = \frac{2}{\Delta}\sum_{sgn=1}^{2}\int_{-1}^{1}\left[\frac{1-(-1)^{sgn}\alpha}{2}\right]E_{inc}^{t}(\mathbf{r})\,\mathrm{d}\alpha \tag{3.44}$$

where $E_{inc}^{t}(\mathbf{r})$ is the tangential component of the incident electric field.

Similarly, the equation 3.33, that provides the elements of the impedance matrix, is now given by:

$$\mathbb{Z}_{i,j} = \frac{j}{4\pi\omega\varepsilon}\frac{1}{\Delta\Delta'}\sum_{\substack{sgn=1\\ sgn'=1}}^{2}\left\{\left[\frac{k^2}{4}\left(\Delta x\Delta x'+\Delta y\Delta y'+\Delta z\Delta z'\right)\left(G_1+G_2+G_3+G_4\right)\right]-G_5\right\} \tag{3.45}$$

where the auxiliary integrals $G_1 - G_5$ are defined as follow:

$$G_1 = \int_{-1}^{1}\int_{-1}^{1}\Psi(\mathbf{r},\mathbf{r}')\,\mathrm{d}\alpha'\mathrm{d}\alpha \tag{3.46a}$$

$$G_2 = \int_{-1}^{1}\int_{-1}^{1}-(-1)^{sgn}\,\alpha\,\Psi(\mathbf{r},\mathbf{r}')\,\mathrm{d}\alpha'\mathrm{d}\alpha \tag{3.46b}$$

$$G_3 = \int_{-1}^{1}\int_{-1}^{1}-(-1)^{sgn'}\,\alpha'\,\Psi(\mathbf{r},\mathbf{r}')\,\mathrm{d}\alpha'\mathrm{d}\alpha \tag{3.46c}$$

$$G_4 = \int_{-1}^{1}\int_{-1}^{1}(-1)^{sgn}(-1)^{sgn'}\,\alpha\alpha'\,\Psi(\mathbf{r},\mathbf{r}')\,\mathrm{d}\alpha'\mathrm{d}\alpha \tag{3.46d}$$

$$G_5 = \int_{-1}^{1}\int_{-1}^{1}(-1)^{sgn}(-1)^{sgn'}\,\Psi(\mathbf{r},\mathbf{r}')\,\mathrm{d}\alpha'\mathrm{d}\alpha. \tag{3.46e}$$

The numerical evaluation of the integrals is performed through the Gaussian quadrature method. In this method, the integral of a given function is approximated by a sum of N Gaussian points multiplied by their respective weights. The possibility to choose the Gaussian points and weights gives to this method two degrees of freedom, which allows the use of higher quadrature formulas than other lesser order methods, such as the Newton-Cotes, with the same number of iterations (PRESS et al., 2007).

It is important to notice that, during the evaluation of the impedance matrix integrals, when the position of the observer $\mathbf{r}$ and the source $\mathbf{r}'$ coincide, there is a singularity in the Green's function presented in equation 3.7. Even though there are more accurate singularity treatment methods, they generally lead to a significant increase in the computational complexity once they are iterative methods (MIKKI; ALZAHED; ANTAR, 2019). Therefore, for purposes of lower computational costs, the singularity was circumvented by using a different number of Gauss points for the evaluation of the integral related to the observer and the source, so that, numerically, the evaluated positions are not the same. Therefore, as the difference between the Gaussian points is small, the diagonal elements of the impedance matrix are much larger than the other elements, what makes the impedance matrix diagonally dominant.

3.7 Incident field modelling

There are several ways to model the excitation of filamentary problems, that is, the incident field in the proposed model. In one of them, it is considered that the incident field exists only in the feeding segments. In other words, it can be modelled by replacing the feeding segment by a gap in which a discrete source is connected. Thus, the tangential incident field $E^t_{inc}(\mathbf{r})$ is given by the ratio between the voltage V_0 applied by the source in this segment with length Δ:

$$E^t_{inc}(\mathbf{r}) = \begin{cases} \dfrac{V_o}{\Delta} & \text{, in the feeding segment} \\ 0 & \text{, otherwise} \end{cases} \tag{3.47}$$

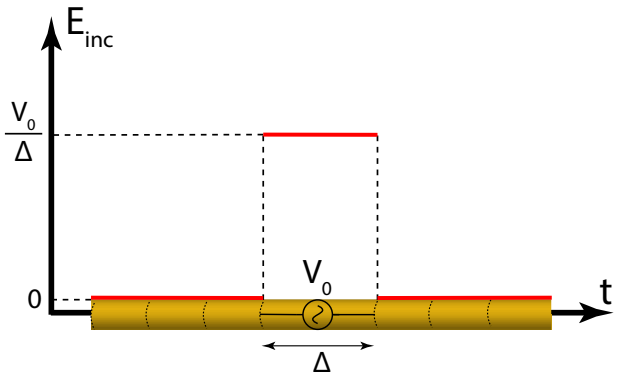

Figure 3.5 – Delta-gap source.

That is called the delta-gap source and it is represented in 3.5. Due to its simplicity and to the fact that only the weighting functions that have support in the feeding segment must be calculated, it makes this model computationally efficient. On the other hand, it can also lead to some inaccuracy in the post-processing results directly related to the current, such as input impedance and return loss. However, this error is attenuated in

the field calculation, and it conducts to more precise near field and radiation patterns results (GIBSON, 2015).

3.8 Lumped element modelling

In the design of coils for RWPT as well as resonant subwavelength metamaterial structures, it is common to use discrete electronic components for tuning the resonant frequency, compensating reactance and matching impedance. Therefore, in order to develop a method for RWPT systems analysis, it is convenient to take into account a discrete or lumped impedance contribution in the thin-wire EFIE.

A lumped element with impedance Z_{load} leads to a reduction of $\mathbf{E}_{load} = Z_{load}\mathbf{J}_s$ in the total electric field expressed in equation 3.1, thus:

$$\mathbf{E}_T = \mathbf{E}_{inc} + \mathbf{E}_s - \mathbf{E}_{load}, \tag{3.48}$$

Consequently, this lumped impedance contribution must be considered in the thin-wire EFIE formulation:

$$\hat{\mathbf{n}}\times\mathbf{E}_{\mathbf{inc}}(\mathbf{r}) = \hat{\mathbf{n}}\times\left[\frac{j}{4\pi\omega\varepsilon}\int_{t'} k^2\mathbf{I}(t')\Psi(\mathbf{r},\mathbf{r}') - [\boldsymbol{\nabla}\cdot\mathbf{I}(t'))]\boldsymbol{\nabla}\Psi(\mathbf{r},\mathbf{r}')\,\mathrm{d}t' \; + Z_{load}\mathbf{I}(t')\right]. \tag{3.49}$$

By applying the MoM, the resulting linear system indicated in 3.31 is modified. Now, the impedance matrix is a sum of the distributed impedance matrix $\mathbb{Z}$, which elements can be found through 3.33, with the lumped impedance matrix $\mathbb{Z}^{load}$:

$$\mathbb{V}_{(N\times 1)} = \left[\mathbb{Z}_{(N\times N)} + \mathbb{Z}^{load}_{(N\times N)}\right]\cdot\mathbb{I}_{(N\times 1)}, \tag{3.50}$$

The elements of the lumped impedance matrix, in turn, are given by:

$$\mathbb{Z}^{load}_{i,j} = \int_t Z_{load} w_i(t) u_j(t') \left(\hat{t}\cdot\hat{t}'\right)\,\mathrm{d}t. \tag{3.51}$$

Even though both distributed and lumped impedance matrices have the same dimension, the way each one operates in the segments is fundamentally different, as it can be seen in the equation for their elements. In the distributed impedance matrix $\mathbb{Z}$, the double integral is performed in the observer and source segments. Then, each source segment is tested with all observer ones. Therefore, this is a symmetrical matrix. On the other hand, the single integral in the equation for the lumped impedance matrix is held only in the observer segment that contains the lumped element. Thus, this is a sparse matrix with non-zero elements only in the rows related to that segment.

Finally, by developing the numerical formulation for $\mathbb{Z}^{load}_{i,j}$ as done for $\mathbb{Z}_{i,j}$ in section 3.6.3, the elements of the lumped impedance matrix can be numerically evaluated as:

$$\mathbb{Z}^{load}_{i,j} = \frac{Z_{load}}{4\Delta\Delta'}\sum_{\substack{sgn=1\\ sgn'=1}}^{2}\left[(\Delta x\Delta x' + \Delta y\Delta y' + \Delta z\Delta z')\left(G_1^L + G_2^L + G_3^L\right)\right] \tag{3.52}$$

where the auxiliary integrals $G_1^L - G_3^L$ are given by:

$$G_1^L = \int_{-1}^{1} 1 - (-1)^{sgn'} \alpha' \, \mathrm{d}\alpha \tag{3.53a}$$

$$G_2^L = \int_{-1}^{1} -(-1)^{sgn} \alpha \, \mathrm{d}\alpha \tag{3.53b}$$

$$G_3^L = \int_{-1}^{1} (-1)^{sgn} (-1)^{sgn'} \alpha\alpha' \, \mathrm{d}\alpha. \tag{3.53c}$$

3.9 Post-processing calculations

The EFIE solved through MoM returns the current across the entire filamentary structure under analysis. Consequently, this current can be used to calculate the field at any point in space by applying the scattering and radiation in equation 3.3. Moreover, this current can be used to calculate many other useful parameters directly linked to it, such as input impedance, return loss, reflection coefficient and voltage standing wave ratio. In this section, these post-processing calculations are developed in order to be computationally implemented.

3.9.1 Current and impedance related parameters

The solution of the linear system 3.31 (or 3.50), considering the basis and weighting functions as nodal triangle functions, implies that the resulting current matrix $\mathbb{I}$ corresponds to the value of the current at each node, that is, at each triangle vertex. In addition to it, as shown in equation 3.39, each segment supports two half-triangles (linear) function, one decreasing and another one increasing, so the current at any point of this segment is given by the superposition of each half-triangle.

Alternatively, it can also be calculated by linear interpolation. Considering a segment defined from a node t_i, in which the calculated value of the current is I_i, to a node t_f in the opposite extremity with current I_f. The current at any point t on this segment is given by:

$$I(t) = \left(\frac{I_i - I_f}{t_i - t_f} \right) t - \left(\frac{I_f t_i - I_i t_f}{t_i - t_f} \right), \tag{3.54}$$

that is exactly the superposition of the half-triangle functions in this segment.

If the filamentary structure is excited by a discrete (delta-gap) source with a voltage V_o, and by approximating the current I_o flowing through the source as the current at the feeding segment midpoint, that is:

$$I_o = \frac{I_f - I_i}{2}, \tag{3.55}$$

the input impedance Z_{in} seen by the source at its terminals is given by:

$$Z_{in} = \frac{V_o}{I_o}. \tag{3.56}$$

From the input impedance, the reflection coefficient S_{11}, the Return Loss (RL), and the Voltage Standing Wave Ratio (VSWR) can be calculated as (POZAR, 2011):

$$S_{11} = \frac{Z_{in} - Z_o}{Z_{in} + Z_o}, \tag{3.57}$$

$$\text{RL} = -20\log_{10}(S_{11}) \text{ dB}, \tag{3.58}$$

$$\text{VSWR} = \frac{1 + |S_{11}|}{1 - |S_{11}|}, \tag{3.59}$$

where Z_o is the reference impedance that is, the characteristic impedance of the transmission line that connects the power source to the filamentary structure.

3.9.2 Field results

According to the total electric and magnetic field expressed by equations 3.3 and 3.4, respectively, and considering the thin-wire approximation for the integro-differential operators $\mathcal{L}(\mathbf{J_s})$ and $\mathcal{K}(\mathbf{J_s})$, the electric and magnetic fields radiated by a filamentary structure are given by:

$$\mathbf{E}(\mathbf{r}, \mathbf{r}') = -\frac{j\eta}{4\pi k}\int_{t'} k^2\mathbf{I}(t')\Psi(\mathbf{r}, \mathbf{r}') - [\boldsymbol{\nabla}\cdot\mathbf{I}(t'))]\boldsymbol{\nabla}\Psi(\mathbf{r}, \mathbf{r}')\ \mathrm{d}t', \tag{3.60}$$

$$\mathbf{H}(\mathbf{r}, \mathbf{r}') = -\frac{1}{4\pi}\int_{t'} \mathbf{I}(t') \times \boldsymbol{\nabla}\Psi(\mathbf{r}, \mathbf{r}')\ \mathrm{d}t'. \tag{3.61}$$

Expanding the equations 3.60 and 3.61 into the Cartesian coordinate directions and developing the involved algebraic and vector operations, the components of the electric and the magnetic field radiated by the analysed structure are given by:

$$E_x(\mathbf{r}, \mathbf{r}') = -\frac{j\eta k^2}{4\pi}\int_{t'} k^2 I(t')\left[(G_E + G_H)\frac{\Delta x'}{\Delta'} - k^2(\hat{t}'\cdot\mathbf{R})(x - x')G_{EH}\right]\ \mathrm{d}t', \tag{3.62a}$$

$$E_y(\mathbf{r}, \mathbf{r}') = -\frac{j\eta k^2}{4\pi}\int_{t'} k^2 I(t')\left[(G_E + G_H)\frac{\Delta y'}{\Delta'} - k^2(\hat{t}'\cdot\mathbf{R})(y - y')G_{EH}\right]\ \mathrm{d}t', \tag{3.62b}$$

$$E_z(\mathbf{r}, \mathbf{r}') = -\frac{j\eta k^2}{4\pi}\int_{t'} k^2 I(t')\left[(G_E + G_H)\frac{\Delta z'}{\Delta'} - k^2(\hat{t}'\cdot\mathbf{R})(z - z')G_{EH}\right]\ \mathrm{d}t', \tag{3.62c}$$

$$H_x(\mathbf{r},\mathbf{r}') = -\frac{k^3}{4\pi}\int_{t'} I(t')\left[\frac{\Delta y'}{\Delta'}(z-z') - \frac{\Delta z'}{\Delta'}(y-y')\right] G_H \, \mathrm{d}t', \tag{3.63a}$$

$$H_y(\mathbf{r},\mathbf{r}') = -\frac{k^3}{4\pi}\int_{t'} I(t')\left[\frac{\Delta z'}{\Delta'}(x-x') - \frac{\Delta x'}{\Delta'}(z-z')\right] G_H \, \mathrm{d}t', \tag{3.63b}$$

$$H_z(\mathbf{r},\mathbf{r}') = -\frac{k^3}{4\pi}\int_{t'} I(t')\left[\frac{\Delta x'}{\Delta'}(y-y') - \frac{\Delta y'}{\Delta'}(x-x')\right] G_H \, \mathrm{d}t', \tag{3.63c}$$

where the inner product between the unitary vector $\hat{t}'$ tangential to the structure at the source point and the position vector $\mathbf{R}$ between the source and observation point is:

$$\hat{t}' \cdot \mathbf{R} = \frac{\Delta x'}{\Delta}(x-x') + \frac{\Delta y'}{\Delta}(y-y') + \frac{\Delta z'}{\Delta}(z-z') \tag{3.64}$$

Moreover, the auxiliary functions G_E, G_H, and G_{EH} are defined as follows:

$$G_E = \frac{1}{k}\Psi(\mathbf{r},\mathbf{r}'), \tag{3.65a}$$

$$G_H = \left[\frac{1+jkR}{(kR)^2}\right] G_E, \tag{3.65b}$$

$$G_{EH} = \frac{3G_H - G_E}{(kR)^2}, \tag{3.65c}$$

with R being the module of the position vector $\mathbf{R}$.

When the distance R between the observer and source points is such that $R \gg \lambda$, some of the electric and magnetic field components are cancelled, what allows a significant simplification in the field equations at the far-field region (BALANIS, 2016). However, as the RWPT systems and the resonant metamaterials under analysis in this work operate in the near-field region, the far-field equation does not need to be implemented.

3.10 Numerical results of the thin-wire model

The MoM solution for the thin-wire model described in the previous sections was implemented in Matlab® and all the results presented in this work were achieved in a computer with an Intel® Core™ i7-8750H processor, 16 GB RAM, and 2.21 GHz clock.

In order to evaluate the accuracy of the proposed model for thin-wire structures, three case studies are analysed: a half-wave dipole antenna, a full-wave loop antenna, and a full-wave loop antenna with a loading coil. The reference solutions for each analysis were obtained by using the computational electromagnetic design software FEKO®, which is based on the MoM solution for the integral formulation of Maxwell's equations

(JAKOBUS et al., 2008). Thus, the error metric applied in the following analysis is based in the euclidean norm $\mathcal{L}_2$ and it can be defined as:

$$\epsilon_X = \left| \frac{\mathcal{L}_2(X_{MoM}) - \mathcal{L}_2(X_{ref})}{\mathcal{L}_2(X_{ref})} \right| \tag{3.66}$$

where ϵ_X is the error related to the parameter X, X_{MoM} is the solution obtained through the implementation of the proposed model, and X_{ref} is the reference solution. This metric can be understood as the normalised distance from the calculated solution to the expected value.

Another metric used in the following analysis is the reciprocal condition number $\mathcal{R}_c$ of the impedance matrix, and it is defined as the ratio of its smallest to the largest singular values. This metric can assume values between zero and one in such a way that for values closer to zero, the matrix is named ill-conditioned whereas, for values closer to one, it is classified as well-conditioned. It is also a measurement of the solution sensitivity to perturbations (LUO; TSENG, 1994). In other words, in an ill-conditioned system, any small variation in the excitation matrix will lead to a significant variation in the solution, that is, the current matrix. As this solution is used as a starting point for all post-processing calculations, its sensitivity to perturbations will also affect the other results.

3.10.1 Half-wave dipole antenna

The first case analysed is a half-wave dipole at the frequency of $300\ MHz$, constituted by a wire with total length $\lambda/2 = 0.5\ m$. As illustrated in Figure 3.6, this structure is centre fed by a time-harmonic source with a voltage of amplitude $1\ V$.

Before addressing the numerical analysis, some general aspects of the implementation have to be highlighted. First, the code receives as an input a text file that contains the Cartesian coordinates that describe the geometry of the structure as well as its diameter, the location and amplitude for the excitation and lumped elements, and the frequency range under analysis. Then, each structure is discretized into nodes and segments, which are the line segments between each node pair, as indicated in Figure 3.6. The number of discretization nodes is calculated based on a scaling factor defined as the ratio between the desired segment length l_{seg} and the wire diameter $2a$:

$$\text{scale} = \frac{l_{seg}}{2a} \tag{3.67}$$

For example, if scale $= 10$ the structures will be discretized so that each segment will be ten times greater than the wire diameter. Thus, it is somehow possible to assure whether the thin wire condition is being obeyed or not.

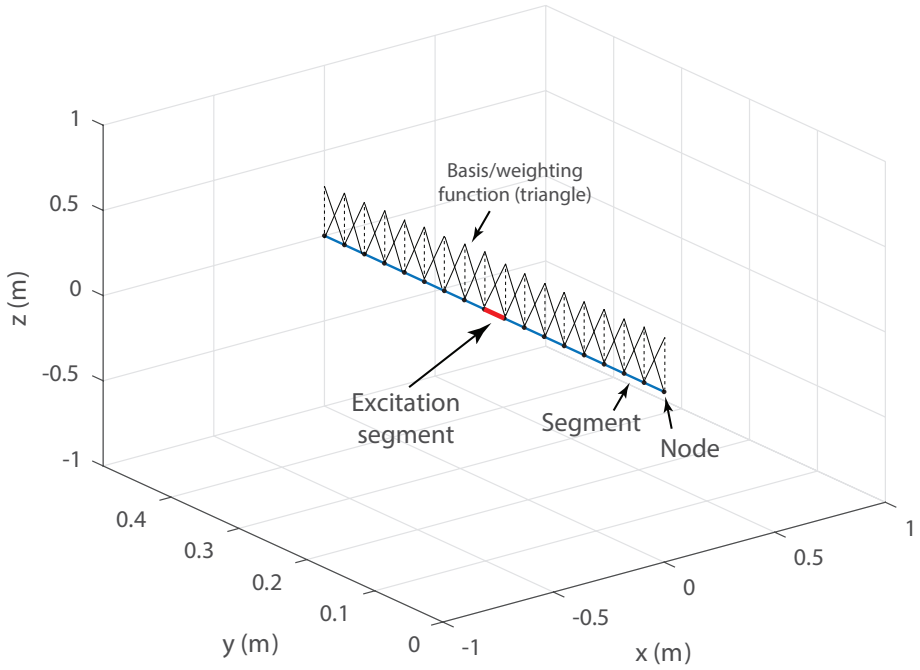

Figure 3.6 – Implementation and discretization of a half-wave dipole antenna.

Based on this discretization, the basis and weighting functions are assigned in a way that each node corresponds to a triangle function vertex. Consequently, each segment is associated with two linear-piecewise functions, an increasing and a decreasing function. After that, the excitation and lumped elements segments are assigned based on their Cartesian coordinates. Finally, for each geometry, excitation source, and lumped elements, a class is created in which the data required for the following calculations are structured as objects.

Firstly, the accuracy of the implemented model is analysed as a function of the structure discretization. To this end, the parameter scale was varied from 1 to 20. The error of the current on the wire as a function of the parameter scale is presented in Figure 3.7. As it can be seen, this error increases along with the segment size in a way that smaller the nodes, the more significant the error. However, when the segment size is equal or smaller than the wire diameter, the error also increases, since the thin-wire condition is violated. Therefore, for this case, the smallest error is achieved when the scale factor is equal to two; besides, the error is over 5% only for scale factors higher than eight.

It is important to observe that, in this work, when it is stated that the thin-wire condition is violated it means that the boundaries established in the model definitions ($a \ll \lambda$ and $a \ll L$) are not obeyed in this particular case, either by the structure discretization or by the numerical evaluation of the integrals.

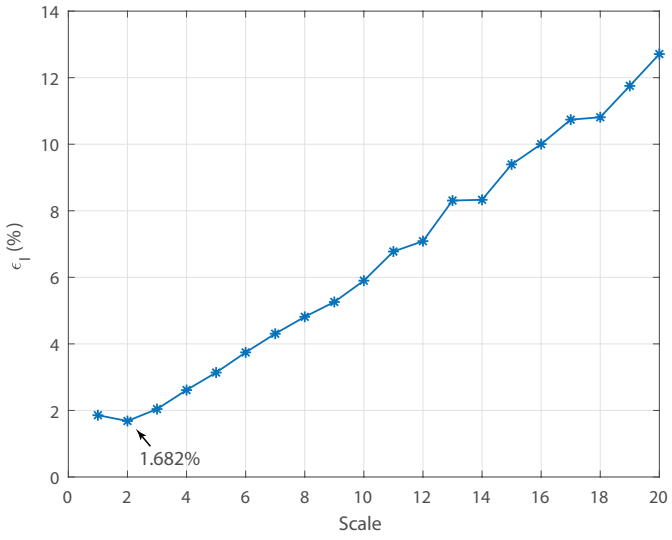

Figure 3.7 – Error of the calculated current on the half-wave dipole as a function of its discretization.

Thereby, the error was evaluated for the field components calculated in the evenly spaced observation points located on a line parallel and $\lambda/4$ apart from the dipole structure. Once the electric field component at the direction $\hat{z}$ and the magnetic field components at the directions $\hat{x}$ and $\hat{y}$ are null for these points, they are disregarded in the error analysis. The field error as a function of the scale factor for the remaining field components is shown in Figure 3.8. Here, the results reveal more acutely the effect of violating the thin-wire condition. When the segments are equal or smaller than the wire diameter, the error sharply grows. On the other hand, for large segments, the error also increases, but not at the same pace. The minimum error for the field results is obtained with a scale factor around four and five.

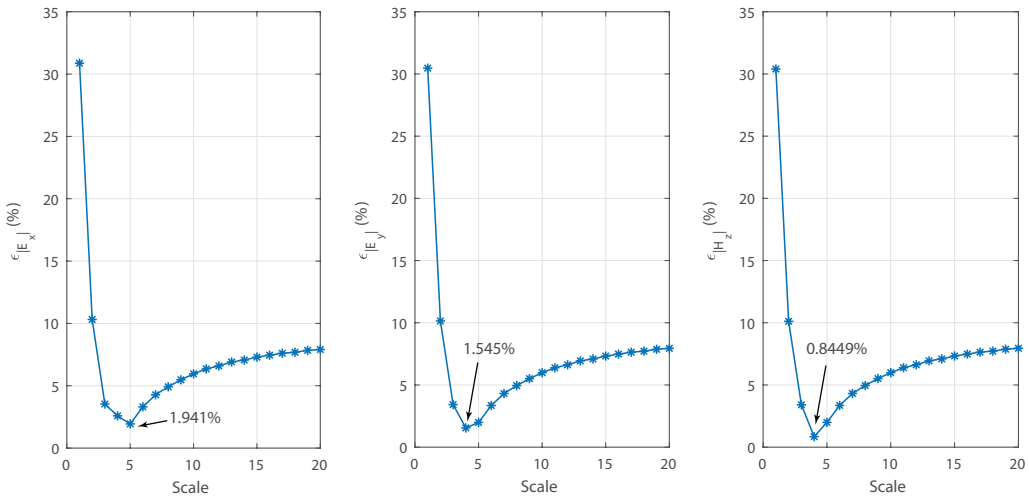

Figure 3.8 – Error of the calculated fields components radiated by the half-wave dipole as a function of its discretization.

Then, as indicated in Figure 3.9, the reciprocal condition decreases as the segment size is reduced; thus, the linear system is more susceptible to small variations, and it becomes more ill-conditioned. This behaviour is due to the violation of the thin-wire condition. Also, the singularity on the evaluated integrals becomes more significant for a shorter segment size. Moreover, as expected, larger segments lead to smaller linear systems, thus reducing the processing time.

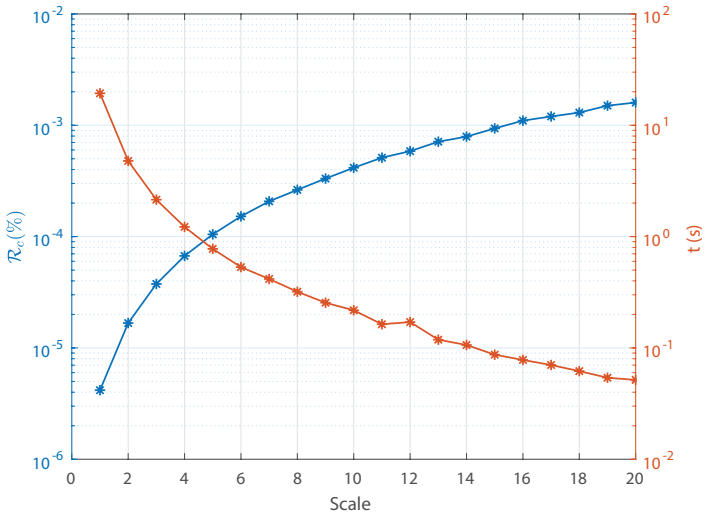

Figure 3.9 – Reciprocal condition number and processing time for the half-wave dipole solution as a function of its discretization.

The error for the calculated current and field values are also analysed as a function of the wire diameter, considering the scale factor equal to four once it led to the minimum overall error. As the fixed scale parameter links both wire diameter and segment size, the behaviours are similar to those previously presented. For instance, the current error as a function of the wire diameter is displayed in Figure 3.10.

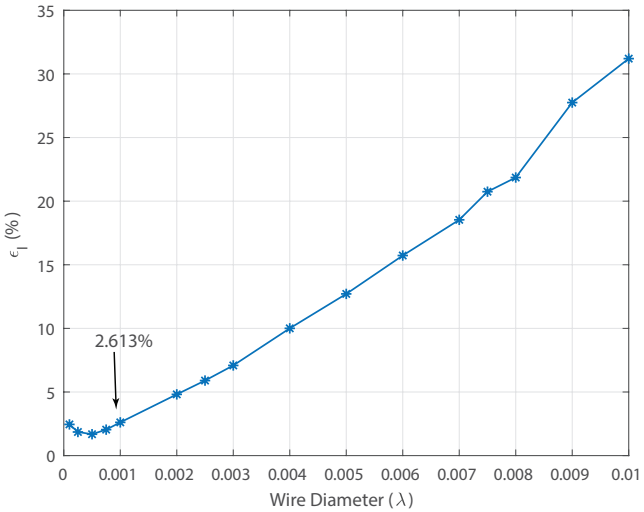

Figure 3.10 – Error of the calculated current on the half-wave dipole as a function of the wire diameter.

When the wire diameter increases, the size of the segments also increases, and the same happens for the error since the structure becomes less discretized. Furthermore, the wire diameter approaches the wavelength, and, in this case, the thin-wire approximation is no longer valid. On the other hand, when the wire diameter is reduced, the effect of singularities in the integrals becomes more prominent, thus increasing the error. The same pattern can be verified for the field error plotted in Figure 3.11. As a consequence, the matrix becomes more ill-conditioned as the diameter reduces and the processing time increases, as shown in Figure 3.12. In this case, the wire diameter that minimises the error is around $10^{-3}\lambda$.

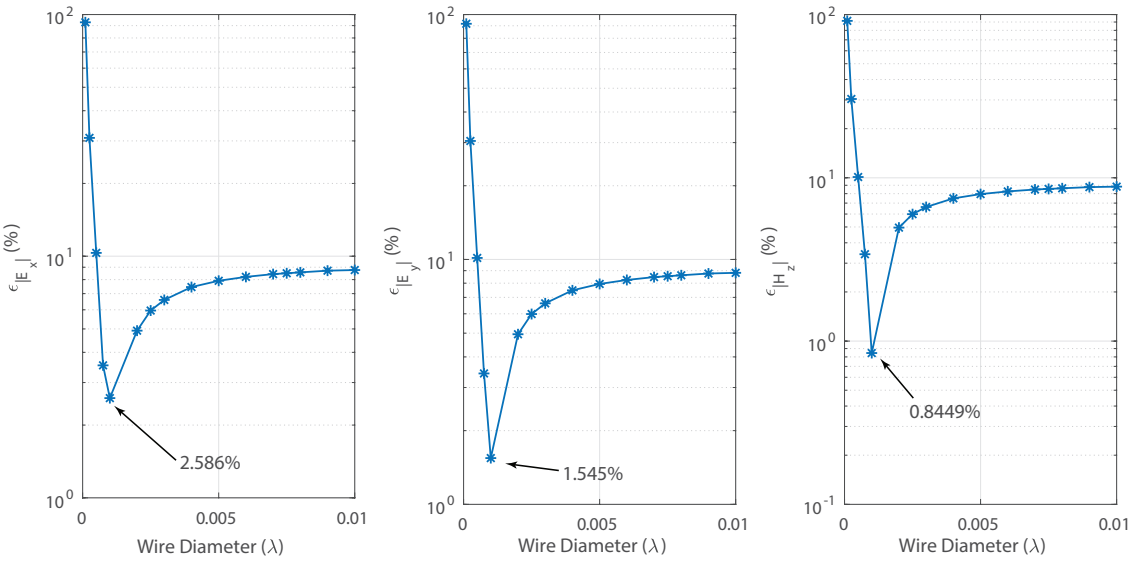

Figure 3.11 – Error of the calculated fields components radiated by the half-wave dipole as a function of the wire diameter.

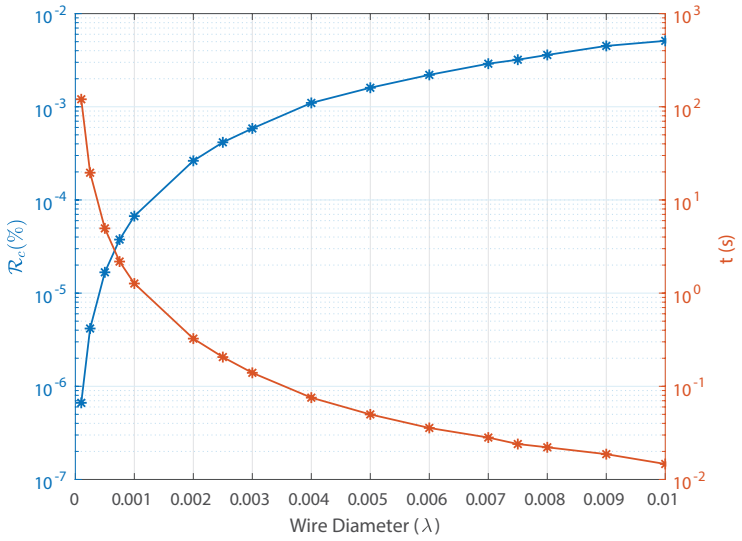

Figure 3.12 – Reciprocal condition number and processing time for the half-wave dipole solution as a function of the wire diameter.

Finally, after determining the wire diameter range in which the proposed model is valid and the optimum number of nodes that discretizes the half-wave dipole antenna, the number of Gauss points that minimizes the error on the evaluation of the integrals must be found. For this, the implemented code was executed with all arrangements of Gauss points for the observer and source segments. The error for each combination is indicated in Figure 3.13. As it can be noticed, the error increases along with the number of Gauss points. It can be understood once in the Gaussian quadrature integration, each segment is further discretized, thus it can also violate the thin-wire condition. Conversely, when a small number of Gauss points is used, the integral cannot be evaluated appropriately. Therefore, the combinations that leads to the minor error is three Gauss points for the observer and two for the source segment. As the error variation in this analysis is lower when compared with the previous cases, only the error of the calculated current is presented.

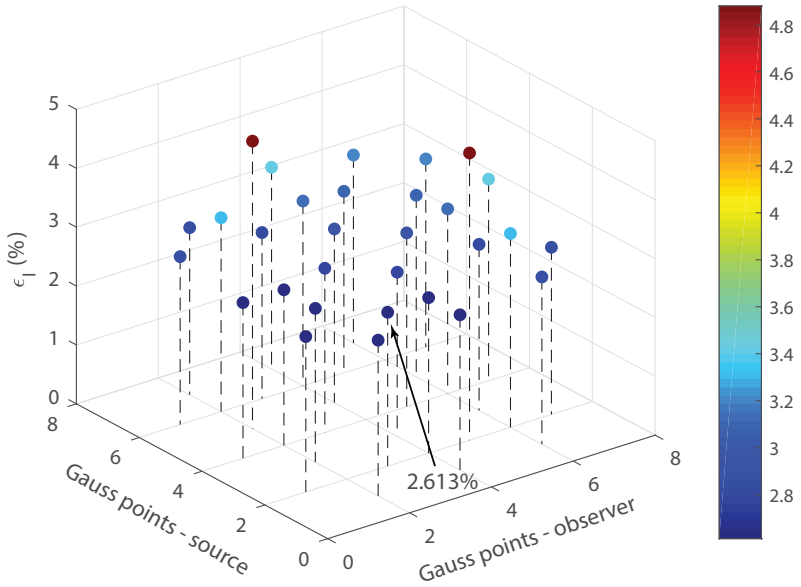

Figure 3.13 – Error of the calculated current on the half-wave dipole as a function of the combination of Gauss points for observer and source segments.

Based on the previous analysis, the set of optimum parameters that leads to the smallest error can be determined. In this specific case of a half-wave dipole at $300\ MHz$, it is accomplished when the wire diameter is $1\ mm$, with the scale factor equal to four, three Gauss points for the observer and two for the source. The results for electric current distribution magnitude in the dipole, reflection coefficient, and the amplitude of electric and magnetic fields are presented in the graphs in Figures 3.14, 3.15, and 3.16, respectively. As it can be seen, the electromagnetic behaviour of a half-wave dipole antenna can be accurately described by the proposed implementation.

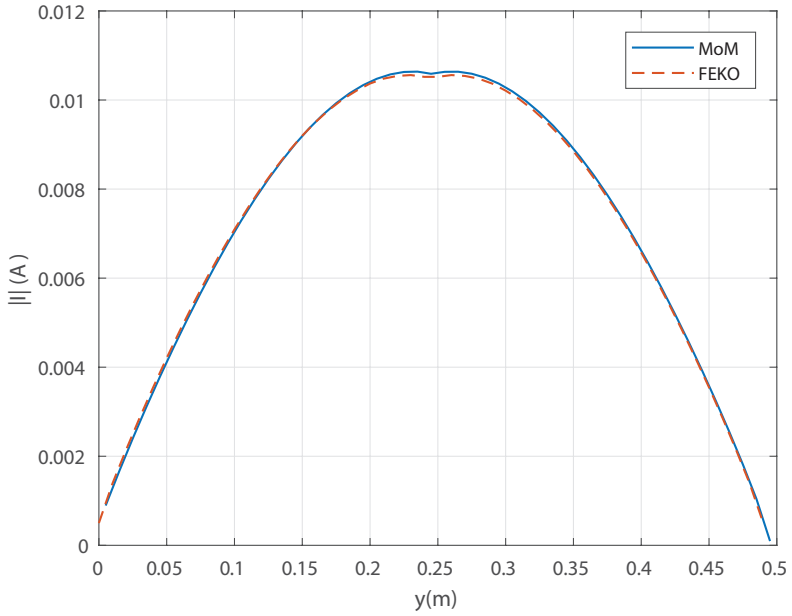

Figure 3.14 – Comparison of the electric current distribution magnitude in a half-wave dipole antenna at $300\ MHz$ using MoM and FEKO.

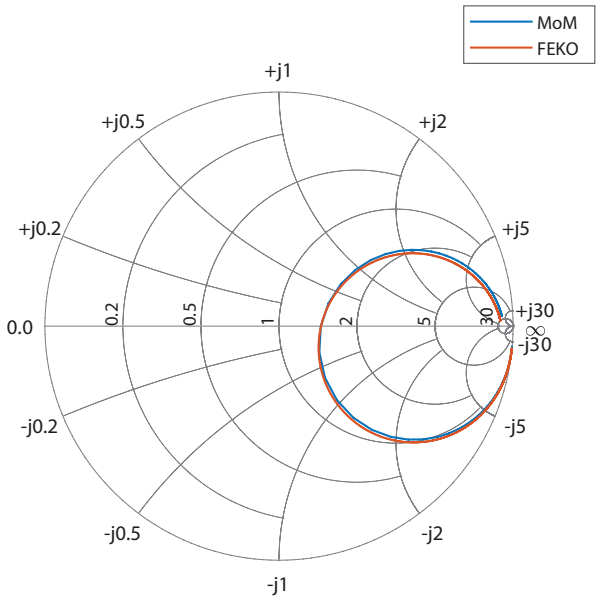

Figure 3.15 – Comparison of the reflection coefficient of a half-wave dipole antenna from $1\ MHz$ to $500\ MHz$ using MoM and FEKO.

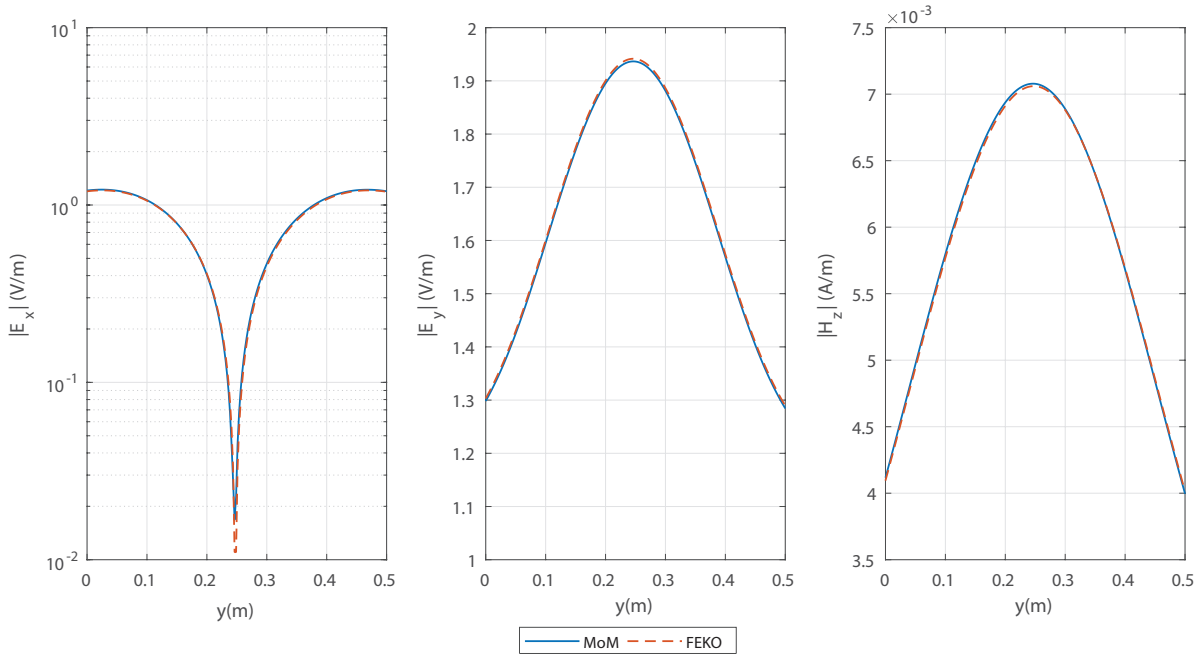

Figure 3.16 – Comparison of the electric and magnetic fields amplitudes in a half-wave dipole antenna at $300\ MHz$ using MoM and FEKO.

3.10.2 Full-wave loop antenna

Another case study used to evaluate the accuracy of the proposed model is the implementation of a full-wave square loop antenna at $300\ MHz$, being the length of each side equal to $\lambda/4 = 0.25\ m$. As indicated in Figure 3.17, this antenna is fed by a time-harmonic source with a voltage of amplitude $1\ V$ located at the centre of one of its sides. For this case, two conditions are analysed: the loop antenna itself without lumped elements and a loop antenna with loading coil that is represented by a $100\ nH$ lumped inductor located at the centre of the opposite side to the excitation. Besides that, the same analysis carried out for the half-wave dipole antenna is applied to present cases.

The electric current distribution is evaluated in the antenna side in which the excitation segment is located, and it is analysed as a function of the discretization (scale factor) and the wire diameter for the cases with and without lumped elements (loading coil). The results of these analyses are presented in Figures 3.18a and 3.18b. Firstly, for the case with no lumped elements, it can be seen that the overall behaviour of the errors is similar to those verified in the half-wave dipole, in the sense that when the segment size or the wire diameter is too short, the error increases due to the violation of the thin-wire approximation conditions and also to the influence of singularities on the linear system result. Conversely, when the segment size is too large, the analysed structure is not sufficiently discretized, and the system does not converge for the expected result. In addition to it, when the wire diameter is too wide, the structure cannot be approximated as the thin-wire and the error increases.

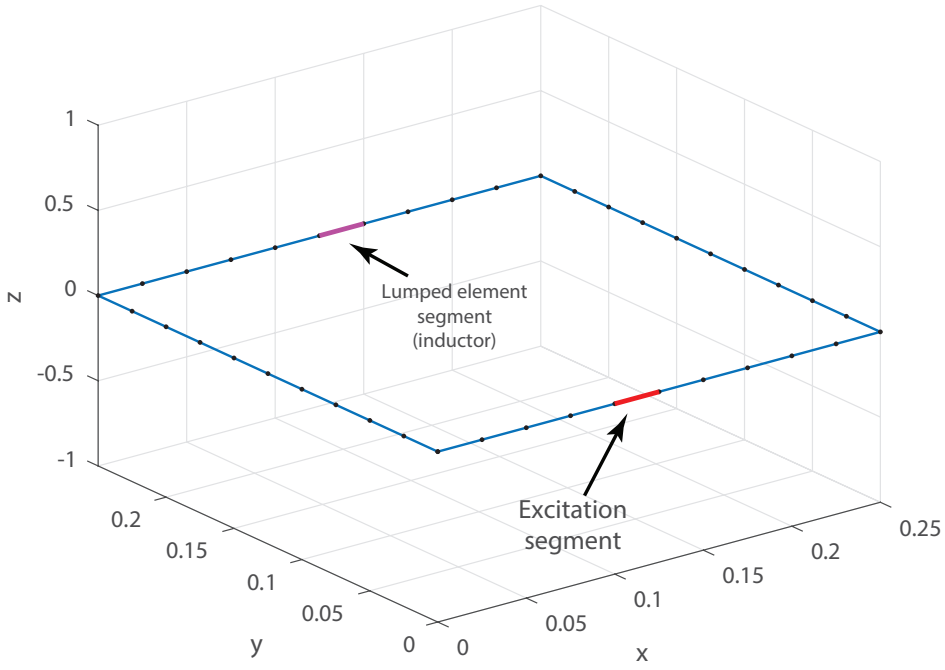

Figure 3.17 – Implementation and discretization of a full-wave loop antenna.

However, in both cases, an oscillation in the error can be seen. This behaviour is due to the manner in which the excitation segment is assigned. After the structure is discretized into segments, the algorithm verifies in which segment the provided excitation point is located. In most cases, it is located in between the two nodes at the excitation segment extremity. However, if the excitation point coincides with a node, the excitation is slightly displaced. When the number of segments is high, the effect of this displacement is not relevant, but it becomes significant as the segment size increases. In this particular case, as the error is evaluated on the antenna side in which the excitation segment is located, it is even more prominent.

For the case of the loop antenna with a loading coil, the behaviour of the current as a function of the scale factor is noticeably different. When the scale factor is low, that is, when the segment size is too short, the error is large and it decreases in indirect proportion to the scale factor. This can be explained by the fact that, as the segment length decreases, the singularities in the integrals evaluated for each segment leads to a sharp increase of the distributed impedance matrix elements, whereas the elements of the lumped impedance matrix do not grow in the same manner. Therefore, the contribution of the lumped elements is overshadowed as the scale factor decreases, and the proposed model is not valid anymore. On the other hand, if the segment size is too large, depending on the wire diameter, the structure cannot be appropriately discretized as it is shown in Figure 3.18b. Therefore, the scale factor that discretizes the structure

must be chosen by taking into account the wire diameter and the acceptable error level. In this specific case, for the antenna with a loading coil, a scale factor equal to eight is selected, considering a $1\ mm$ wire diameter.

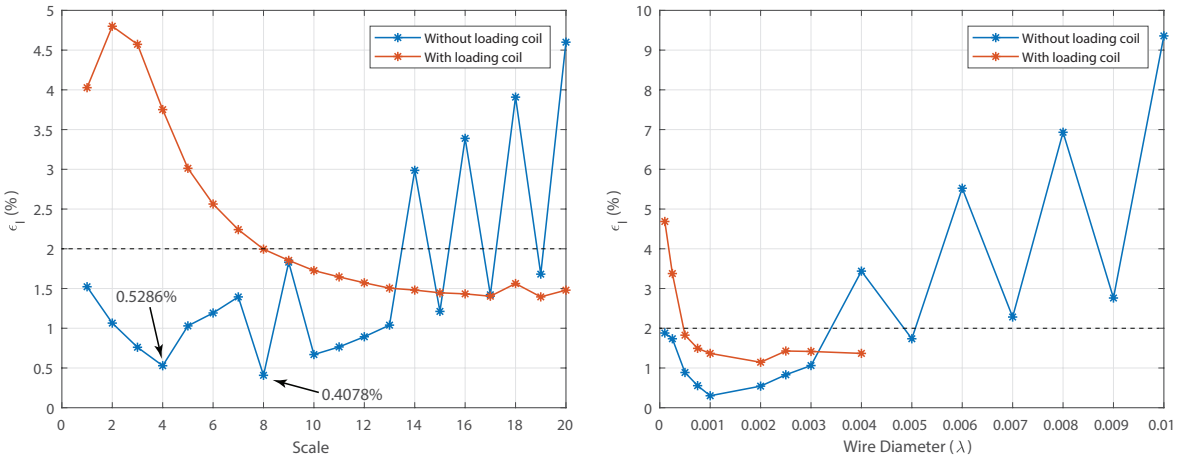

(a) Error as a function of the scale factor. (b) Error as a function of the wire diameter.

Figure 3.18 – Error of the calculated current on the full-wave loop with and without lumped elements

The error related to the magnitude of electric and magnetic field components are revealed in Figure 3.19a as a function of the scale factor and in Figure 3.19b in relation to the wire diameter. As it can be seen, the error behaviours for the field results support the conclusions presented in the analysis of the current error. For the antenna, without lumped elements, the minimum error is achieved for a scale factor in which the segment size is not too short to the point that does not obey the thin-wire approximation condition but not too large in a way that the structure cannot be sufficiently represented.

On the other hand, for the antenna with a loading coil, the error is inversely proportional to the scale factor, but the wire diameter limits the increase in the segment size. Thus, if the segment and wire diameter are large, the structure cannot be discretized. Furthermore, the oscillation in the error result is more significant for low amplitude field results, whereas for the other components, it is filtered by the integrals solved in the field evaluation.

The results for the reciprocal condition number and the processing time for both cases shown in Figures 3.20 and 3.21 are similar to those verified for the half-wave dipole, and this behaviour is characteristic for MoM implementations. When the segment length or the wire diameter is too short, the linear system becomes ill-conditioned, once the effects of the integral singularities are more expressive. Moreover, the processing time to evaluate each element of the linear system and to solve it is higher. Conversely, as the scale factor and the wire diameter increases, the system becomes well-conditioned.

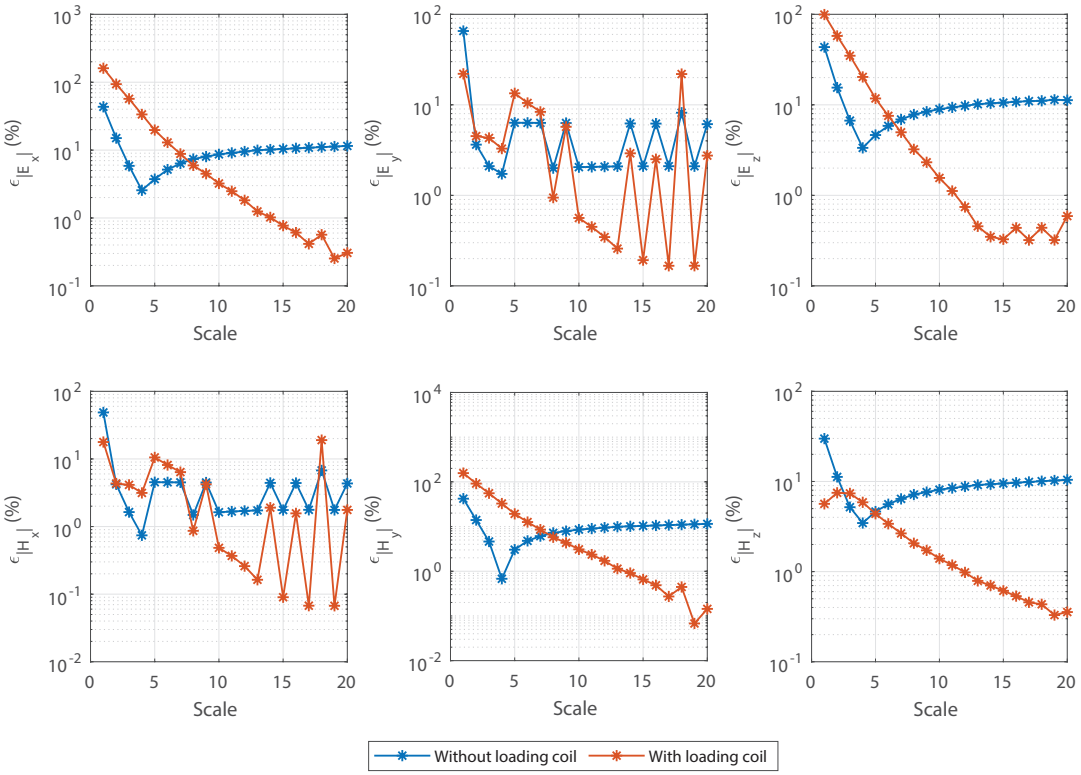

(a) Error as a function of the scale factor.

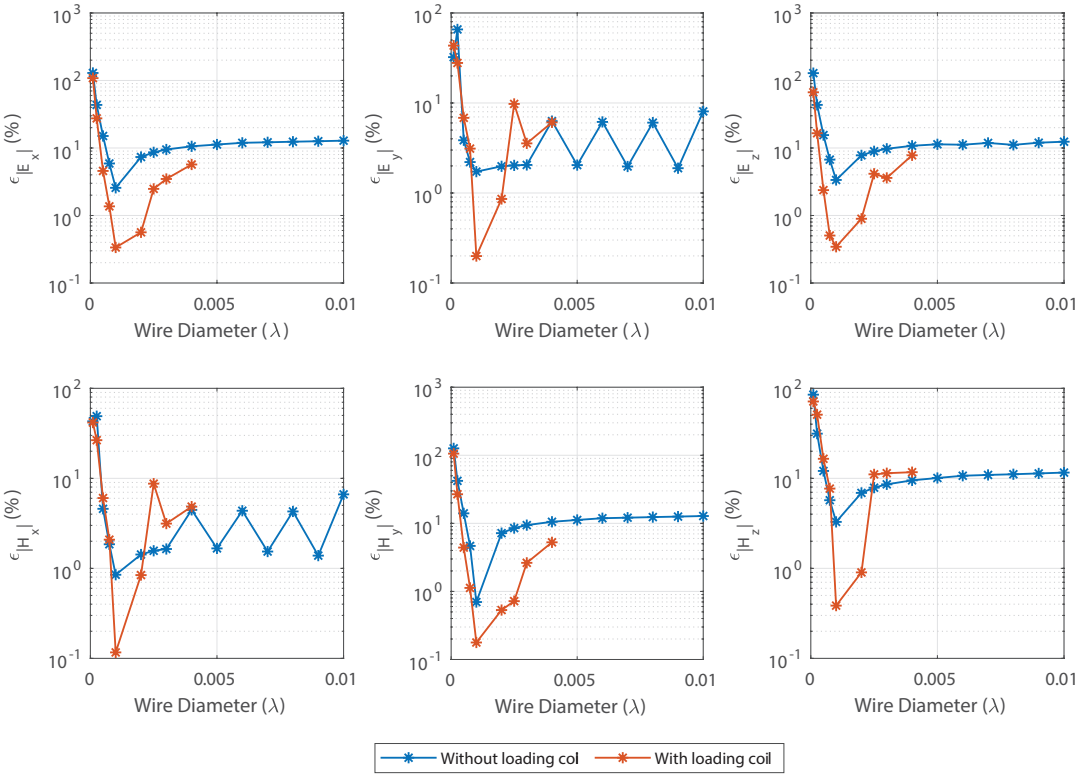

(b) Error as a function of the wire diameter.

Figure 3.19 – Error of the calculated fields components on the full-wave loop with and without lumped elements

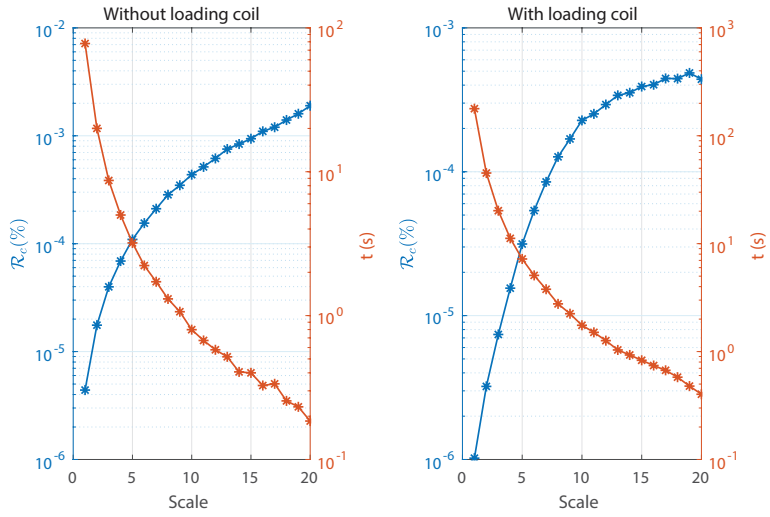

Figure 3.20 – Reciprocal condition number and processing time for the full-wave loop solution as a function of its discretization.

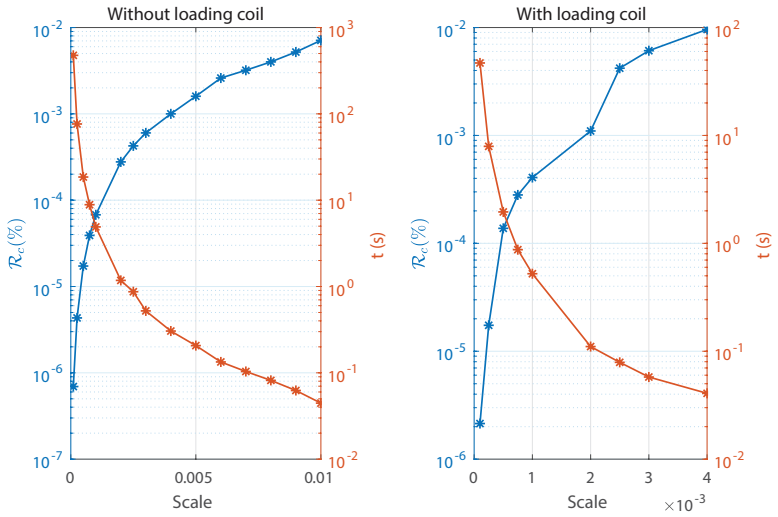

Figure 3.21 – Reciprocal condition number and processing time for the full-wave loop solution as a function of the wire diameter.

Finally, the relation between the number of Gauss points for the observer and source and the error for the current result is analysed for the full-wave loop antenna with and without loading coils. As indicated in Figure 3.22, in the first case, as well as for the half-wave dipole antenna, the error increases with the number of Gauss points. It happens once the best discretization for both cases leads to a high number of segments and, from the numerical point of view, it is better to have a more refined discretization than increasing the order of the interpolation polynomial that is related to the number of Gauss points.

In contrast, for the antenna with a loading coil, as the segment size cannot be too short, the error is reduced by choosing a number of Gauss points higher than the verified in

the antenna without lumped elements. Therefore, the best pair of numbers of Gauss points in the first case is one for the observer and four for the source, whereas for the situation with a lumped inductor is two points for the observer and five for the source.

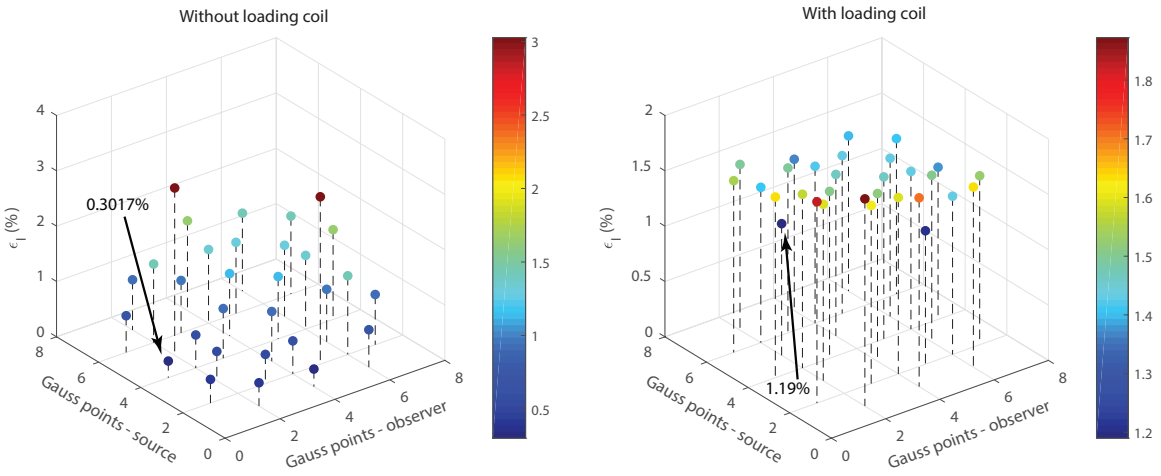

Figure 3.22 – Error of the calculated current on the full-wave loop as a function of the combination of Gauss points for observer and source segments.

Based on the best sets of numerical parameters established in the previous analyses, the implemented code was executed for the full-wave loop antenna with and without loading coils. Thereby, the results for electric current distribution presented in Figure 3.23, reflection coefficient in Figure 3.24, and electric and magnetic fields magnitude indicated in Figures 3.25 and 3.26 were generated.

As it can be seen, there is a displacement in the reflection coefficient as a function of the frequency. As the parametric analysis was carried out in the fixed frequency of $300\ MHz$, the best parameter set is valid for this frequency, leading to the minimum error. However, in order to get the minimum error over the frequency, the optimum parameter set must be chosen for each frequency individually. In the case of the antenna with a lumped inductor, the error for the reflection coefficient is higher. This is due to the fact that, as the discretization of this structure is limited, as shown in Figure 3.23b, the most expressive error happens at the excitation segment, that is where the current is evaluated for the reflection coefficient calculation, leading to the observed error.

Taking into account all the analysis accomplished in this section, it can be concluded that the results corroborate those obtained with commercial software and assure that the proposed approach is able to model thin-wire structures with arbitrary geometry and with lumped elements.

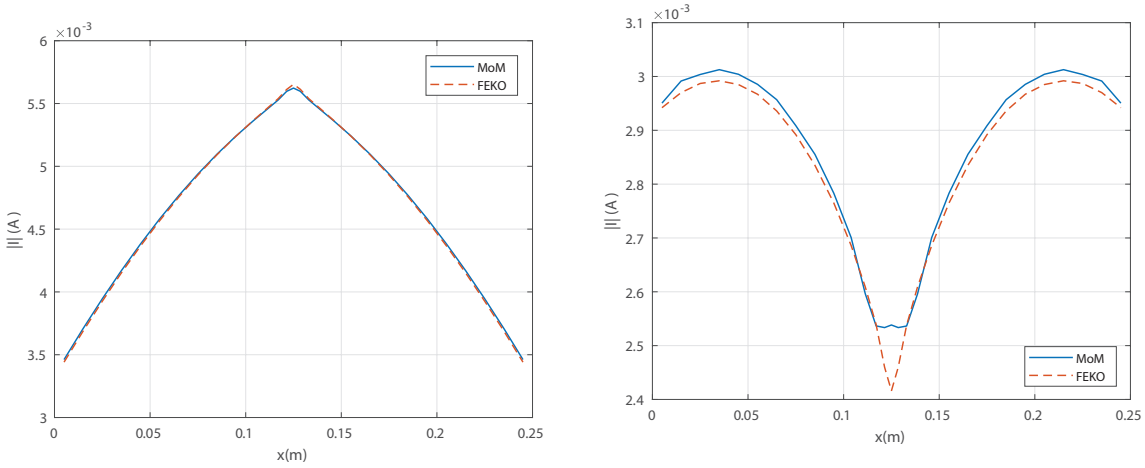

(a) Full-wave loop antenna

(b) Full-wave loop antenna with loading coil.

Figure 3.23 – Comparison of the electric current distribution magnitude in a full-wave loop antenna at $300\ MHz$ using MoM and FEKO.

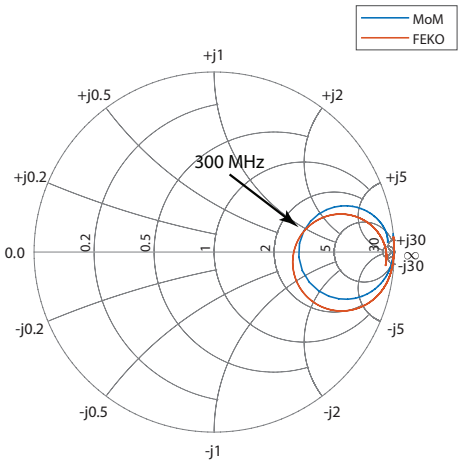

(a) Full-wave loop antenna

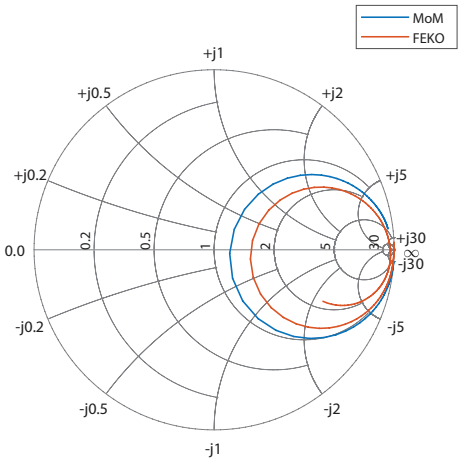

(b) Full-wave loop antenna with loading coil.

Figure 3.24 – Comparison of the reflection coefficient of a full-wave loop antenna from $1\ MHz$ to $500\ MHz$ using MoM and FEKO.

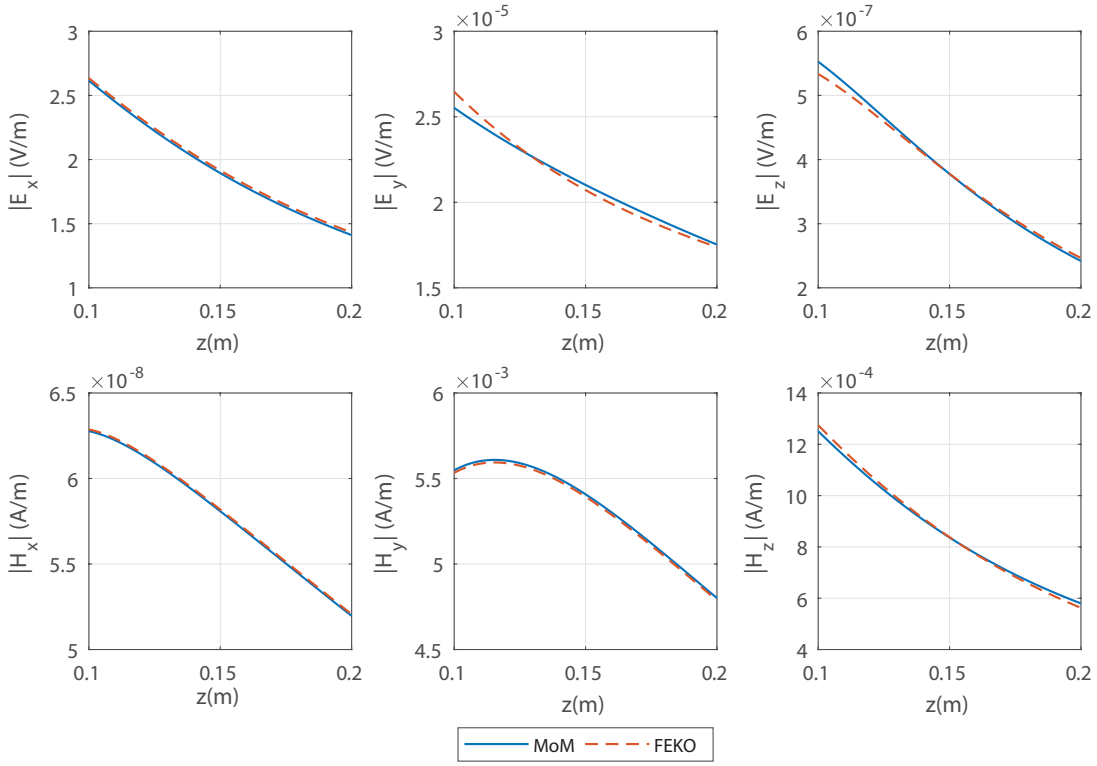

Figure 3.25 – Comparison of the electric and magnetic fields amplitudes in a full-wave loop antenna at $300\ MHz$ using MoM and FEKO.

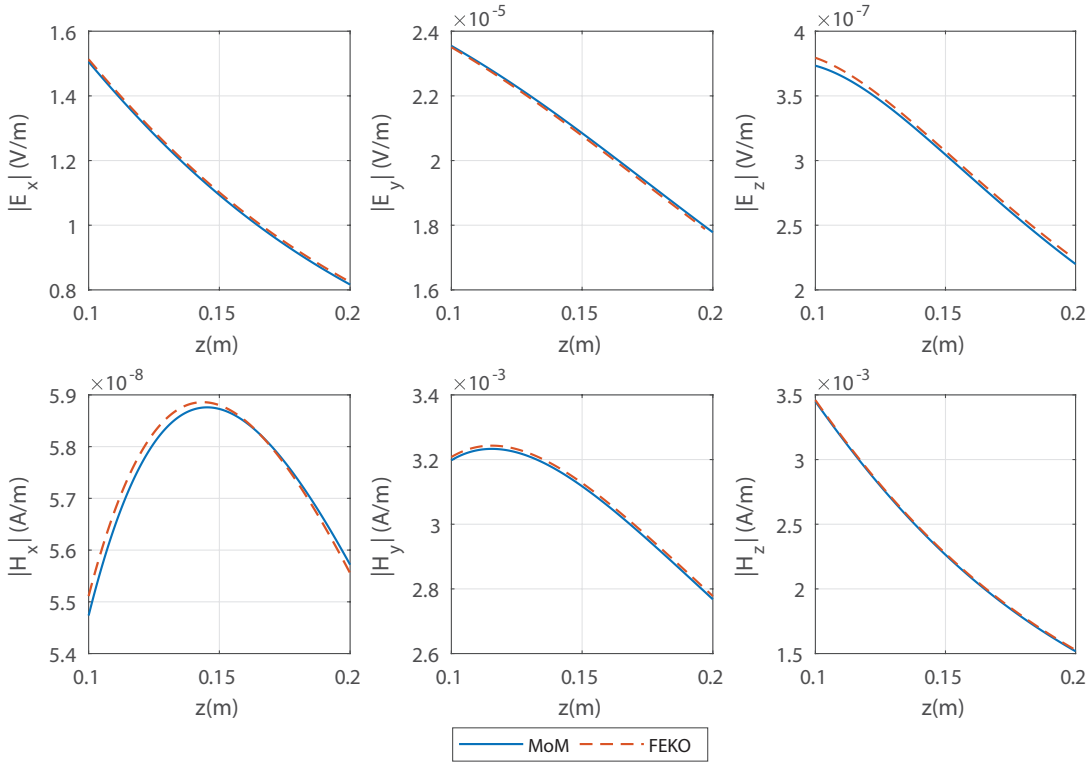

Figure 3.26 – Comparison of the electric and magnetic fields amplitudes in a full-wave loop antenna with loading coil at $300\ MHz$ using MoM and FEKO.

3.11 Thin-wire approximation for microstrip structures

The printed coils and resonators used in RWPT applications as well as the printed sub-wavelength resonant metamaterials, in general, operate at a frequency range in which the thin-wire approximation conditions are satisfied, that is, the radius a of microstrip line cross-section is such that $a \ll \lambda$, and the structure size $L \ll \lambda$. Therefore, the approach proposed in this work is that the thin-wire EFIE and its MoM implementation can be used as an approximation for the microstrip structures that obey these conditions.

However, some treatments have to be performed in order to apply the developed model to microstrip structures. In this section, these treatments related to the structure geometry and the contribution of the dielectric material are incorporated in the thin-wire EFIE numerical solution.

Consider a microstrip structure surrounded by free-space and constituted by a conductive line with width w_f, conductive layer thickness t_c and arbitrary geometry printed over a dielectric substrate with thickness h_s, relative electric permittivity ε_r and loss tangent $\tan\delta$, as represented in Figure 3.27a. Since in the most printed circuit boards copper is used in the conductive layer and has one of the highest conductivities among the metals, it is reasonable to assume the conductive layer as PEC. However, the microstrip line cross-section is rectangular, whereas the cross-section considered in the thin-wire modelling is circular. As it can be seen in Figure 3.27b, a manner to get around this is by calculating the equivalent diameter d that leads to a circular cross-section with the same area as the microstrip line cross-section (PEREIRA, 2016), thus:

$$d = \sqrt{\frac{4 w_f t_c}{\pi}}. \tag{3.68}$$

Two different media surround the microstrip line, the dielectric substrate with relative electric permittivity ε_r and the free space. An effective medium can be defined as a homogeneous dielectric in which a transmission line presents the same properties, particularly the propagation constant, of the corresponding microstrip line (BALANIS, 2016). This effective medium is characterized by its effective electric permittivity ε_r^{eff}, which expression depends on the ratio between the microstrip width w_f and the substrate thickness h_s (BAHL; TRIVEDI, 1977):

$$\varepsilon_r^{eff} = \begin{cases} \dfrac{\varepsilon_r + 1}{2} + \dfrac{\varepsilon_r - 1}{2}\left[\left(1 + 12\dfrac{h_s}{w_f}\right)^{-\frac{1}{2}} + 0.04\left(1 - \dfrac{w_f}{h_s}\right)^2\right] & , \text{if } \dfrac{w_f}{h_s} \leq 1 \\ \dfrac{\varepsilon_r + 1}{2} + \dfrac{\varepsilon_r - 1}{2}\left(1 + 12\dfrac{h_s}{w_f}\right)^{-\frac{1}{2}} & , \text{if } \dfrac{w_f}{h_s} \geq 1 \end{cases}. \tag{3.69}$$

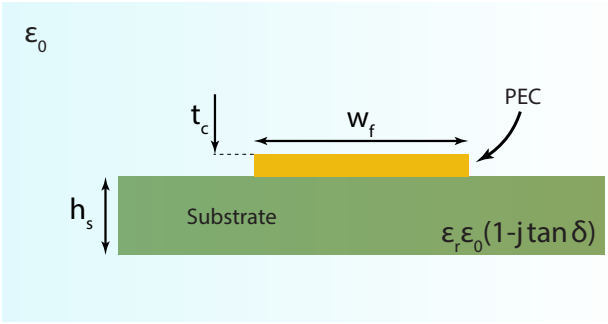

(a) Cross-section of a real microstrip line.

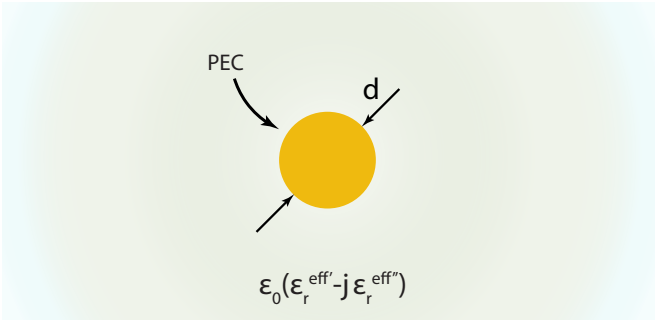

(b) Thin-wire approximation and effective electric permittivity.

Figure 3.27 – Thin-wire approximation for thin microstrip structures.

However, the effective electric permittivity depends on the frequency, and the dispersive effects represented by the loss tangent must be taken into account. This can be accomplished by applying the multipole Debye model, which is a physical model that describes the behaviour of the complex electric permittivity in the frequency domain. In this model, the lossy medium is represented as the RC network with N branches indicated in Figure 3.28, with $R = \varepsilon_\infty(k-1)$ and $C = C = 1/(R\omega_0)$. From this equivalent circuit, it can be found the complex electric permittivity model in the frequency domain as (ENGIN et al., 2019):

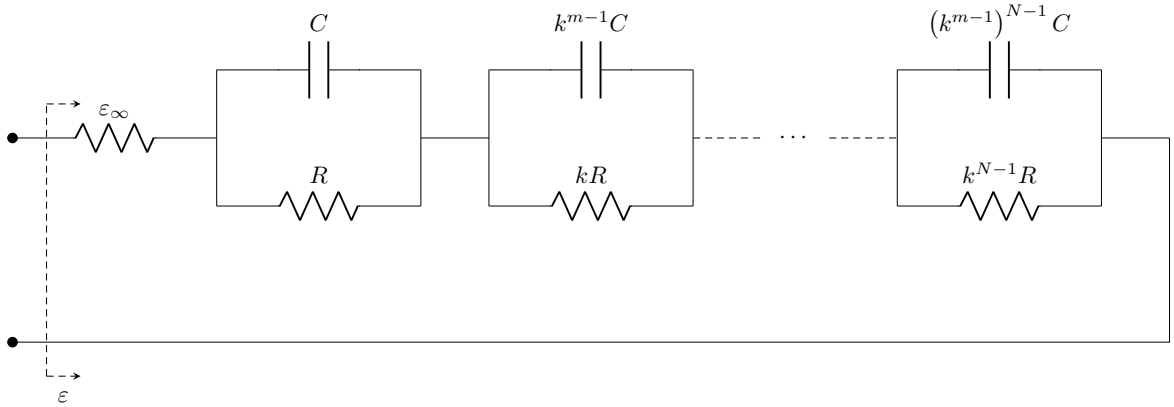

Figure 3.28 – Circuit that represents a lossy dielectric medium according to the multipole Debye model.

$$\varepsilon = \varepsilon_\infty + \sum_{n=0}^{N-1} \frac{\varepsilon_\infty (k-1)k^n}{1 + \frac{j\omega k^{nm}}{\omega_0}}, \tag{3.70}$$

where $m = \pi/2\delta$, $k = 10^{1/m\varsigma}$ is the spacing factor related to the number ς of elements per decade in the Debye model. The parameter ε_∞ is the asymptotic permittivity, that is, the electric permittivity at very high frequencies given by:

$$\varepsilon_\infty = \frac{2\varepsilon_r^{eff}\varepsilon_0}{k^{\frac{N-1}{2}}(k+1)} \tag{3.71}$$

The upper frequency bound ω_0 is related to the bandwidth centre frequency as follows:

$$\omega_0 = \omega_c 10^{\frac{N-1}{2\varsigma}}. \tag{3.72}$$

Therefore, the input parameters used in the implementation of the Debye model in this work are the effective electric permittivity ε_r^{eff} , the substrate loss tangent $\tan\delta$, the angular frequency ω_c in which the substrate is characterized, the number ς of substrate characterization samples, and N that is the Debye model order, that must be chosen in order to increase the accuracy of the model (ENGIN et al., 2019).

3.12 Thin microstrip model validation

In order to validate the thin-wire approximation for thin microstrip structures proposed in this work, three prototypes were built: a printed dipole, an open printed double split ring loop, and the same loop with a lumped inductor in the slit ring gap. The geometry and the dimensions of these Devices Under Test (DUTs) are presented in Figure 3.29. The DUTs were printed over a single-sided copper fibreglass substrate (FR-4) with the geometrical and electromagnetic properties shown in Table 1 (RODA, 2018).

Table 1 – FR-4 geometrical and electrical properties.

Parameter	**Typical value**
Substrate thickness (h_s)	1.48∼1.63 mm
Copper layer thickness (t_c)	0.085 mm
Relative electric permittivity at $1\ MHz$ (ε_r)	4.3∼5.4
Dielectric loss tangent at $1\ MHz$ ($\tan\delta$)	0.027-0.035

These DUTs were experimentally characterized by measuring their reflection coefficient with the calibrated Vector Network Analyser (VNA) Agilent® E5071C. In addition to it, they were simulated by using the frequency domain solver of the simulation suite Computer Simulation Technology (CST®), which is based on the finite element method with adaptive tetrahedral mesh refinement.

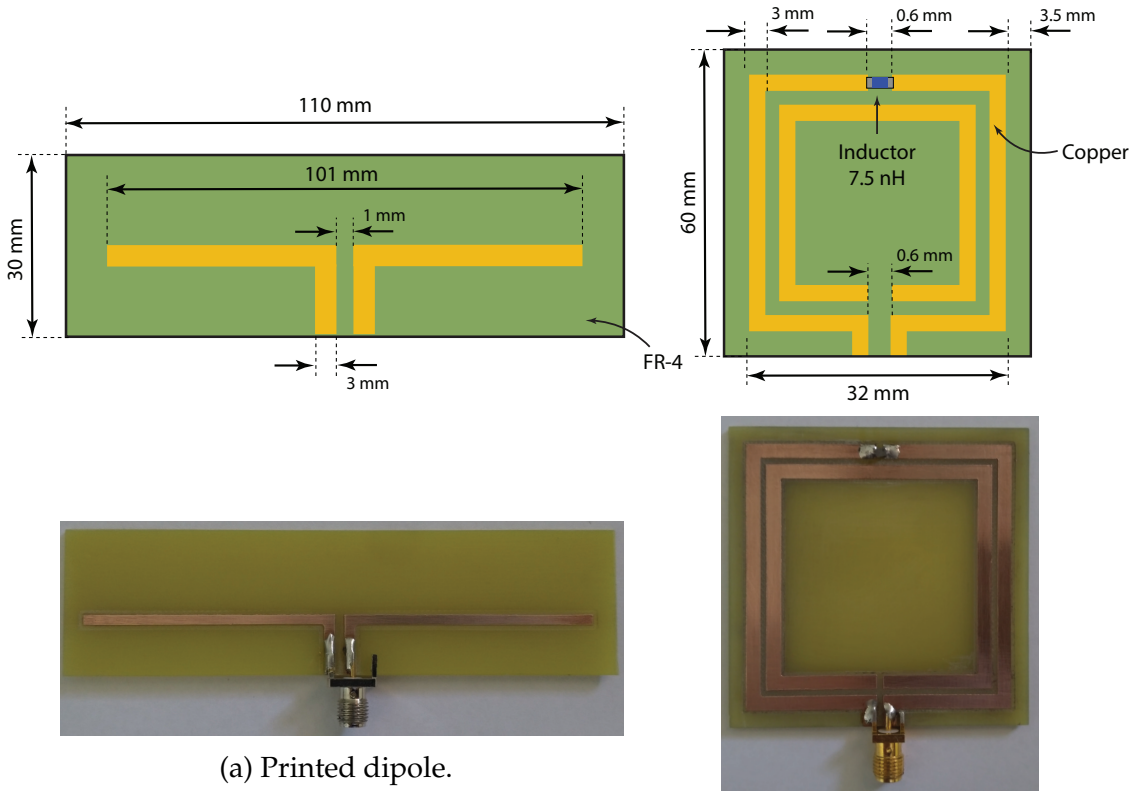

(a) Printed dipole.

(b) Printed double split ring loop with lumped inductor.

Figure 3.29 – Devices under test for the microstrip model validation.

To define the validity range of the proposed model and its implementation, the same error defined in equation 3.66 is used. However, at this point, it is not used to evaluate the accuracy of the model, rather than that it is used to specify the error that must be taken into account when applying this model in a specific application. It is essential to make this distinction since numerically the structure is still a thin-wire with the additional approximations for the conductor cross-section and the dielectric properties.

3.12.1 Printed dipole

The implemented printed dipole, as well as its discretization, are shown in Figure 3.30. For this case, the set of numerical parameters that led to minimum error was the scale factor equal to five, three Gauss points for the observer and two for the source. Regarding the dielectric modelling, the multipole Debye model up to the seventh order was considered. With these settings, it was obtained the reflection coefficient result present in Figure 3.31 along with the simulated and measured results.

As can be noticed, the result calculated with the proposed implementation agrees with the measured result, and the error between them increases linearly with the frequency. This is expected since as the frequency increases, the ratio between the dipole size and the wavelength increases as well, approaching the thin-wire approximation limit.

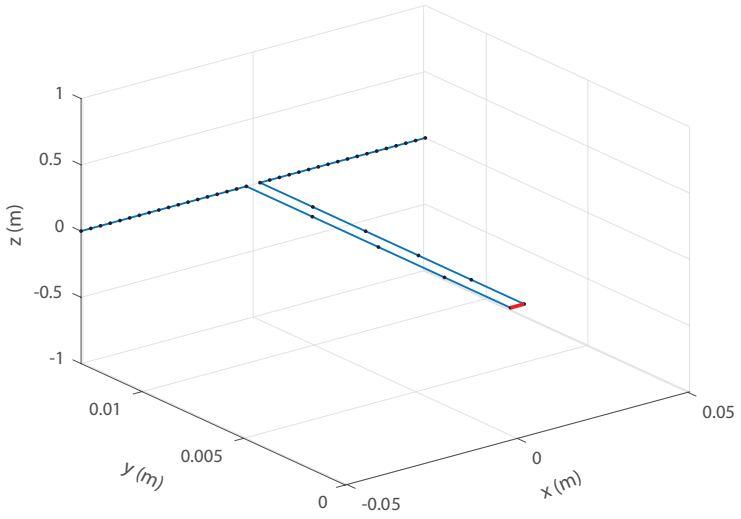

Figure 3.30 – Printed dipole discretization.

Moreover, the dipole was discretized considering the initial frequency of $1\ MHz$, which is also the dielectric specification frequency in Table 1. It also explains the error increasing over the frequency. It must be pointed out that the deviations that can be seen from $200\ MHz$ to $450\ MHz$ are mainly due to constructive uncertainties once after that, the measured reflection coefficient returns to match the calculated curve.

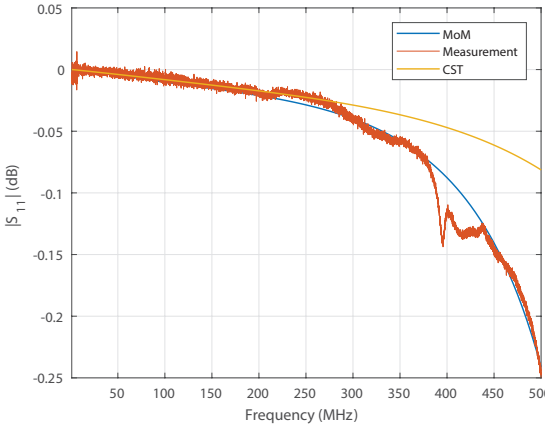

(a) Reflection coefficient S_{11}.

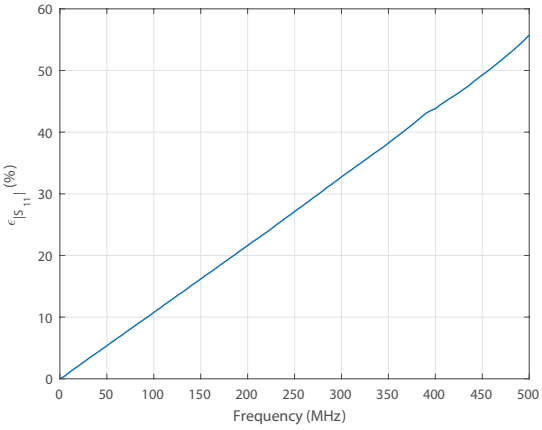

(b) Error between calculated and measured S_{11}.

Figure 3.31 – Results for the printed dipole.

On the other hand, the results obtained through simulation in CST® starts to deviate from the measured and calculated valued after 250 MHz even with its adaptive mesh refinement function set to the start ($1\ MHz$), centre ($250\ MHz$), and the end ($500\ MHz$) of the frequency range. One explanation to this deviation is the fact that, to refine the mesh this software calculated the S-parameter variation from the previous to the actual adaptive pass, if this variation is higher than $0.02\ dB$ the algorithm keeps meshing.

Otherwise, the solver understands that the adaptive refinement converged. As the dipole is not resonant in this range, its reflection coefficient is low, and it achieves the refinement stop after 13 adaptative passes without, in fact, converging. This stop condition can also be changed but the increase in the number of passes leads to an exponential rise in the processing time and memory usage, what makes the simulation of this simple structure prohibitively costly from the computational point of view.

3.12.2 Printed split ring loop

A similar analysis was performed for the printed double split ring loop whose discretization is shown in Figure 3.32a for the open case and 3.32b with the lumped inductor added. As it was observed in the analysis with thin wire structures, the error with lumped elements decreases as the segment size increases. Therefore, the number of segments, in this case, is reduced when compared with the open loop. However, for a scale factor higher than 13, the feeding line cannot be discretized, and the excitation segment is not assigned. Thus, for the following analysis, a scale factor equal to 13 was applied for the case with the lumped inductor, and a scale factor equal to 12 was used for the open loop. For both cases, five Gauss points were used for the observer and six for the source. The calculated, measured, and simulated results are presented in Figure 3.33 and 3.34.

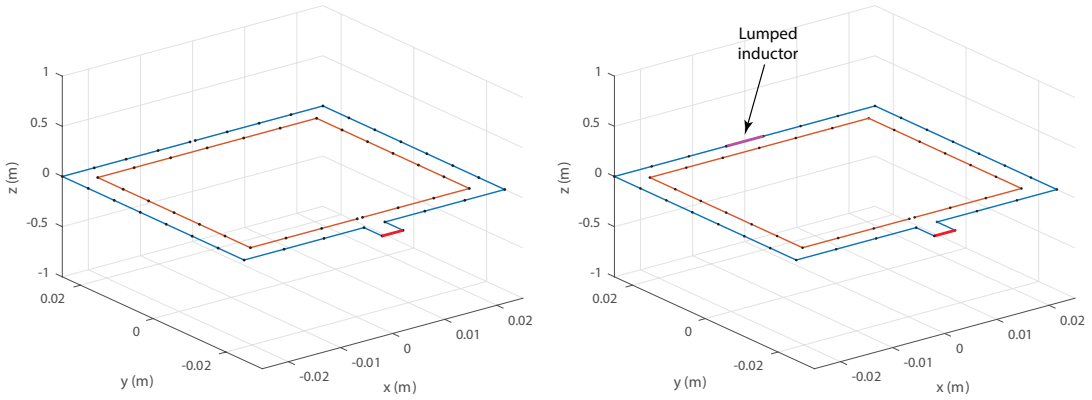

(a) Without a lumped inductor. (b) With a lumped inductor.

Figure 3.32 – Printed split ring loop discretization.

For the open double split ring loop, the calculated and measured results are in close agreement from $1\ MHz$ to $300\ MHz$, after that, the error sharply increases. The reasons for this behaviour are the same pointed out for the printed dipole case, that is, for frequencies above this range the loop perimeter is in the order of the wavelength, and the thin-wire condition is violated. In addition to it, as the dielectric is characterized at $1\ MHz$, the error for its approximation in the proposed model also increases for higher frequencies.

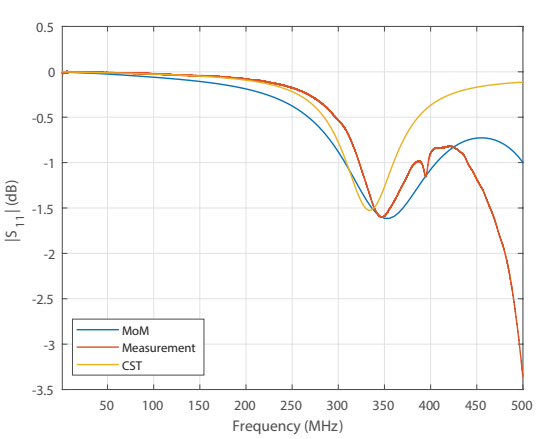

(a) Reflection coefficient S_{11}.

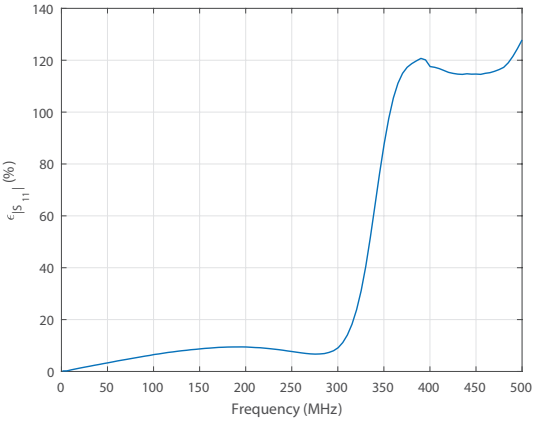

(b) Error between calculated and measured S_{11}.

Figure 3.33 – Results for the printed split ring loop.

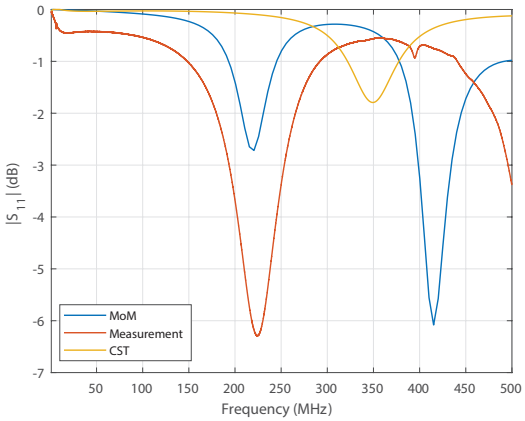

(a) Reflection coefficient S_{11}.

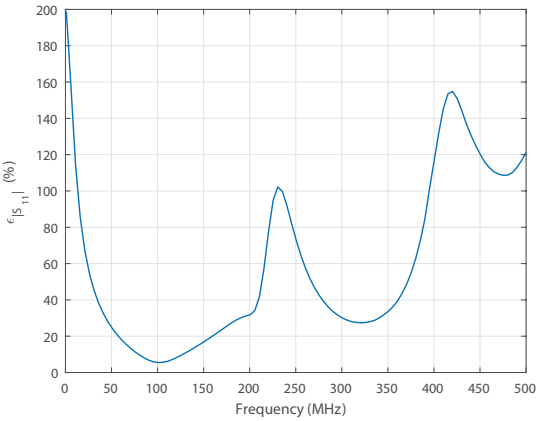

(b) Error between calculated and measured S_{11}.

Figure 3.34 – Results for the printed split ring loop with lumped inductor.

On the other side, the calculated results for the double split ring loop with lumped inductor resemble the measured results, but, in this case an expressive error can be noticed. This error can be justified, in part, for the requirement of larger segment size as indicated in the thin wire loop with a loading coil. As the segment size decreases, the impact of the singularities becomes more and more significant, what reduces the influence of the lumped impedance in the linear system. At the same time, if the segment is too large, the structure cannot be adequately discretized. However, there is another factor that leads to this error: the discretization algorithm prioritizes the thin wire conditions by defining an uniform scale factor in relation to the wire diameter and the wavelength. Thereby, the whole implemented structure is divided into equal segments. When a lumped elements are included, they are treated by the discretization algorithm in the same way that this algorithm treats the excitation, assigning the segment in which

the lumped elements are located as an entire lumped segment that not necessarily corresponds to the physical (packaging) size of this component.

Therefore, in order to reduce the error observed in the numerical evaluation of structures with lumped elements, it is essential to develop a discretization algorithm that accounts for the component packaging size. In this way, the algorithm assigns as many segments as needed to reproduce its dimension or, otherwise, it permits the lumped segment to have a different size from the other segments.

3.13 Partial conclusions

In this chapter, the mathematical modelling of thin microstrip structures is proposed to quantitatively evaluate the behaviour of RWPT resonators and metamaterial structures. This model is based on the integro-differential formulation with thin-wire approximation, and it is numerically implemented through the application of the MoM.

In order to determine the validity of the proposed approach, different case studies were accomplished, and the results were compared with simulated thin-wire antennas and measured thin wire structures. It has been shown that the proposed implementation is capable of accurately describing the behaviour of these structures without lumped elements, and the validity frequency range depends upon the frequency used in the geometry discretization. On the other hand, due to limitations in the discretization algorithm, the calculated results for the cases with lumped elements present some displacement to the measured ones. Therefore, to increase the precision in this case, an adaptive discretization algorithm has to be implemented, and the packaging size of the lumped elements must be taken into account.

Nonetheless, the proposed approach revealed to be an alternative simpler, faster, and computationally cheaper than the tridimensional full-wave simulations performed in a commercial software. Besides, this modelling can be already used for qualitative analysis of metamaterials and RWPT systems, what is aimed at this work. Further improvements in the proposed implementation will also expand its capability to the quantitative analysis and synthesis of RWPT structures and metamaterial devices.

4 Analysis and Design of Metamaterial Lenses

This chapter focus on the analysis and design of metamaterials lenses for RWPT applications. For this intent, the manner in which these lenses overcome the optical diffraction limit is studied as well as the collimation of evanescent magneto-inductive waves by a metamaterial slab with negative magnetic permeability. Then, the Transformation Optics technique is applied in order to qualitatively determine the unit cell arrangements that lead to the converging and the diverging magnetic field collimations. Finally, uniform, converging and diverging metasurface lenses are designed and prototyped based on the analysis realized in this chapter. The behaviour of a uniform metamaterial lens is qualitatively analysed with the numerical implementation proposed in this work.

4.1 Metamaterial lenses applied to RWPT systems

As discussed in chapter 2, a way to improve the efficiency of RWPT systems is through the inclusion of a resonant slab which acts by manipulating the effective magnetic permeability on transmission stage. The operation principle that leads to this enhancement has been previously analysed, but its physical realisation has not been discussed so far. From these analyses, it can be concluded that the magnetic field generated by the transmitter coil induces an electric current in the resonator slab, thus creating a magnetic dipole moment. Moreover, the physical dimension of this resonator is much smaller than the wavelength at its resonant frequency. Therefore, each part of the resonator slab emulates the atomic resonances; in this sense, they can be called "meta-atoms". Based on this analogy, the whole slab, that is, the material constituted by these meta-atoms can be defined as a **metamaterial**.

Although a closed definition has not been agreed so far, it can be affirmed that metamaterials are composite materials, with a periodic or non-periodic structure whose unusual electromagnetic behaviour emerges from their unit cell arrangement and chemical composition (CUI; LIU; SMITH, 2010). It is essential to notice that the intrinsic electromagnetic properties of the medium in which the metamaterial is designed remain unchanged. However, it is the topology and geometrical disposition of the unit cell that lead to the effective electromagnetic parameters that characterise the metamaterial (ALMEIDA; FEITOZA, 2018).

The metamaterial concept was conceived by Victor Veselago (VESELAGO, 1968), who investigated the electrodynamic behaviour of left-handed media, i.e. a medium with negative magnetic permeability and electric permittivity. However, it was only after

the realisation of negative permittivity by using a wire medium (PENDRY et al., 1996), and negative permeability with Split Ring Resonators (SRR) (PENDRY et al., 1999) that this concept called out the attention of the scientific community. Nowadays, metamaterials have been used in invisibility cloak (STECKIEWICZ; CHOROSZUCHO, 2019), frequency selective surfaces (VERMA et al., 2020), electromagnetic band-gap structures (BRANDAO et al., 2020), leaky-wave antennas (CHOWDHURY; PAL; GHATAK, 2018), and superlenses (HARRIS; STANCIL; RICKETTS, 2019), among other applications.

The concept of superlenses, that is, lenses made of left-handed media (artificial media that presents simultaneously negative electric permittivity and negative magnetic permeability) that are able to overcome the diffraction limitation, was proposed in (PENDRY, 2000). This limit can be understood as follows: considering a lens which is located in the z-axis illuminated by an electric field source that propagates in the $+\hat{z}$ direction. This field can be described by the superposition of its spectral components:

$$E(\mathbf{r},t) = \sum_{k_x,k_y} E_0(k_x,k_y)e^{j(k_x x+k_y y+k_z z-\omega t)}, \tag{4.1}$$

being the wave vector component in the direction $\hat{z}$ related to the components in the other directions according to:

$$k_z = \sqrt{\frac{\omega^2}{c^2} - (k_x^2 + k_y^2)}. \tag{4.2}$$

The lens acts in this field by performing a phase correction in each spectral component in a way that, at its focal point, the field is reassembled and an image of the field source is generated (PENDRY, 2000). However, if the wave vector components are such that $k_x^2 + k_y^2 > \frac{\omega^2}{c^2}$, the equation 4.2 will be purely imaginary, characterizing an evanescent field. In this case, the field attenuation will not allow the formation of the source image at the focus. Therefore, the ability of a lens to collimate fields is limited by $k_x^2 + k_y^2 < \frac{\omega^2}{c^2}$. From this limit, the maximum resolution Δ_{max} of any lens is given by:

$$k_{max} = \frac{2\pi}{\Delta_{max}} = \frac{\omega}{c} \;\Rightarrow\; \Delta_{max} = \lambda. \tag{4.3}$$

In other words, the smaller area that a lens can collimate fields is λ^2.

Unusual behaviour is observed when the lens is composed of an artificial left-hand medium with $\varepsilon = -1$ and $\mu = -1$. First, it must be pointed out that, in this medium, the refractive index $n_0 = -\sqrt{\mu_0\varepsilon_0}$ since, for this case, the negative square root must be considered, as demonstrated in (ZIOLKOWSKI; HEYMAN, 2001). Moreover, the intrinsic impedance for a left-hand medium is equal to the one in free-space, so the lens is perfectly matched to free-space, and there is no reflection as the field components penetrate or leave the lens. In this medium, the transmission coefficient T is given by:

$$T = e^{-jdk_z}, \tag{4.4}$$

where d is the thickness of the metamaterial slab. Therefore, there is a phase reversal in the left-hand metamaterial that cancels the phase acquired by the wave as it propagates. In addition to it, the metamaterial amplifies the evanescent field amplitude, as it is shown in Figure 4.1. Thus, the metamaterial is able to focus even the evanescent fields, reconstructing both propagating and evanescent waves (PENDRY, 2000). For this reason, these devices are called **superlenses** or perfect lenses.

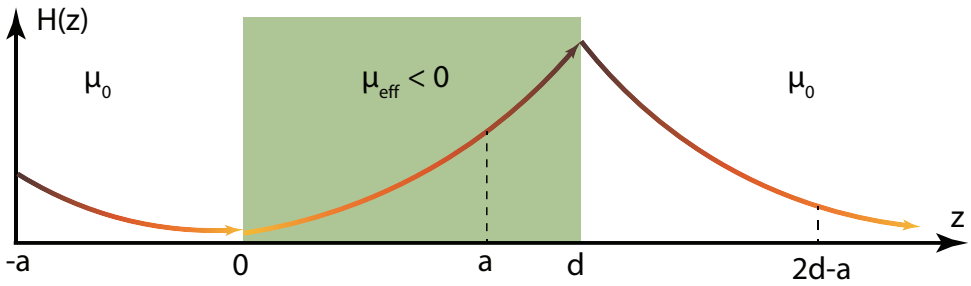

Figure 4.1 – Evanescent magnetostatic field amplification in a metamaterial lens.

Particularly for the case of RWPT systems, the evanescent fields are magnetic in its nature, and the separation between the unit cells is much smaller than the wavelength. In this magneto-quasistatic situation the double negative requirement can be relaxed and only $\mu = -1$ is required in order to design a superlens (SOLYMAR; SHAMONINA, 2009). In addition to the evanescent magnetic field amplification, the resonance of the magnetostatic wave reinforces it in a way that, for a theoretical lossless metamaterial lens, the field amplification would be infinite (HARRIS; STANCIL; RICKETTS, 2019). It is essential to point out that it does not violate the principle of energy conservation because the evanescent waves do not transport energy and, thus, there is no change in power (PENDRY, 2000).

However, as it is represented in Figure 2.9 and was previously discussed in section 2.4 that the imaginary part of the effective magnetic permeability sharply increases while the real part becomes negative. Nonetheless, this imaginary part is associated with the losses in the metamaterial slab, thus, the higher losses are verified around the metamaterial resonant frequency. Therefore, even though the maximum field amplification is achieved when the perfect lens condition $\mu = 1$ is satisfied, this is the condition in which the losses are higher, reducing then the RWPT efficiency. Consequently, as demonstrated in (HARRIS; STANCIL; RICKETTS, 2019), a non-perfect metamaterial lens, that is, with $\mu < 0,\ \mu \neq -1$ is better suitable for RWPT efficiency enhancement.

4.2 Metamaterial homogenization in RWPT systems

From the electromagnetic point of view, a metamaterial is described by its effective electric permittivity and magnetic permeability. Thus, it is convenient to extract these

properties in order to approximate the whole material as a homogeneous medium with these effective properties (SMITH; PENDRY, 2015). It is accomplished by the so-called homogenization methods, that apply different formulations to approximate and extract the metamaterial properties.

As discussed in section 2.4, a metamaterial slab enhances the RWPT efficiency by changing the effective magnetic permeability μ_{eff} of the system. Thereby, for RWPT systems, the permeability can be retrieved by measuring the scattering parameters (S-parameters) matrix over the frequency, as proposed in (CHEN et al., 2012). The measurement setup is constituted by two coaxially aligned coils, both with area A, as shown in Figure 4.2.

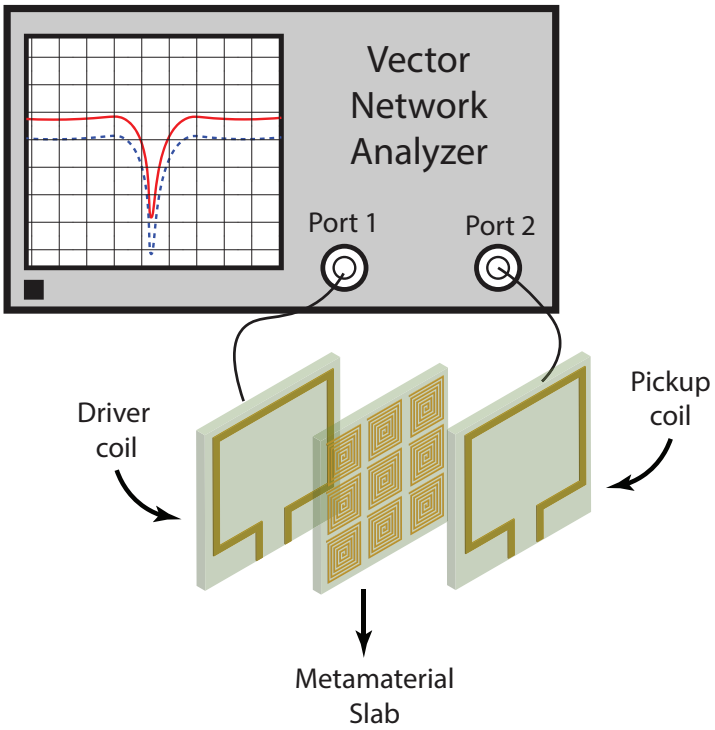

Figure 4.2 – Measurement setup for effective magnetic permeability retrieval in RWPT systems.

From the Faraday's Law, the electromotive force $V(t)$ induced in the pickup coil due to magnetic field $H(t)$ created by the drive coil is given by:

$$V_r(t) = \left| A\mu_0 \frac{\mathrm{d}H(t)}{\mathrm{d}t} \right|. \tag{4.5}$$

Then, when a metamaterial slab also with area A is inserted between the coils, the induced electromotive force is:

$$V_s(t) = \left| A\mu_{eff}\mu_0 \frac{\mathrm{d}H(t)}{\mathrm{d}t} \right|. \tag{4.6}$$

In equations 4.5 and 4.6 the index r indicates the reference measurement without the metamaterial slab, and s indicates the measurement with the metamaterial sample.

Thus, the effective magnetic permeability over the frequency ω can be calculated as (CHEN et al., 2012):

$$\mu_{eff}(\omega) = \frac{\mathfrak{F}\left[V_s(t)\right]}{\mathfrak{F}\left[V_r(t)\right]}, \tag{4.7}$$

where $\mathfrak{F}$ denotes the complex Fourier transform of the measured induced electromotive force.

These measurements can be performed in two ways. Firstly, as proposed in (CHEN et al., 2012), a pulse is applied in the driver coil, and the induced voltage is measured at the pickup with an oscilloscope. For the second approach, presented in (WU et al., 2015) and used in this work, the drive coil is connected to the Port 1 of a VNA whereas the pickup coil is connected to Port 2. Thereby, as the input power is unchanged and the forward complex transmission coefficient S_{21} is proportional to the ratio between the output and input electromotive force, the effective permeability is given by:

$$\mu_{eff}(\omega) = \frac{V_s(\omega)}{V_r(\omega)} = \frac{\Re(S_{21}^s) + j\Im(S_{21}^s)}{\Re(S_{21}^r) + j\Im(S_{21}^r)}, \tag{4.8}$$

where $\Re(S_{21}^s)$ and $\Im(S_{21}^s)$ are, respectively, the real and imaginary parts of the forward complex transmission coefficient. More details about the physical implementation of this measurement technique are presented in chapter 5.

4.3 Transformation Optics

The manner in which metamaterial lenses alter the field path inside and outside them is related to their inhomogeneous and anisotropic electromagnetic properties. Therefore, it is possible to design a material in order to get a specific field path. It can be accomplished by using a technique called **Transformation Optics** (TO) which has been extensively used in order to design novel metamaterial devices (YU et al., 2009). In this technique, the field path manipulation is expressed as a coordinate system transformation. Once Maxwell's equations are invariant to this transformation, the electric permittivity ε^* and magnetic permeability μ^* tensors in this new coordinate system is related to the homogeneous properties (ε, μ) in Cartesian coordinates through Eq. 4.9 and Eq. 4.10, where $\mathbb{J}$ is the Jacobian matrix operator (ABDOLALI; SEDEH; FAKHERI, 2020).

$$\varepsilon^* = \frac{\mathbb{J}\varepsilon\mathbb{J}^T}{\det(\mathbb{J})}, \tag{4.9}$$

$$\mu^* = \frac{\mathbb{J}\mu_s\mathbb{J}^T}{\det(\mathbb{J})}. \tag{4.10}$$

In this work, TO is used to find out the unit cell arrangements that lead to convergent and divergent lenses. This technique reveals the refractive index profile in the device

required to alter the field path as desired. Once each unit cell has a different refractive index, they can be positioned in order to reproduce this profile (ESKANDARI; TYC, 2019).

A coordinate system transformation that represents the electromagnetic behaviour of plane converging and diverging lenses is developed in (GILOAN, 2017). This new system (x', y') in the $xy-$plane can be expressed as a function of the Cartesian coordinates (x, y):

$$\begin{cases} x' = x \\ y' = \dfrac{1}{\delta - \gamma\sqrt{\varphi^2 + y^2}} \end{cases}, \tag{4.11}$$

where $\gamma = \pm\frac{1}{h_s}$, h_s is the metamaterial lens thickness, φ is the focal point location and $\delta = 1 + \varphi\gamma$. In order to design converging lenses, the positive sign $+\gamma$ must be chosen whereas, for diverging lenses, the negative sign $-\gamma$ is more appropriate.

The effect of this coordinate system transformation is represented in Figure 4.4(a) for converging lenses and in Figure 4.4(b) for diverging lenses. In these graphs, the field path expected after a uniform magnetic field crosses the metamaterial lens is represented. Even though these graphs do not provide information about the field magnitude, they describe how the metasurface act on this field by "distorting" the coordinate system to focus the magnetic field in a specific direction: at the centre for the converging lens, and at the border for the diverging lens.

When the TO technique is applied, it returns the required electric permittivity and magnetic permeability of a medium that is able to perform this "distortion" on the path of a plane wave normally incident upon the lens. Considering this transformation and a homogeneous and isotropic substrate, the permittivity and permeability in the transformed coordinate system are given by Eq. 4.9 and Eq. 4.10. Therefore, the lens refractive index can be calculated through $n^* = \sqrt{\mu^*\varepsilon^*}$. To analyse the refractive index results, consider a cross section $a - a'$ of the metamaterial lens, as indicated in Figure 4.3.

The refractive index distribution at each point of the metamaterial cross-section is indicated in Figure 4.4(c) for a converging lens and in Figure 4.4(d) for a diverging lens. From these results, it can be affirmed that, in order to design a converging lens, the metamaterial unit cells must be positioned in a way that those with higher refractive index are in the border, with refractive index decreasing towards the centre. On the other hand, for a diverging lens, the unit cell refractive index must decrease towards the edge.

It is important to notice that, even though the TO technique can be used to calculate the electric permittivity and magnetic permeability tensors and the metamaterial can be

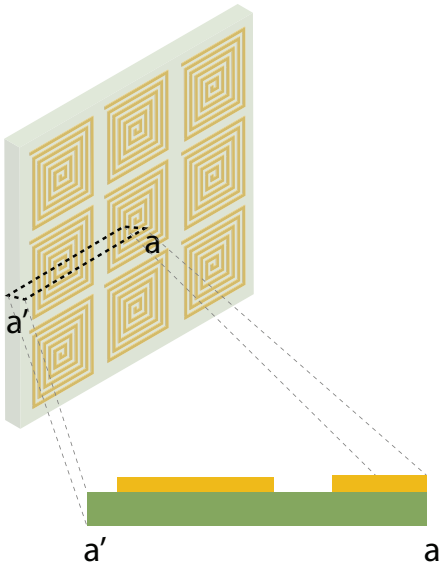

Figure 4.3 – Metamaterial lens cross-section $a - a'$.

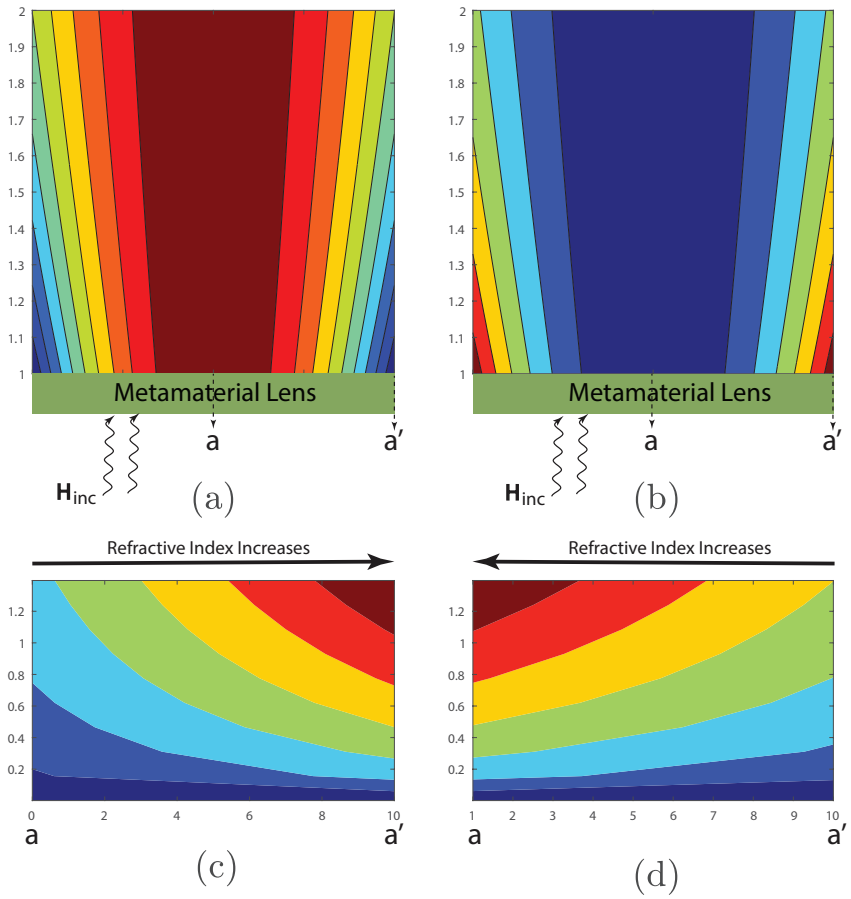

Figure 4.4 – Transformation optics applied to metamaterial lenses: (a) converging lens, (b) diverging lens, (c) refractive index profile for converging lens behaviour, and (d) refractive index profile for diverging lens behaviour.

designed to achieve these parameters, in this work, TO is applied qualitatively in order to provide the required direction of the refractive index gradient in each lens topology (SMITH et al., 2005).

4.4 Design of magnetic metasurface lenses

The first step to project a metasurface is to design a unit cell in which induced currents emulate atomic resonances. To achieve this operation, it is required that the unit cell size shall be less than a tenth of the free-space wavelength. Nevertheless, in this work, subwavelength unit cells (size $\ll \lambda_0$) are designed.

Two major design constraints for the unit cell design are established. First, the unit cell size is limited to $4\ mm$ to assure the unit cell periodicity without having very large full structures. This is important since the losses in the dielectric substrate as well in its conductive layer increase with its size. In addition to it, the entire system, that is, the RWPT resonator and the metamaterial slabs must operate at $28\ MHz$. This specific frequency was chosen because it allows having subwavelength cells without leading to a constructively prohibitive size. Also, this frequency is in the validity range of the developed numerical implementation. Among other factors, it can also be noticed that this frequency is located in the 10m band, which is internationally allocated to amateur radio. Therefore, it is an easy licensing and access band, with low-cost options for transmitters, electronic components, and instrumentation, and it is also very close to an ISM band ($26.957 - 27.283\ MHz$) which would facilitate the adaptation for commercial applications. Based on these constraints, it is assured that the subwavelength condition is satisfied since the unit cell size is $\lambda_0/250$.

One of the most commonly used unit cell topologies is the Split Ring Resonator (SRR). However, to operate at the specified frequency, this topology itself would be prohibitively large. Therefore, a lumped capacitor is added in the SRR gap to get a more compact structure (WANG et al., 2011). Consequently, the resonant frequency and the metamaterial parameters can be adjusted by varying the SRR dimensions and the lumped capacitance C. The proposed square SRR topology is presented in Figure 4.5a.

The metamaterial unit cell and the full structure were designed and optimized using the software Computer Simulation Technology (CST®) to get $\mu < 0$ in $28\ MHz$. The optimization method applied is the Covariance Matrix Adaptation Evolutionary Strategy (CMA-ES), with the sigma parameter equal to 0.9 to force the method to be more global. In the simulation and optimization of metamaterials, the excitation and boundaries must be judiciously chosen according to the application properties. For the present case, the designed structures were centred between two parallel waveguide ports; perfect electrically conducting boundary conditions were set on the faces that are perpendicular

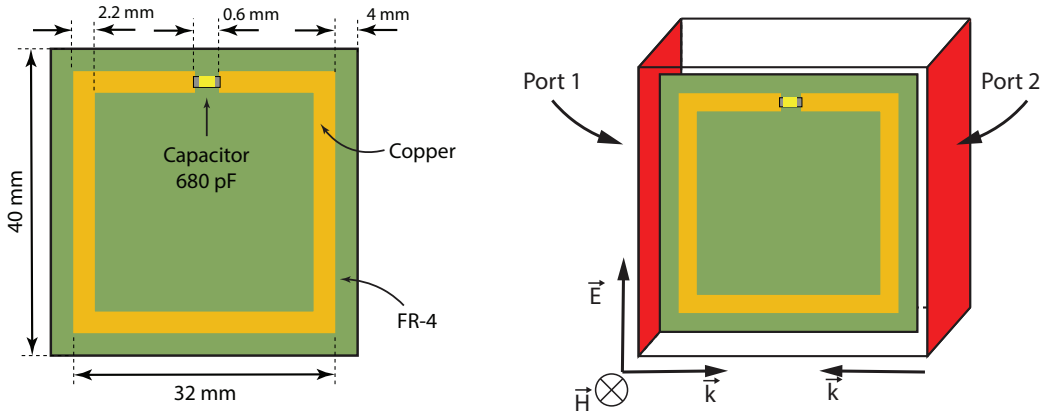

(a) Topology and optimized dimensions.

(b) Ports and boundary assignment.

Figure 4.5 – Metamaterial lens unit cell.

to the electric field $\vec{E}$ and perfect magnetically conducting boundary conditions on the faces that are perpendicular to the magnetic field $\vec{H}$ (BAKIR et al., 2017), as indicated in Figure 4.5b, in which $\vec{k}$ is the wave vector. Therefore, it is guaranteed that the magnetic field is normally incident upon the metamaterial lens, and this configuration enables the metamaterial parameter extraction function in CST®.

Based on this unit cell, a full-structure constituted by a 5x5 unit cell arrangement, as shown in Figure 4.6a, was simulated. However, due to the inductive and capacitive couplings between unit cells, the metamaterial resonant frequency is shifted and the whole structure must be retuned. After that, the dimensions presented in Figure 4.5 are obtained. This designed metamaterial was built on a single-side FR-4 substrate through an etching process; this prototype can be seen in Figure 4.6b.

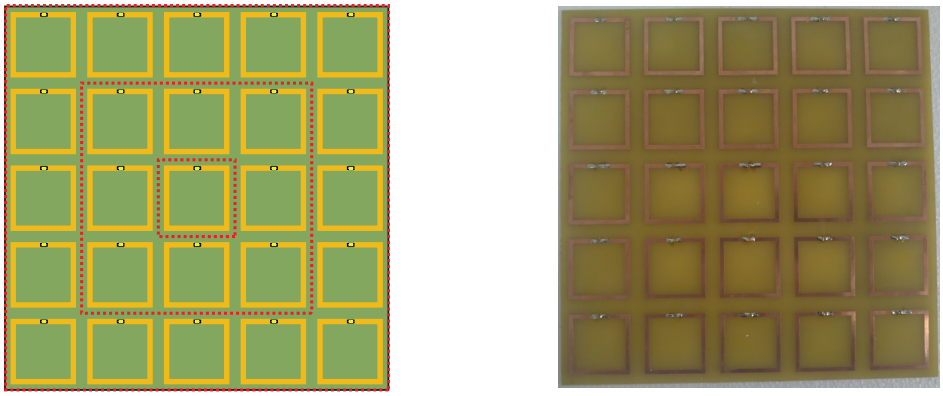

(a) Topology

(b) Prototype

Figure 4.6 – Designed metamaterial lens.

In this case, the refractive index gradient provided by the TO technique can be reproduced in two ways: by changing the unit cell size or by varying the value of the capacitor added to it. The advantage of the first approach is that it assures that all unit cells resonate in the same frequency (SOARES; RESENDE; SIQUEIRA, 2018); however,

it is constructively more complex. On the other hand, fixing the unit cell geometry and changing only the capacitance value favours the full structure discretization and its numerical analysis by the proposed approach. For this reason, in this work, three different capacitor values are used; one at each layer indicated by the red dashed line in Figure 4.6a.

The graph in Figure 4.7 presents the parametric analysis result of the refractive index as a function of the lumped capacitance as blue dots that were interpolated by the red line. As it can be seen, the refractive index reduces as the capacitance increases. Therefore, based on the available commercial values for capacitors, the converging and diverging metasurface lenses were built, as shown in Figure 4.8a and 4.8b, respectively. In addition to, for the sake of comparison, an uniform metamaterial lens in which all unit cells were loaded with $680\ pF$ capacitor was prototyped.

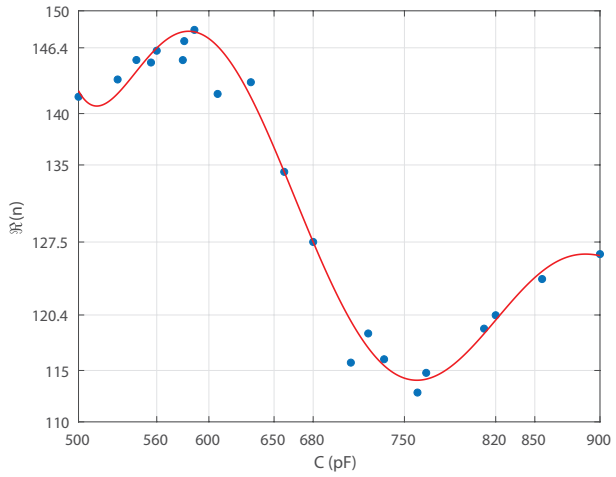

Figure 4.7 – Real part of the refractive index as a function of the lumped capacitance.

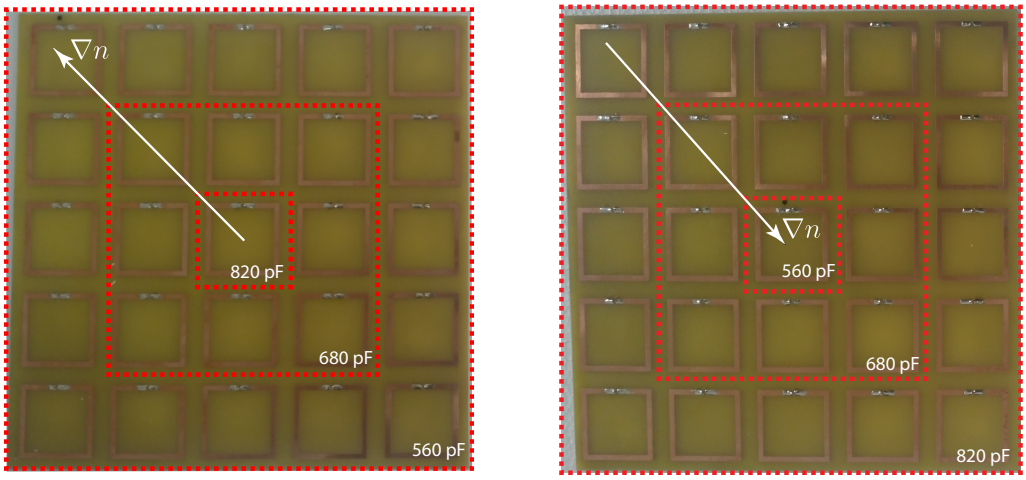

(a) Converging lens. (b) Diverging lens.

Figure 4.8 – Prototypes of the designed metamaterial lenses.

4.5 Simulation of metamaterials through the Method of Moments

As discussed in section 3.13, the electromagnetic formulation proposed in this work for thin wire microstrip structures and its numerical solution through the Method of Moments opens up a possibility to conduct simulations and qualitative analyses of metamaterials and RWPT devices. Therefore, the uniform lens described in the previous section is computationally implemented in the developed code, whose results were presented in chapter 3.

For this simulation, a loop with the same size as the metamaterial lens is used in order to generate the magnetic field that shall be collimated by the lens. In Figure 4.9, it is shown the magnetic field distribution only with this loop. Then, in Figure 4.10 it is possible to see the field collimation when the uniform lens is inserted in front of the loop.

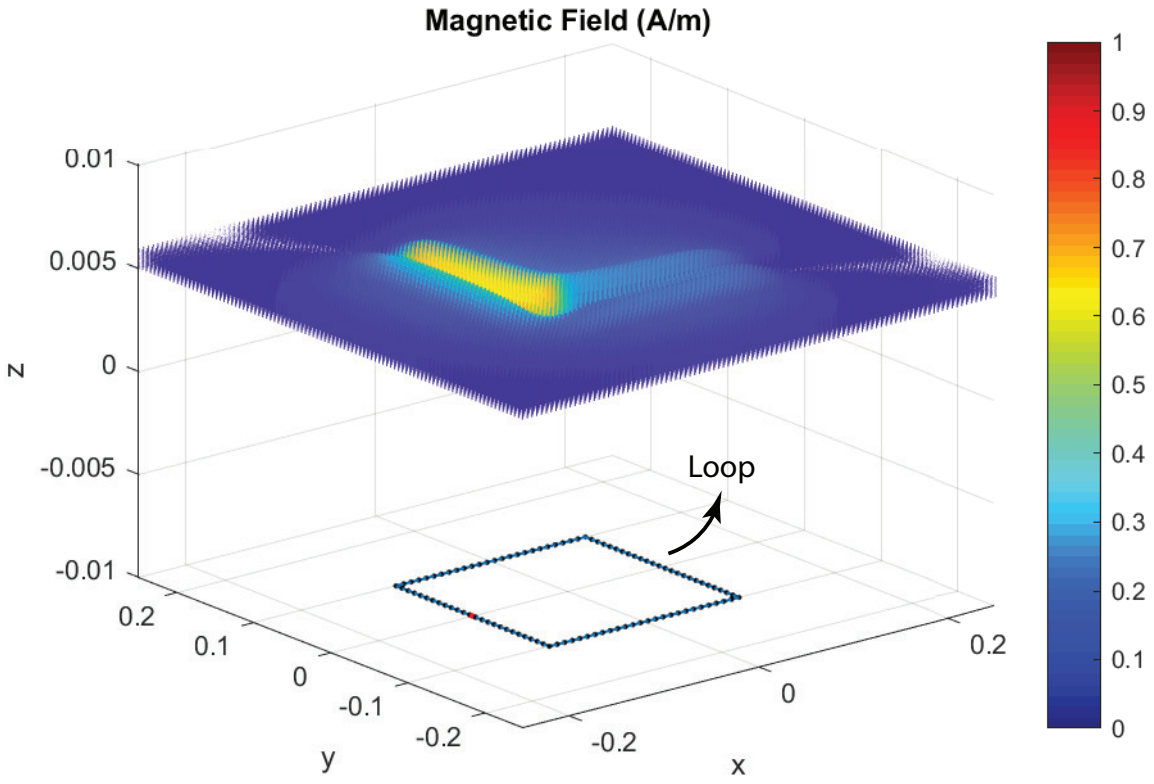

Figure 4.9 – Distribution of the magnetic field generated by the loop.

This simulation was carried out also for the designed converging and diverging lenses, however, the obtained results were very close to the one presented in Figure 4.10. It is due to the fact that the numerical implementation proposed in this work cannot properly deal with the capacitance variation between unit cells. The algorithm developed is not

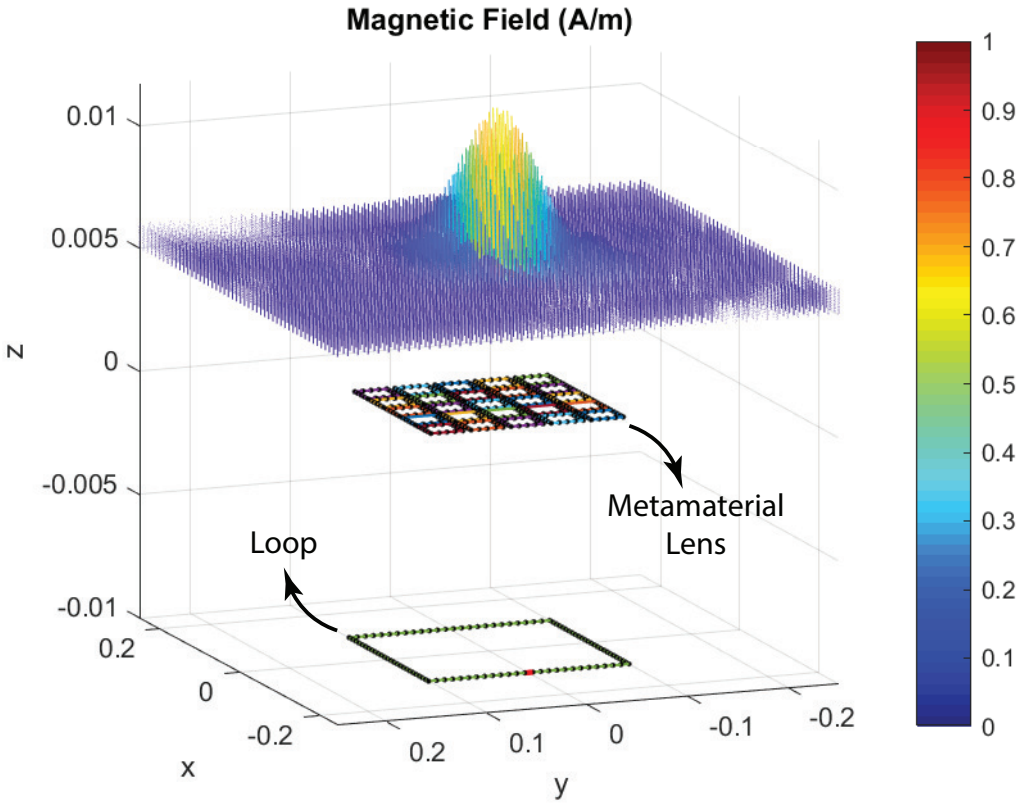

Figure 4.10 – Collimation of the magnetic field by the metamaterial lens.

able to refine the discretization to accurately represent the small features of the full system, since as discussed in subsection 3.12.2, when the segment size is too short, the influence of the integral singularities is expressive and shadows the effect of such small lumped capacitance variation. However, with the improvements proposed in chapter 3, it will be possible to achieve more precise results.

Nonetheless, the result obtained for the uniform lens proves that the proposed formulation can be used for the analysis of a metamaterial lens. It should be pointed out that it is an approximation for the physical problem and it is intended to be a qualitative analysis but, nevertheless, it turns out to be an useful tool and a starting point for metamaterial design and fast verification of its behaviour.

4.6 Partial conclusions

In this chapter, the metamaterial lens operation principle is discussed as well as how these structures enhance the efficiency of RWPT systems. First, metasurfaces lenses are able to overcome the diffraction limit by amplifying the magnetostatic evanescent fields and, particularly in RWPT applications, the magnetic resonance leads to an intensification of this effect, that is limited only by the metamaterial losses. Thereby,

to properly apply these superlenses for wireless power transfer, the effective magnetic permeability must be $\mu < 0$, but with $\mu \neq -1$. Then, the efficiency enhancement can be achieved, and the losses in the lens minimised.

Thus, a manner to design magnetic metasurface lenses with controlled field collimation is proposed through the application of the Transformation Optics technique. This technique reveals that the collimation profile is related to the refractive index gradient in the lens, in a way that converging lenses have unit cells with the higher refractive index at the border, whereas for diverging lenses, it is located at the centre. In addition to it, a procedure of effective magnetic permeability retrieval in an RWPT system is discussed. Finally, the design and physical realisation of uniform, converging, and diverging magnetic metasurface lenses are presented. It is also shown that, with the proposed numerical implementation, it is possible to verify the effect of an uniform metamaterial lens collimating a magnetic field generated by the electric current that flows in a loop.

5 Experimental Analysis of RWPT Systems with Metamaterial Lenses

In this chapter, two RWPT systems based on the two-coil and four-coil topologies are designed and prototyped. Then, these systems are used to perform experiments related to the topics discussed in this work. Thereby, the maximum and realised RWPT efficiencies are analysed, the frequency splitting phenomenon is evaluated as well as a way of mitigating its effects on the efficiency, and the power transfer levels are measured with the inclusion of rectifier circuits at the system output. Moreover, the metamaterial lenses are characterised, and their enhancement in RWPT systems is verified.

5.1 Design of the RWPT systems

In this work, two RWPT systems are designed based on the two and four-coil systems analysed in chapter 2. For both systems, the square topology is chosen, since it leads to higher coil quality factors (MAO et al., 2018). First, the dimensions of each resonator are optimised using CMA-ES algorithm in CST® with the same settings described in section 4.4. The goal specified for this optimisation is to minimise the VSWR at $28\ MHz$, and it was established according to the transmitter operation requirements. Moreover, in order to get a compact structure, the resonators are designed in an FR-4 board with the same size of the designed metamaterial lenses, that is, $200 \times 200\ mm$. In the case of the four-coil RWPT resonator, it is used a double-sided FR-4 board in a way that the driver/sink coil is placed in one copper layer and the transmitting/receiving resonator is in the opposite layer. The designed coils with their optimised dimensions are presented in Figures 5.1 and 5.2 as well as the built prototypes in Figure 5.3.

In order to complete the resonator design, the inductive reactance of each coil must be compensated. Therefore, for the two-coil RWPT resonator, a capacitor is connected in series with the loop and its value is optimised, leading to $47\ pF$, as indicated in Figure 5.1. However, in the prototype, a variable capacitor (trimmer) with measured capacitance range from $30 - 60\ pF$ is used for a fine adjustment. On the other hand, the four-coil RWPT resonator was optimised in a way that its self-capacitance compensates its inductive reactance at the operation frequency.

The reflection coefficient of the prototypes was measured with the vector network analyser nanoVNA, and the measured results are presented in Figure 5.4 as well as the simulated results. As it can be seen, the two-coil RWPT resonator cannot achieve the desired VSWR due to its structure. A resonant loop at $28\ MHz$ would be too large, and

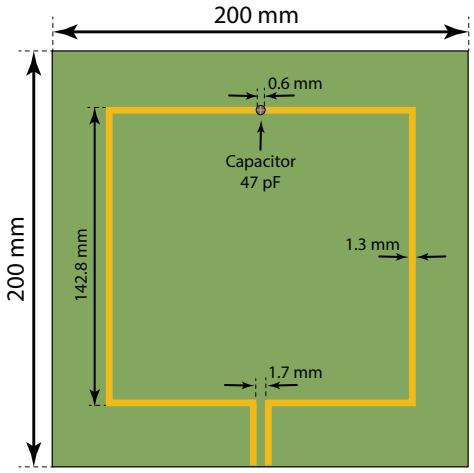

Figure 5.1 – Optimized dimensions for a two-coil RWPT resonator.

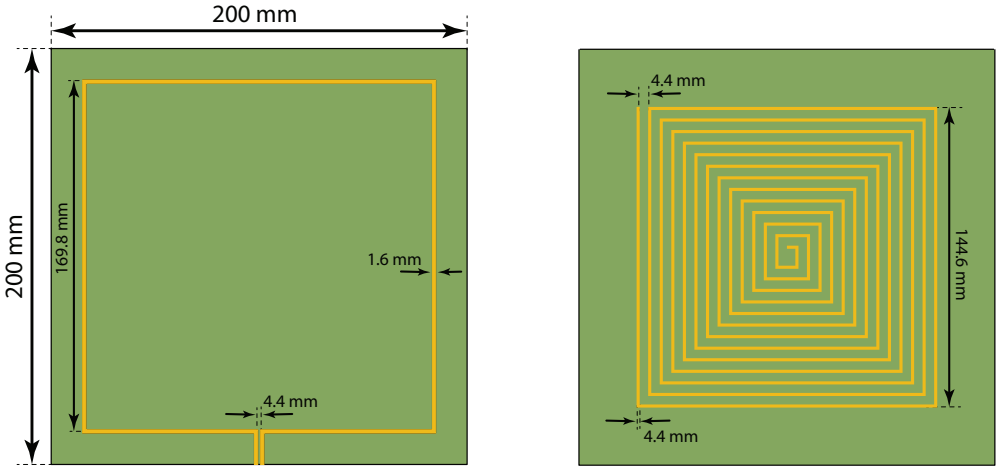

(a) Driver/Sink coil.

(b) Transmitting / Receiving resonator.

Figure 5.2 – Optimized dimensions for a four-coil RWPT resonator.

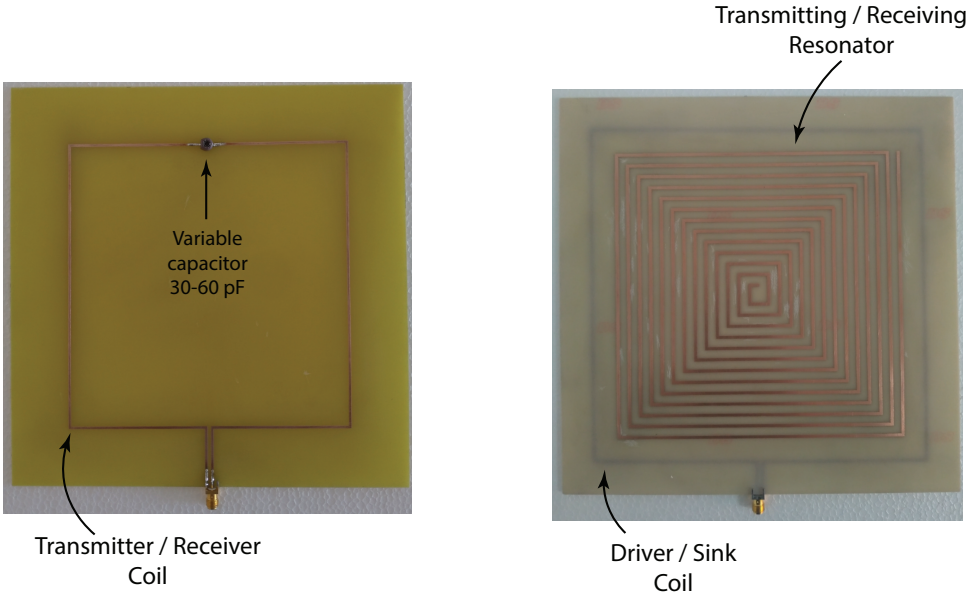

(a) Two-coil system resonator.

(b) Four-coil system resonator.

Figure 5.3 – Prototypes of the designed RWPT resonators.

a spiral topology would require feeding through vias or wires, which are avoided in this work. It can also be seen that there is a significant deviation from the measured and simulation results; this is due to the variable capacitor that was tuned to minimise the reflection coefficient in the built prototype. In contrast to that, the S_{11} measurements on the four-coil RWPT prototype corroborate with the simulated results, and it satisfies the design requirement with a measured VSWR equal to 3.57.

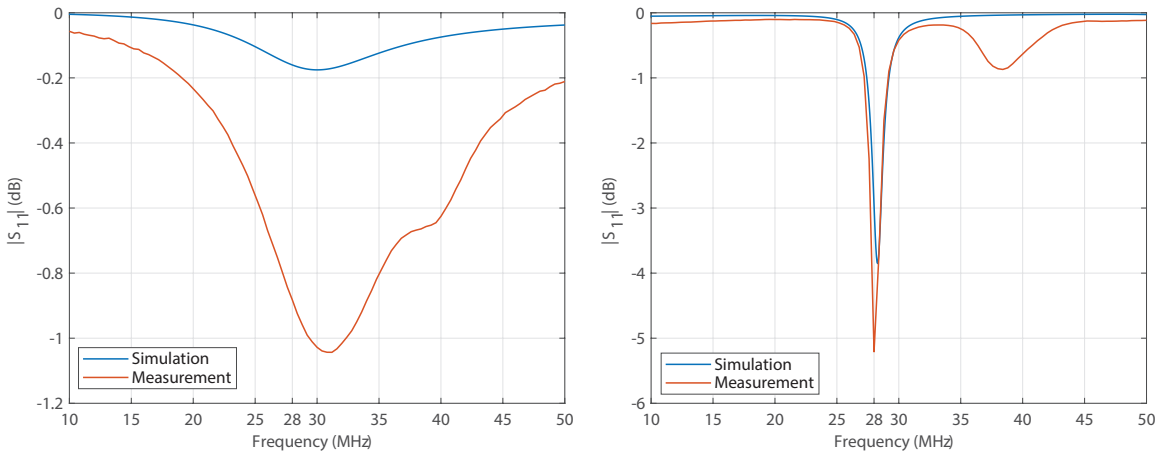

(a) Two-coil system.

(b) Four-coil system.

Figure 5.4 – Simulated and measured reflection coefficient for the designed resonators.

5.2 Measurement setup description

To analyse and compare the behaviour of both designed RWPT systems, the measurement setup schematised in Figure 5.5 is proposed. As shown in Figure 5.6a, the transmitter coil is connected to the Port 1 and the receiver to the Port 2 of the nanoVNA, that is connected to a computer. Then, through the nanoVNA interface installed on the computer, the scattering-parameter matrix is measured in a frequency range from $10\ MHz$ to $50\ MHz$, and this result is saved as a touchstone file (*.s2p*). This measurement is performed by varying the distance between transmitter and receiver coils from $10\ cm$ to $60\ cm$ in $10\ cm$ steps. It is important to highlight that, prior to the measurements, the nanoVNA was calibrated at the cable extremities using the Short-Open-Load-Thru (SOLT) standard.

After the measurements with only the two-coil and four-coils systems, the metamaterial lenses were positioned $5\ cm$ apart from the transmitter coil, as shown in Figure 5.6b. Then, the same measurements were performed considering the uniform, converging and diverging lenses.

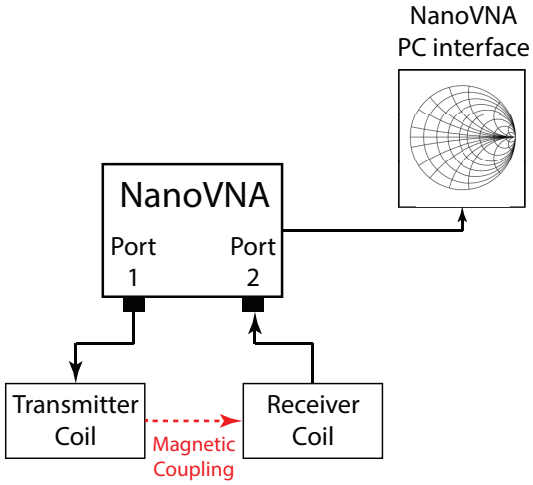

Figure 5.5 – Block diagram for the efficiency measurement.

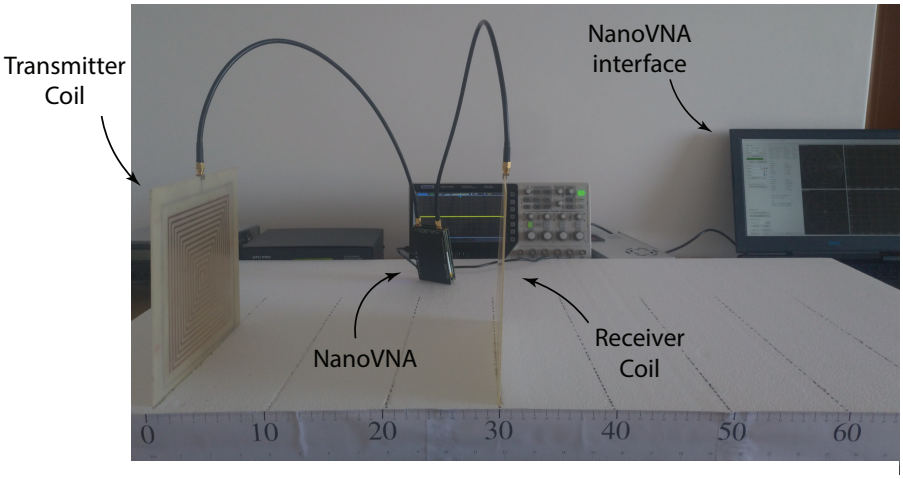

(a) Without metamaterial lens.

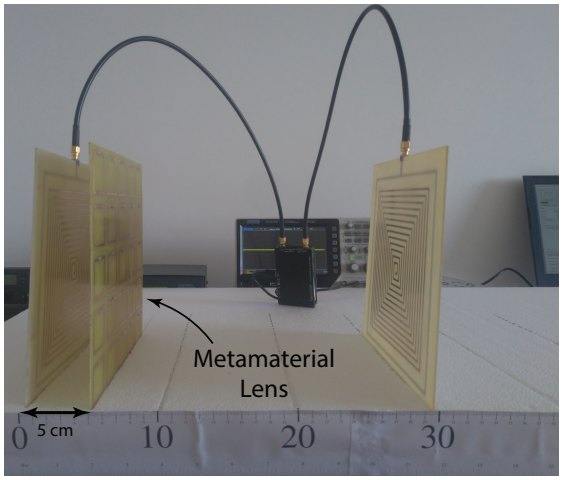

(b) With metamaterial lens.

Figure 5.6 – Setup for RWPT efficiency measurement.

Considering this described setup, it is possible to evaluate the maximum achievable efficiency of an RWPT system, to characterise the effective metamaterial properties, as well as to quantitatively analyse the influence of these structures in RWPT efficiency enhancement.

For the tests in which the transmitter must be connected to an RF power source, it is used the HF transceiver Emperor TS-5010 which operates in the 11 and 10 m bands ($26 - 30\ MHz$) with maximum output power level around $22\ W$. Specifically for the experiments described in this section, the transceiver is set at its FM function in order to send a sinusoidal carrier without modulation at the frequency of $28\ MHz$ and with power level of $10\ W$, as shown in Figure 5.7. Since the VSWR of the designed RWPT systems are relatively high, the power level was limited, and the transmission is enabled for a short time interval, just enough to perform the measurements. The specific details of the setup used for each experiment are provided in the following sections.

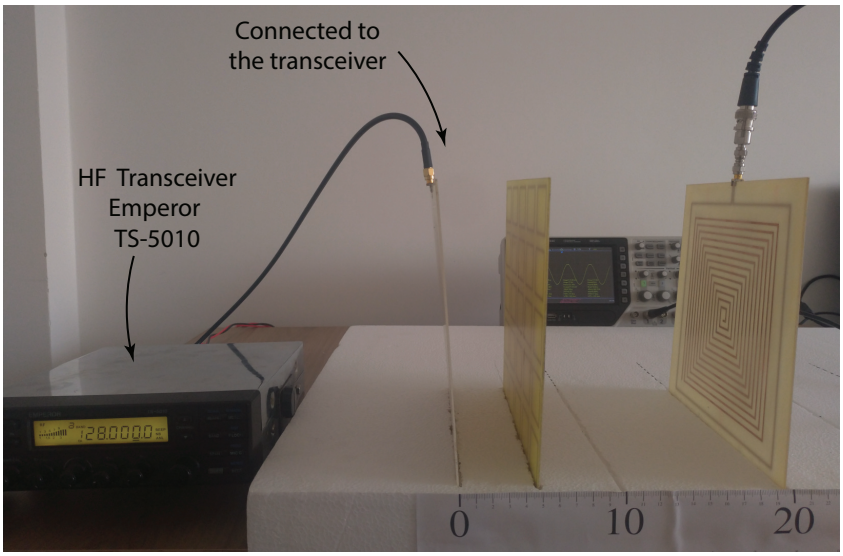

Figure 5.7 – Setup used for the power transfer measurement.

5.3 Characterization of the metamaterial lenses

In order to characterize the effective magnetic permeability of the RWPT with a metamaterial lens, the measurement procedure detailed in section 4.2 was applied with the setup described in section 5.2. In this case, the transmitting and receiving resonators of the four-coil RWPT system were used as drive and pickup coil, and they were positioned $10\ cm$ apart. First, the S_{21} parameter was measured without any lens, and this measurement is used as a reference. Then, the metamaterial slabs were positioned in between them and the S_{21} was measured for each sample. Thereby, the effective permeability can be calculated according to equation 4.8.

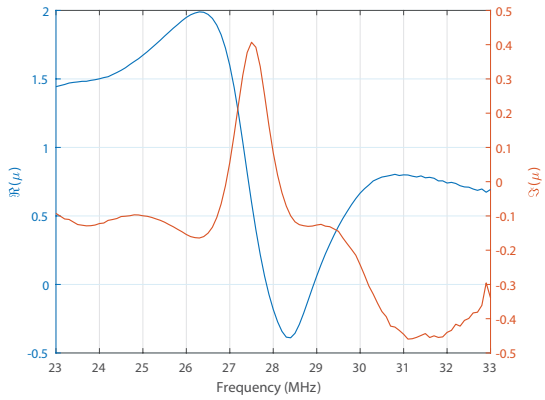

(a) Uniform lens

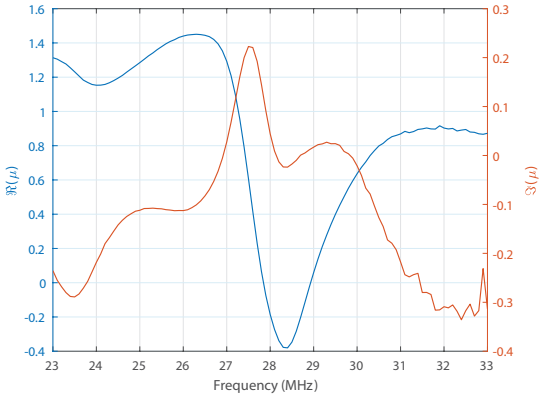

(b) Converging lens

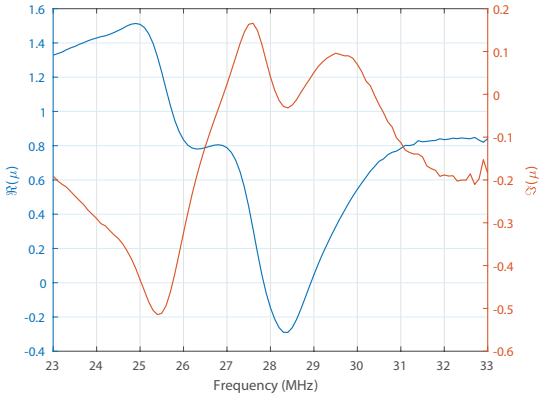

(c) Diverging lens

Figure 5.8 – Measured real and imaginary parts of the effective magnetic permeability of the designed metasurface lenses in the four-coil RWPT system.

The four-coil RWPT system was used for this measurement because it is in resonance at the metamaterial lens operation frequency, which makes the manipulation of the effective permeability more evident.

The results for the real and imaginary parts of the effective magnetic permeability are shown in Figure 5.8 for the three designed lenses. As it can be noticed, all of them operate at $28\ MHz$ since, in this frequency, all metamaterials slabs led to effective negative permeability of the RWPT system. Besides that, the imaginary part reaches its maximum in a frequency below the operating frequency; thus, the region of maximum losses in the metamaterial lens is avoided. The negative values for the imaginary part are due to measurement imprecision, that is higher for the frequencies outside the resonance.

When the converging lens and the diverging lens results shown in Figures 5.8b and 5.8c, respectively, are compared with the uniform lens it can be seen that in both of them the lens also affects the frequencies around their operating range. That is due to the fact that, as different capacitances are used to create a refractive index gradient, but

the dimensions of the unit cells are maintained, the resonant frequency of each cell is slightly shifted from $28\ MHz$.

5.4 Maximum efficiency measurement

With the scattering parameters matrices measured as described in section 5.2, it is possible to evaluate the efficiency of an RWPT system. The forward complex transmission coefficient S_{21} is related to the RWPT efficiency η_{RWPT}, according to the equation (SONG; BELOV; KAPITANOVA, 2017):

$$\eta_{RWPT} = \frac{|S_{21}|^2 \left(1 - |\Gamma_L|^2\right)}{\left(1 - |\Gamma_{in}|^2\right) |1 - S_{22}\Gamma_L|^2}, \tag{5.1}$$

where Γ_{in} and Γ_L are the reflection coefficient at the source and at the load, respectively. Assuming that the RWPT system is perfectly matched, that is, $\Gamma_{in} = \Gamma_L = 0$, the maximum achievable efficiency is given by:

$$\eta_{RWPT} = |S_{21}|^2 . \tag{5.2}$$

Even though in real applications, there will always be a certain level of impedance mismatching; this maximum achievable efficiency is an important metric for the evaluation of an RWPT system. Then, the measured efficiency for the two-coil and four-coil prototypes are shown in Figures 5.9 and 5.10, respectively.

In the maximum efficiency for the two-coil RWPT system presented in Figure 5.9, the results at $28\ MHz$ and $10\ cm$ are highlighted in the y-axis. As it can be noticed, for this situation, the maximum achievable efficiency, 2.076%, happens in the case without any lens. This can be explained by the fact that as the transmitting and receiving resonators are tuned with a lumped capacitor but, nevertheless, they are out of resonance, the presence of the metamaterial lens detune the resonators and, since the whole system is not resonant, the lens acts as a loss source instead of enhancing the coupling between coils.

On the other hand, when the RWPT system is properly tuned at the operation frequency of the metamaterial lens, a significant increase in the maximum achievable efficiency is observed in Figure 5.10. For instance, the efficiency is about 8% at the frequency of $28\ MHz$ with a distance between resonators equal to $20\ cm$. However, when the converging lens is included this efficiency increases to almost 33%. By way of comparison, the same measurement with a uniform lens leads to an efficiency of 17.59%. Conversely, as the diverging lens collimates the magnetic field at the border, it can be noticed that the maximum efficiency is much lower when compared with the other lens. Nevertheless, it is still higher than the case without any lens.

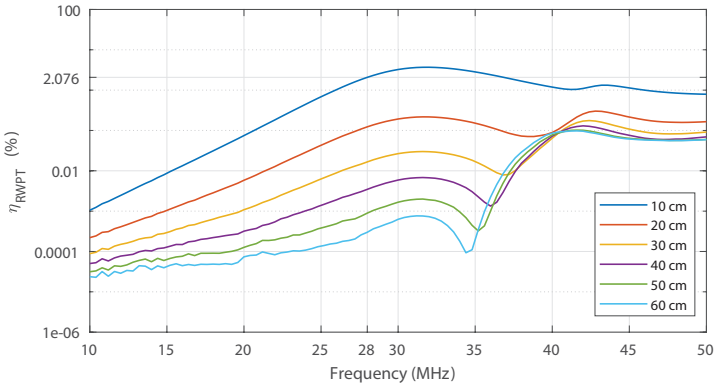

(a) Without lenses

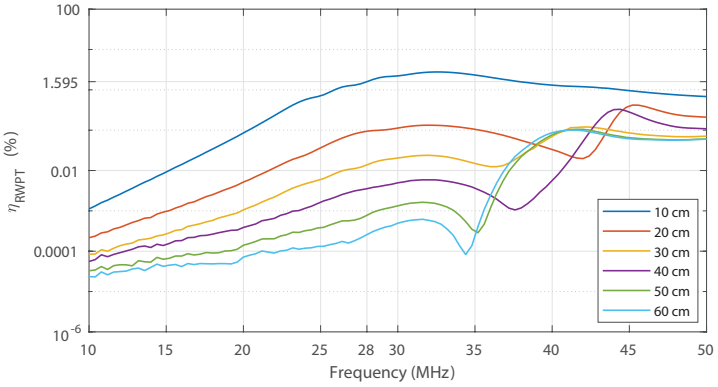

(b) Uniform lens

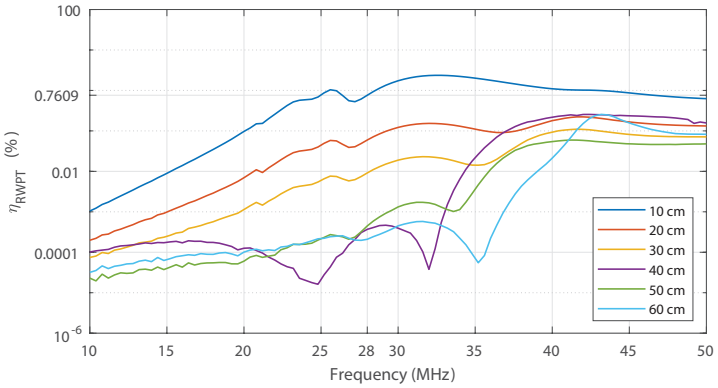

(c) Converging lens

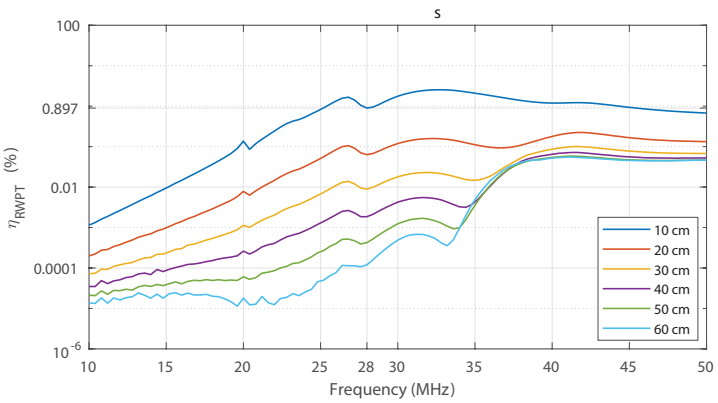

(d) Diverging lens

Figure 5.9 – Measured results for the maximum efficiency of the two-coil RWPT prototype.

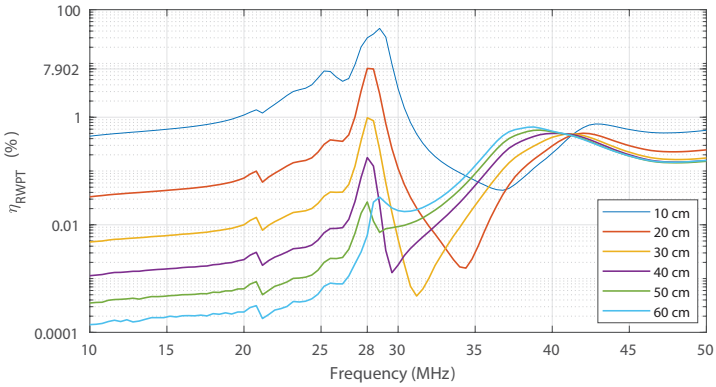

(a) Without lenses

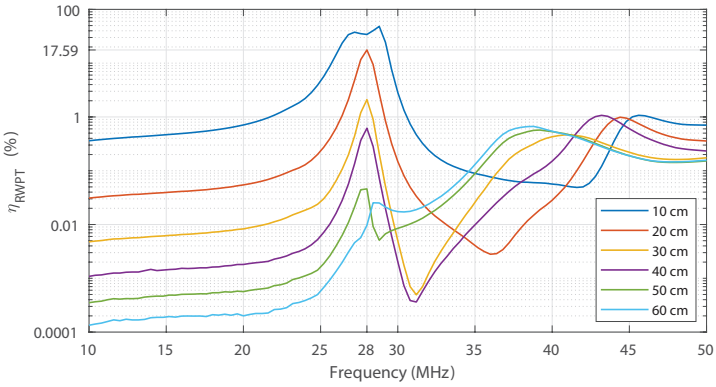

(b) Uniform lens

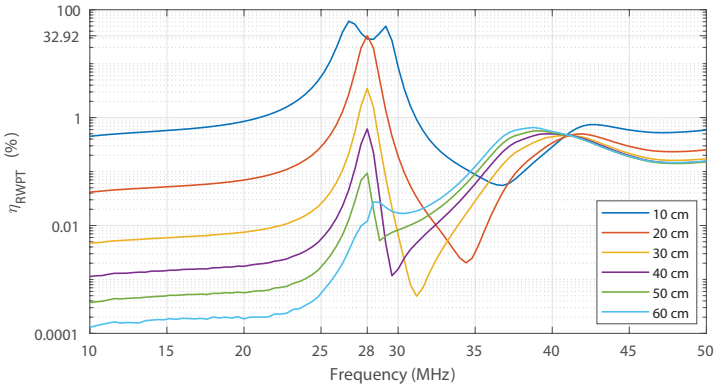

(c) Converging lens

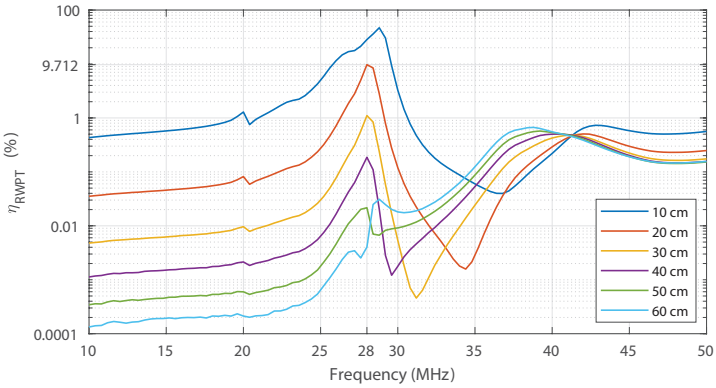

(d) Diverging lens

Figure 5.10 – Measured results for the maximum efficiency of the four-coil RWPT prototype.

5.5 Power transfer measurement

For the power transfer experiment, a coplanar half-wave and a full-wave rectifier circuit were designed. For the impedance matching, it is considered the output impedance of the four-coil RWPT system with a separation between resonators equal to 30 cm, measured without any lens. Due to the transmitting power level, the electronic components were chosen in order to handle higher received power levels. Therefore, it is used the Schottky diode SS14 (1N5819), that is indicated for rectifying operations at the HF band with rated current equal to $1\ A$. These circuits are optimized with the electronic design software Advanced Design System (ADS®), and they are shown in Figure 5.11. For the optimization, it is used the Genetic Algorithm present in ADS® with its default settings, to minimize the load reflection coefficient at $28\ MHz$. Then, these circuits are prototyped, as it can be seen in Figure 5.12. It must be highlighted that the optimized load for the full-wave rectifier is equal to $23\ \Omega$, whereas for the half-wave rectifier it is $56\ \Omega$.

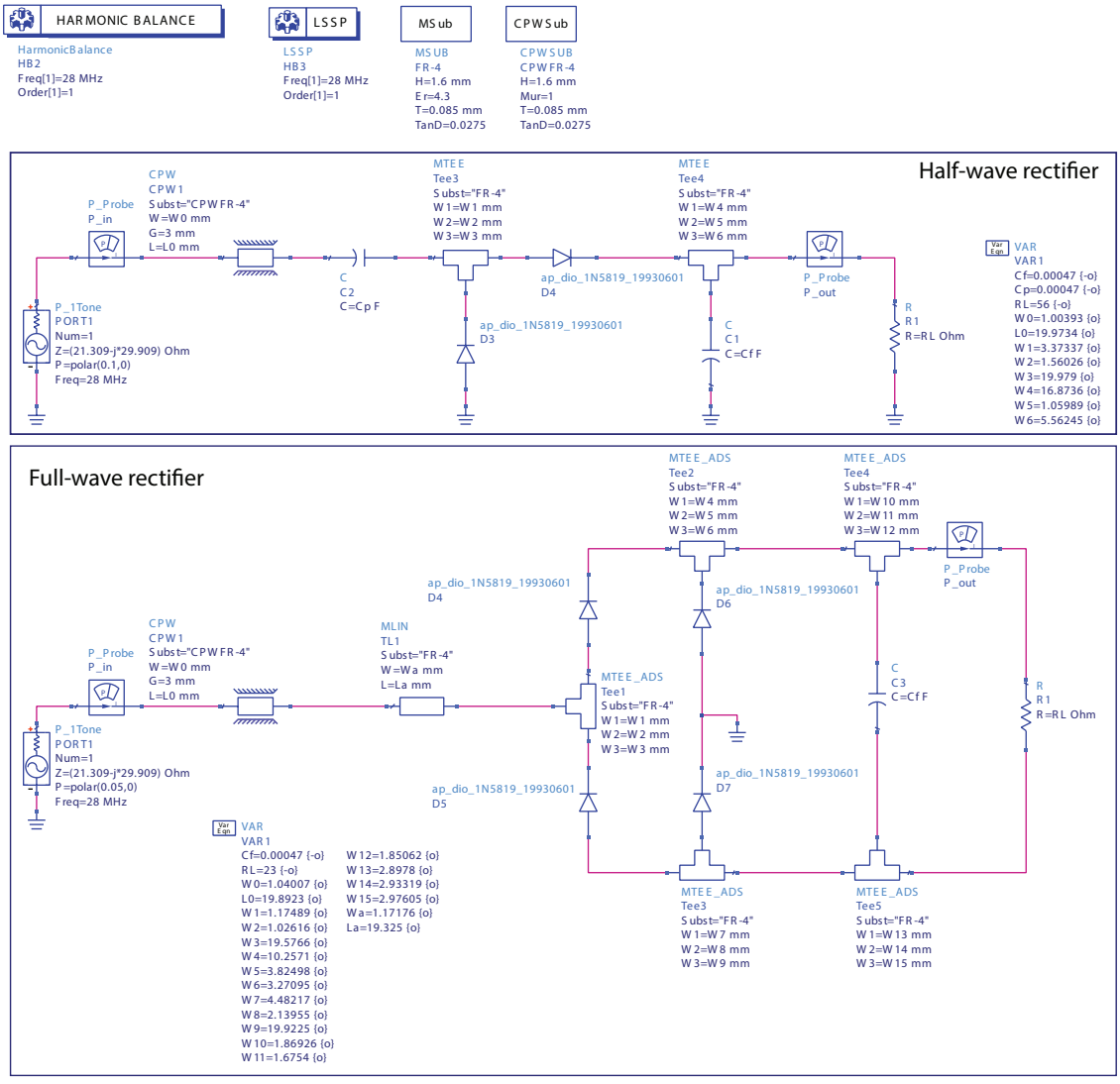

Figure 5.11 – Design of the half-wave and full-wave rectifiers.

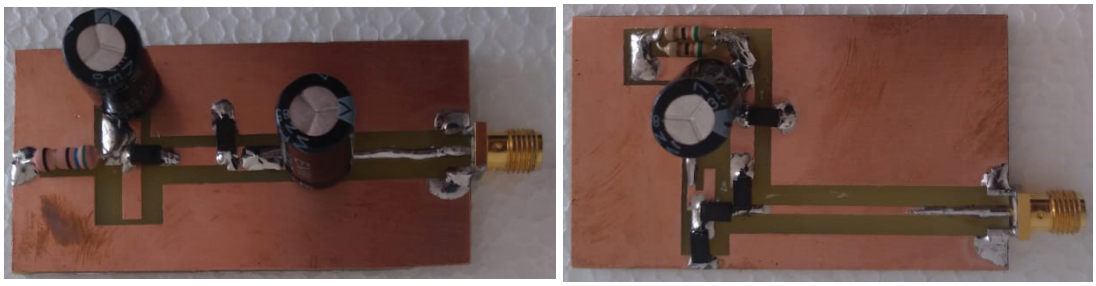

(a) Half-wave rectifier. (b) Full-wave rectifier.

Figure 5.12 – Rectifier circuit prototypes.

The setup used for the power transfer measurement is represented in the block diagram in Figure 5.13. The transceiver applies $10\ W$ at $28\ MHz$ in the transmitter coil, and the voltage on the rectifier load that is connected to the receiver coil is measured with an oscilloscope. These measurements are also accomplished in $10\ cm$ steps, from 10 to $60\ cm$. However, in this experiment, only the four-coil RWPT system is used, once it reveals to be much more efficient than the two-coil system prototyped. The measured power delivered to the load P_{out} and the realized efficiency can be seen in Figure 5.14, with and without lenses.

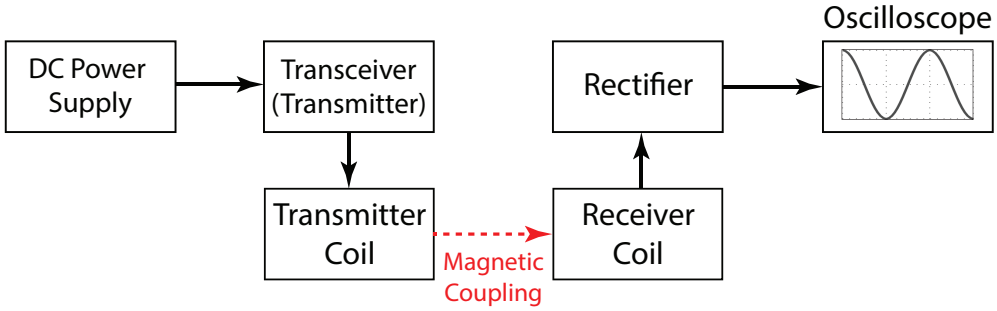

Figure 5.13 – Block diagram for the power transfer measurement.

In the results presented in Figure 5.14, the power and efficiency measured with the receiver at $20\ cm$ from the transmitter are highlighted. The continuous line denotes the measurements with the full-wave rectifier, whereas the half-wave rectifier is denoted by the dashed line. From these results it can be noticed that the realized efficiency in the case without any lens is very close to the maximum achievable efficiency indicated in Figure 5.10; this happens since the rectifier was designed to match the system output impedance at this condition. It must also be noticed that for the case with the half-wave rectifier, the realized efficiency is slightly higher than the maximum achievable previously presented. It is due to the fact that, for the S-parameters measurements, the nanoVNA applies a signal with a low power level that causes this difference when compared with the efficiency measurements accomplished with a higher input power. Nonetheless, even with this difference, both results are in agreement.

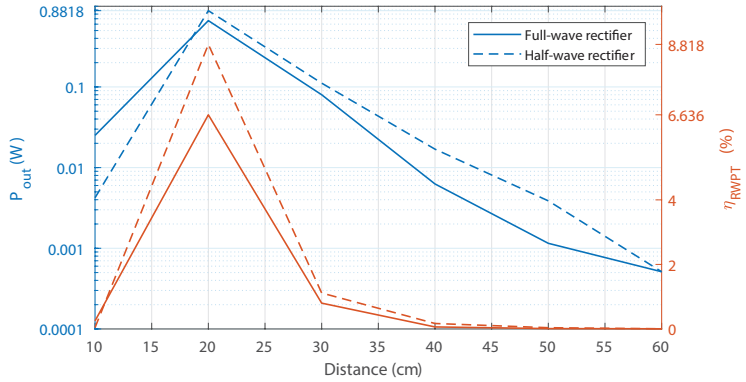

(a) Without lenses

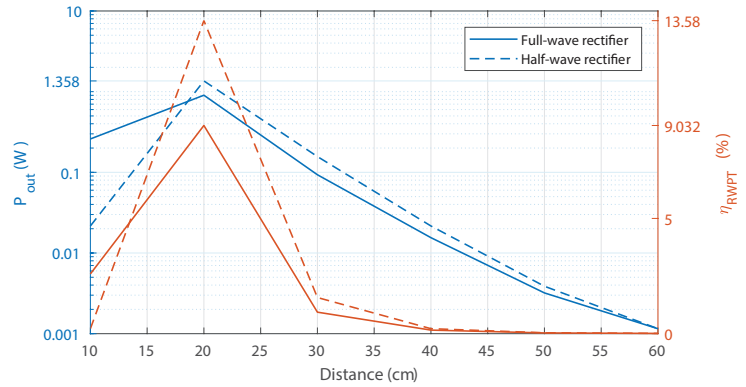

(b) Uniform lens

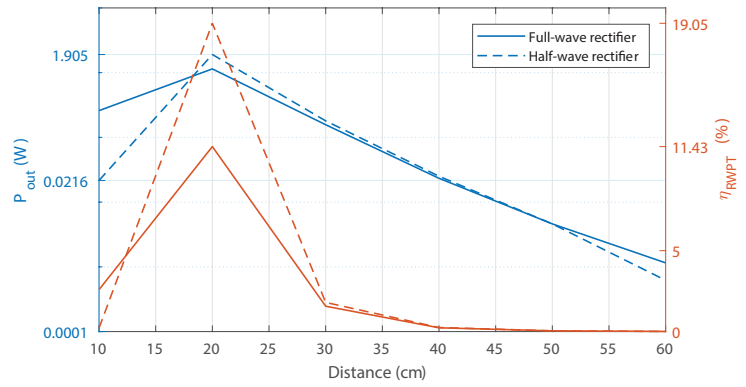

(c) Converging lens

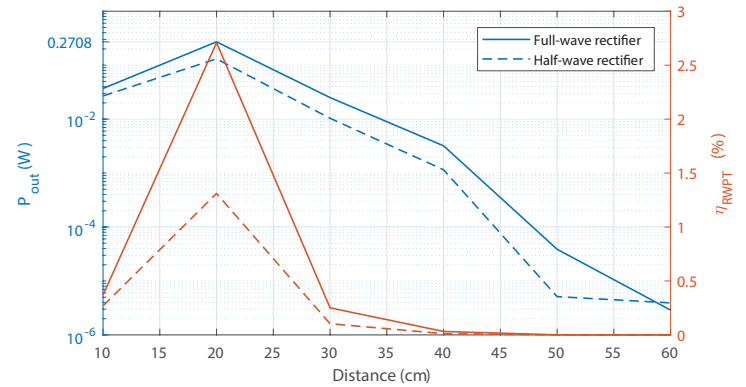

(d) Diverging lens

Figure 5.14 – Measured results for the power delivered to the load and realized RWPT efficiency.

When the metamaterial lenses are included, it can be seen that, due to the mismatching between receiver output impedance and rectifier input impedance, the RF-DC conversion efficiency is lower, causing a reduction on the RWPT efficiency when the realized and maximum achievable values are compared. However, the measured behaviours resemble those previously discussed. The highest realized efficiency and power delivered to the load is achieved in the condition with converging lens, with maximum measured power level equal to $1.905\ W$. Conversely, as the magnetic field collimation reduced the induced voltage at the receiver, the realized efficiency, in this case, is also lower. For this case, it should be noticed that the full-wave rectifier was slightly more efficient once its efficiency is closer to the output impedance with the diverging lens, when compared with the half-wave rectifier.

In the maximum achievable efficiency for the four-coil RWPT system with converging lens presented in Figure 5.10c, it is possible to see that, when the separation between transmitting and receiving resonator is equal to $10\ cm$, the system is on the over-coupling region and the frequency splitting phenomena can be observed. In this case, instead of achieving a higher efficiency at $28\ MHz$, the maximum efficiency is shifted to $26.8\ MHz$ and $29.20\ MHz$. This behaviour also explains the reason that leads to the low values for the power delivered to the load in this condition, $0.02\ W$, whereas in $20\ cm$ it increases to $1.905\ W$.

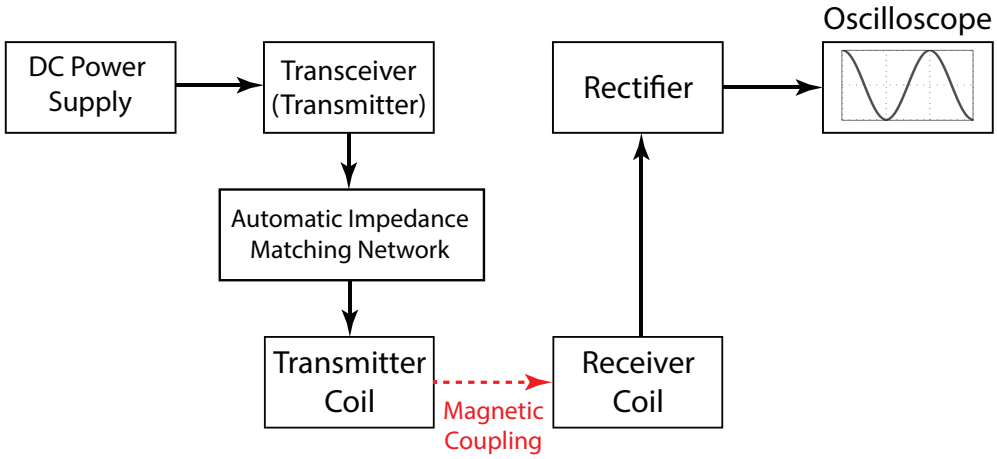

Figure 5.15 – Block diagram for the power transfer measurement with automatic impedance matching.

In order to verify the frequency splitting phenomena mitigation discussed in section 2.3, the experiment presented on the block diagram in Figure 5.15 was schematized. Basically, the four-coil resonators were positioned $10\ cm$ apart, and, as shown in Figure 5.16, the converging lens was positioned between them. Between the transceiver output and the transmitter resonator input, an automatic impedance matching network was added. This network has an inner measurement bridge that, based on the transmitted and reflected power level, automatically tunes its LC network parameters to reduce

the VSWR. The half-wave resonator was connected to the receiving resonator, and the voltage delivered to the load was measured with the oscilloscope.

As it is indicated in Figure 5.16, when the network matches the source and the resonator impedance, the measured VSWR is 1.7 with a transmitter power equal to $8\ W$. In this case, the measured power delivered to the load is $903.17\ mW$, which corresponds to 11.3% of the realized RWPT efficiency. Therefore, the power at the load increases by approximately 42 times when compared with the same measurement without the impedance matching. It must be pointed out that the frequency splitting phenomena still happens due to the over-coupling between resonators, this can be verified by the fact that the efficiency at $20\ cm$ is higher; however, the automatic impedance network significantly attenuates this effect.

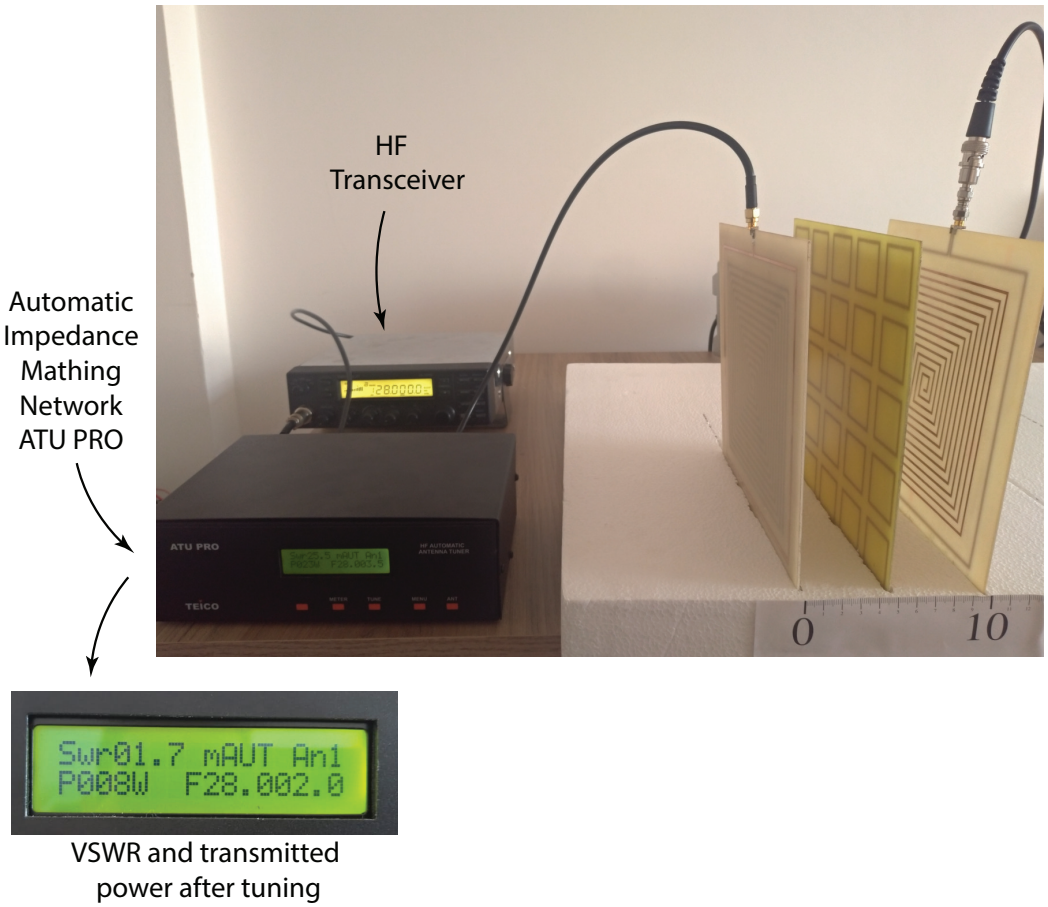

Figure 5.16 – Setup used for the power transfer measurement with automatic impedance matching.

5.6 Partial conclusions

In this chapter, several experiments were accomplished in order to verify the behaviour of two-coil and four-coil RWPT systems and their efficiency, with and without the designed metamaterial lenses. First, the transmitting and receiving resonators for each

case were optimized to operate at the same frequency of the metamaterial lenses. It was noticed from simulations and S_{11} measurements that the four-coil system is more flexible, allowing better tuning of the resonant frequency and minimization of the reflection coefficient. Then, the metamaterial lenses were experimentally characterized and, through the calculation of the effective magnetic permeability, it was shown that all three lenses present negative permeability at the operating frequency.

Afterwards, the maximum achievable RWPT efficiency was calculated based on S-parameters measurements. It was noticed that the highest efficiency is obtained with the converging lens, which is also verified in the power transfer measurements. At the same time, as the transfer quality factor is increased, the frequency splitting phenomenon is more explicit when this lens is applied. Finally, it has been proven that, by automatically matching the source and the RWPT system input impedance, it is possible to significantly increase the power transfer efficiency when the resonators are overcoupled. Therefore, it mitigates the effects of frequency splitting, even though it is not eliminated.

6 Final Considerations

6.1 Conclusions

The primary aim of this work is to analyse, from the theoretical, computational and experimental point of view, the influence of magnetic metasurface lenses in the efficiency of Resonant Wireless Power Transfer systems (RWPT). With this objective in mind, different studies have been realized.

Firstly, the concept of the RWPT technique and its operation principle is discussed and analysed. Opposed to the inductive wireless power transfer system, in this case, the transmitter and receiver coils are coupled through the magnetic field at their resonant frequency, which significantly increases the coupling between them. Even though different topologies and configurations can be used to physically implement this technique, in this work, the two-coil and four-coil RWPT system are used as references. Thereby, the circuit models of both systems are presented and, from them, it is possible to analyse the factor that affects the power transfer efficiency. From all the analysis accomplished, it is possible to notice that the coupling between the coils and the mismatching between the input and output impedances with the source and load impedances are the main factor that influences the RWPT system behaviour.

It was verified that the efficiency sharply increases with the transfer quality factor, which is used as a factor of merit for the analysis in this work. Thus, in an ideal system, the efficiency would asymptotically approach the unit as the distance between coils decreases. However, in real applications, if the coils are overcoupled, the maximum efficiency is split into two smaller peaks deviated below and above the resonant frequency. It was also shown that, by automatically matching the system input impedance with the source impedance, this frequency splitting phenomenon could be attenuated even though it cannot be completely suppressed.

In addition to it, a manner to enhance the efficiency of RWPT systems through the manipulation of the effective magnetic permeability is discussed. In this proposal, an additional resonator is added in the vicinity of the transmitting resonator and the interactions between the transmitting and the added resonator magnetic dipole moments leads to an increase in the coupling between the transmitter and receiver, thus increasing efficiency.

This principle is physically realisable through metamaterials lenses that, conversely to the conventional lenses, are able to collimate the evanescent field at the reactive near

field region, thus overcoming the diffraction limit. Specifically for magnetic metasurface lenses in RWPT applications, the resonance intensifies the magnetostatic wave amplification, which is only limited by the losses in the metamaterial.

Even though the circuit model can be used to easily visualise the RWPT system behaviour, it is limited because it cannot model the electromagnetic field dynamic in these systems, and it cannot fully explain the interaction between the transmitting and receiving resonators and the metamaterial lenses. On the other hand, a tridimensional full-wave simulation in computational aided design software is computationally costly and time-consuming, what complicates the design of an RWPT system loaded with metamaterial lenses. In this context, this work proposes an alternative and a simplified formulation with a low computational cost that enables fast analysis of these systems.

The proposed approach applies the thin-wire approximation to simplify the integro-differential formulation of thin microstrip structures. As the size of RWPT systems and metamaterials lenses have dimensions much smaller than the wavelength at their operating frequency, this approximation is justified. Then, this mathematical formulation was computationally implemented and solved through the Method of Moments (MoM).

In order to validate the proposed implementation, the error of the thin wire solution was evaluated by comparing the calculated results with those simulated in FEKO, that is a commercial software that also applies the MoM in its solver. Comparisons that took into account the geometry discretization size, wire diameter and number of Gauss points, revealed that the proposed implementation is in close agreement with the reference results. Moreover, after extending this formulation to microstrip structures and comparing with measured data, it is verified that this formulation is valid, and it allows a faster calculation of reflection coefficient, input impedance and near-field results.

From the presented results, it can be noticed that the greater deviation is obtained for the case in which a lumped impedance is added in the geometry. It is explained by the fact that, in the way that the structure is discretized, that is, by prioritizing the obedience to the thin-wire conditions, the implemented size of the lumped component not necessarily corresponds to its physical packaging size. Moreover, depending on the discretization size, the effect of the integral singularities surpasses the lumped impedance, leading to a higher error. Finally, the implemented algorithm defines the discretization to a single frequency point. Thus, for frequencies far away from the specified, the error also tends to increase.

Despite these aforementioned points, the proposed formulation and implementation met the expected objectives for this work, as it can be used for a qualitative analysis of metamaterial lenses for RWPT applications.

For instance, three metamaterial lenses based on the refractive index gradient profile provided by the application of Transformation Optics are designed and prototyped. These metasurface lenses allow the magnetic field collimation in a specific direction, with behaviour similar to optical converging and diverging lens. In addition to it, one uniform lens in which all unit cells have the same refractive index is used as a reference. The simulations carried out in this uniform lens, with the proposed numerical implementation, qualitatively proves the collimation of the magnetic field generated by a coil.

Finally, experiments were realized with the uniform, converging and diverging metasurface lenses applied on two-coil and four-coil systems designed to operate at $28\ MHz$, which is the same operating frequency of the lenses. Firstly, from the design perspective and the reflection coefficient measurements, it is noticed that with the four-coil system, it is easier to get a more compact resonator. It happens because, as the drive coil is not physically connected to the transmitting resonator, it is less sensitive to constructive variations and, as it is possible to compensate its inductive reactance with its self-capacitance, it does not require lumped capacitances that add uncertainties to the design. Moreover, as the transmitting resonator in the four-coil system is not directly connected to the source, its quality factor is higher.

Based on the scattering parameters matrix measurement, the metamaterial lenses were characterized and the maximum achievable efficiency was calculated. It has been shown that all designed metasurfaces presented negative values for the real part of the effective magnetic permeability at $28\ MHz$, and the maximum value of the imaginary part occurs before this frequency. Thereby, the frequency range with higher losses in the metamaterial slab is avoided. It was also observed that, as the converging and diverging lenses use capacitors in order to produce a gradient of the refractive index, the frequencies around the resonant are also affected by these lenses.

Furthermore, the calculated values for the maximum achievable frequency, that is, the efficiency that is obtained when the mismatching with the source and load are disregarded reveal that the highest efficiency is achieved for the four-coil RWPT system with the converging lens. That is justified by the fact that, as the magnetic field is focused at the centre of the lens and the receiving resonator is coaxially aligned to it, the magnetic coupling is significantly enhanced in this case. And, as presented in the circuit analysis in chapter 2, the transfer quality factor increases. It is also in this case that the frequency splitting phenomenon is more evident, revealing that, at 10 cm, the resonators with the converging lens are in the overcoupled region. In addition to it, it has also been shown that, even the diverging lens that led to the lowest efficiency among the lenses, presented better results than without any lenses.

The power transfer and the associated realized efficiency were also calculated by measuring the power delivered to the load when a rectifier is connected to the system output. As expected, the highest received power level was verified on the four-coil system with the converging lens, when the transmitting and receiving resonator were positioned 20 cm apart. At this point, the measured efficiency was around 19%. The reduction in the efficiency in this case, when compared with the maximum achievable efficiency is due to the mismatching between the system output impedance and the rectifier impedance, since the rectifier was designed based on the system without lenses. For this reason, the maximum and realized efficiency without a lens are in close agreement.

Finally, in order to verify the efficiency enhancement by the automatic impedance matching at the frequency splitting situation, the four-coil RWPT system with the converging lens and separation between resonators equal to 10 cm was connected to an automatic impedance matching network, and it was verified an efficiency 42% higher at this position.

Therefore, based on the performed analysis and the results discussed in this dissertation, it is proven that the goals proposed in this work have been accomplished.

6.2 Future works

Based on the present conclusions, some actions can be developed in order to improve this project continuously.

The mathematical formulation and its numerical implementation for thin microstrip structures reveal a significant potential to analyse RWPT structures and magnetic metasurface lenses. In this work, for instance, qualitative analysis can be already performed, as demonstrated. However, some improvements regarding its computational implementation would lead it to its full potential.

First, regarding the geometry treatment, it is essential to develop a discretization refinement algorithm. It would allow the proper modelling of lumped elements and sources, reinforcing the use of their physical size and leading to higher accuracy for modelling structures with lumped impedances. This algorithm would also improve the numerical representation of systems with different sizes, for instance, the modelling of RWPT resonators and metamaterial lenses together. Since the size of the resonator is much greater than the unit cell size, a uniform discretization is not the best option. This improvement would allow not only a qualitative analysis of these structures, but also would make it possible to get approximate values for the parameters used in this work, such as the RWPT efficiency, the power delivered to the load, and the effective magnetic permeability.

After this enhancement in the computational implementation, an optimization algorithm could be implemented in order to allow also the synthesis and design of RWPT resonators and metamaterial lenses. In addition to it, by applying high-performance computing methods such as parallel processing, it would be possible to design large structures with a very short processing time.

Regarding the design of the metamaterial lenses, by applying the procedure proposed in this work, it is possible to design active metasurface lenses, in which the collimation direction can be controlled and readjusted. For this, the lumped capacitor in each unit cell is replaced by a tuning circuit based on varactor diodes, and, by controlling the bias voltage of each varactor, their capacitance can be changed, thus changing the refractive index gradient direction of the metamaterial lenses.

From the presented results, it is possible to see that, even though unit cells with the same size simplifies the construction and the numerical implementation, in this case, there will always be a small deviation of the resonant frequency between unit cells. Therefore, in this case, the capacitance value needs to be carefully chosen as in this work; otherwise, the metasurface lens could not work properly. On the other hand, multiple metasurface lenses with slightly different operation frequencies can be used together to increase its bandwidth.

Finally, as developed, the RWPT efficiency can be increased by increasing the quality factor of the resonators. However, a high-quality factor structure has a high VSWR, considering 50Ω as the reference impedance. Therefore, it is possible to design a dedicated transmitter for feeding these systems, with impedance designed to match the system impedance. Also, reactance compensation circuits can be further investigated in order to improve the efficiency of the system presented in this work. This analysis was accomplished so far, since it does not belong to the scope of this work.

The magnetic resonant coupling principle and the effect of metasurface lenses on the magnetostatic wave were investigated for power transfer applications. However, it can also be applied to short and middle-range wireless communications. Therefore, further studies can be realized to investigate the data transmission and reception on the presence of metasurface lenses.

6.3 Publications

Some experiments and the results obtained from them during the development of this work were presented in scientific conferences and journals. These results cover the theoretical aspects discussed in this dissertation, but also reveals different approaches and applications. The submitted works and in-development publications are listed

below:

1. **A Novel Magnetic Metasurface Lens for Wireless Power Transfer**:
   Presented at the 18th Biennial IEEE Conference Electromagnetic Field Computation (CEFC 2018);
2. **Magnetic Metamaterial Lenses for Resonant Wireless Power Transfer:**
   Presented at the 2019 IEEE Magnetic Summer School;
3. **Analysis of Metamaterial Permeability on the Performance of Loosely Coupled Coils:**
   Presented at the 2019 International Conference on Computational Electromagnetics, Electrodynamics, Methods and Applications (ICCEEMA 2019);
4. **Electromagnetic Energy Harvesting Using a Glass Window:**
   Published in the Journal of Microwaves, Optoelectronics and Electromagnetic Applications (March 2020);
5. **Design of artificial magnetic conductor metasurfaces using generalized boundary conditions:**
   Published in the Journal of Electromagnetic Waves and Applications (April 2020);
6. **Magnetic Metasurface Lenses for Resonant Wireless Power Transfer Applications:**
   Submitted to the Journal of Electromagnetic Waves and Applications;
7. **Controlled Magnetic Field Collimation by Active Metasurface Lens:**
   Submitted to the 2020 Magnetism and Magnetic Materials Conference (MMM 2020).

Bibliography

ABDOLALI, A.; SEDEH, H. B.; FAKHERI, M. H. Geometry free materials enabled by transformation optics for enhancing the intensity of electromagnetic waves in an arbitrary domain. **Journal of Applied Physics**, v. 127, n. 5, p. 054902, 2020. Cited in page 65.

AHN, D.; KIANI, M.; GHOVANLOO, M. Enhanced wireless power transmission using strong paramagnetic response. **IEEE Transactions on Magnetics**, v. 50, n. 3, p. 96–103, 2014. Cited 4 times in page 3, 18, 19, and 20.

ALMEIDA, J. V. de; FEITOZA, R. S. Metamaterial-enhanced magnetic coupling: An inductive wireless power transmission system assisted by metamaterial-based μ-negative lenses. **IEEE Microwave Magazine**, v. 19, n. 4, p. 95–100, 2018. Cited 2 times in page 7 and 61.

ANOWAR, T. I. et al. High-efficiency resonant coupled wireless power transfer via tunable impedance matching. **International Journal of Electronics**, Taylor Francis, v. 104, n. 10, p. 1607–1625, 2017. Cited in page 18.

BAHL, I. J.; TRIVEDI, D. K. A designer's guide to microstrip line. **Microwaves**, v. 16, p. 174–182, 1977. Cited in page 53.

BAKIR, M. et al. Metamaterial characterization by applying different boundary conditions on triangular split ring resonator type metamaterials. **International Journal of Numerical Modelling: Electronic Networks, Devices and Fields**, v. 30, n. 5, p. e2188, 2017. Cited in page 69.

BALANIS, C. **Antenna Theory: Analysis and Design**. 4. ed. [S.l.]: Wiley-Interscience, 2016. Cited 3 times in page 24, 37, and 53.

BINGLER, A. et al. Integral equation formulations for modeling wireless power transfer systems in close proximity to foreign objects. **IEEE Transactions on Magnetics**, v. 55, n. 6, p. 1–4, 2019. Cited in page 3.

BONDESON, A.; RYLANDER, T.; INGELSTROM, P. **Computational Electromagnetics**. 2. ed. [S.l.]: Springer, 2012. Cited in page 25.

BRANDAO, G. L. F. et al. Design of artificial magnetic conductor metasurfaces using generalized boundary conditions. **Journal of Electromagnetic Waves and Applications**, Taylor Francis, v. 34, n. 10, p. 1502–1512, 2020. Cited in page 62.

CHAUDHARY, K.; KUMAR, D. Satellite solar wireless power transfer for baseload ground supply: clean energy for the future. **European Journal of Futures Research**, v. 6, n. 1, 2018. Cited in page 2.

CHEN, W.-C. et al. Extremely subwavelength planar magnetic metamaterials. **Phys. Rev. B**, American Physical Society, v. 85, p. 201104, May 2012. Cited 2 times in page 64 and 65.

CHOWDHURY, D.; PAL, M.; GHATAK, R. Vicsek fractal slot substrate integrated waveguide leaky wave antenna for x-band application. **Journal of Electromagnetic Waves and Applications**, Taylor Francis, v. 32, n. 10, p. 1212–1220, 2018. Cited in page 62.

CORREA, D. C.; RESENDE, U. C.; BICALHO, F. S. Experiments with a compact wireless power transfer system using strongly coupled magnetic resonance and metamaterials. **IEEE Transactions on Magnetics**, v. 55, n. 8, p. 1–4, 2019. Cited in page 3.

CRUCIANI, S. et al. Active shielding design for wireless power transfer systems. **IEEE Transactions on Electromagnetic Compatibility**, v. 61, n. 6, p. 1953–1960, 2019. Cited in page 3.

CUI, T. J.; LIU, R.; SMITH, D. **Metamaterials: Theory, Design, and Applications**. 1. ed. [S.l.]: Springer-Verlag US, 2010. Cited in page 61.

ENGIN, A. E. et al. Closed-form multipole debye model for time-domain modeling of lossy dielectrics. **IEEE Transactions on Electromagnetic Compatibility**, v. 61, n. 3, p. 966–968, 2019. Cited 2 times in page 54 and 55.

ESKANDARI, H.; TYC. Controlling refractive index of transformation-optics devices via optical path rescaling. **Scientific Reports**, v. 9, n. 1, 2019. Cited in page 66.

FENG, G.; SIT, J. An injection-locked wpt transmitter with automatic maximum efficiency tracking. **IEEE Transactions on Industrial Electronics**, p. 1–1, 2020. Cited in page 18.

F.JOLANI; YU, Y.; CHEN, Z. A planar magnetically coupled resonant wireless power transfer system using printed spiral coils. **IEEE Antennas and Wireless Propagation Letters**, v. 13, p. 1648–1651, 2014. Cited in page 8.

GIBSON, W. C. **The Method of Moments in Electromagnetics**. 2. ed. [S.l.]: CRC Press, 2015. Cited 5 times in page 25, 26, 30, 31, and 34.

GILOAN, M. Designing devices for wave-vector manipulation using a transformation-optics approach. **Phys. Rev. Applied**, American Physical Society, v. 8, p. 014005, Jul 2017. Cited in page 66.

GUREL, L.; SERTEL, K.; ŞENDUR, I. K. On the choice of basis functions to model surface electric current densities in computational electromagnetics. **Radio Science**, v. 34, n. 6, p. 1373–1387, 1999. Cited in page 31.

HARRINGTON, R. **Field computation by moment methods**. Piscataway, NJ: IEEE Press, 1993. Cited in page 27.

HARRIS, W. C.; STANCIL, D. D.; RICKETTS, D. S. Improved wireless power transfer efficiency with non-perfect lenses. **Applied Physics Letters**, v. 114, n. 14, p. 143903, 2019. Cited 2 times in page 62 and 63.

HOURAN, M. A.; YANG, X.; CHEN, W. Magnetically coupled resonance wpt: Review of compensation topologies, resonator structures with misalignment, and emi diagnostics. **Electronics**, v. 7, n. 11, p. 296, 2018. Cited 2 times in page 1 and 9.

HUANG, R. et al. Frequency splitting phenomena of magnetic resonant coupling wireless power transfer. **IEEE Transactions on Magnetics**, v. 50, n. 11, p. 1–4, 2014. Cited in page 17.

JAKOBUS, U. et al. Tailoring feko for microwave problems. **IEEE Microwave Magazine**, v. 9, n. 6, p. 76–85, 2008. Cited in page 38.

JEONG, S.; LIN, T.; TENTZERIS, M. M. A real-time range-adaptive impedance matching utilizing a machine learning strategy based on neural networks for wireless power transfer systems. **IEEE Transactions on Microwave Theory and Techniques**, v. 67, n. 12, p. 5340–5347, 2019. Cited in page 18.

JIN, K.; ZHOU, W. Wireless laser power transmission: A review of recent progress. **IEEE Transactions on Power Electronics**, v. 34, n. 4, p. 3842–3859, 2019. Cited in page 2.

KACZMARCZYK, Z. et al. Chart design method for multi-coil resonant wireless power transfer systems. **IEEE Transactions on Power Electronics**, p. 1–1, 2020. Cited in page 8.

KIANI, M.; GHOVANLOO, M. An rfid-based closed-loop wireless power transmission system for biomedical applications. **IEEE Transactions on Circuits and Systems II: Express Briefs**, v. 57, n. 4, p. 260–264, 2010. Cited in page 7.

KURS, A. et al. Wireless power transfer via strongly coupled magnetic resonances. **Science**, v. 317, n. 5834, p. 83–86, 2007. Cited in page 7.

LEE, W. et al. Contactless energy transfer systems using antiparallel resonant loops. **IEEE Transactions on Industrial Electronics**, v. 60, n. 1, p. 350–359, 2013. Cited in page 18.

LIN, Y.; TANG, K. An inductive power and data telemetry subsystem with fast transient low dropout regulator for biomedical implants. **IEEE Transactions on Biomedical Circuits and Systems**, v. 10, n. 2, p. 435–444, 2016. Cited in page 7.

LU, F. et al. An inductive and capacitive integrated coupler and its lcl compensation circuit design for wireless power transfer. **IEEE Transactions on Industry Applications**, v. 53, n. 5, p. 4903–4913, 2017. Cited in page 18.

LU, X. et al. Wireless charging technologies: Fundamentals, standards, and network applications. **IEEE Communications Surveys Tutorials**, v. 18, n. 2, p. 1413–1452, 2016. Cited in page 7.

LUO, Z.-Q.; TSENG, P. Perturbation analysis of a condition number for linear systems. **SIAM Journal on Matrix Analysis and Applications**, v. 15, n. 2, p. 636–660, 1994. Cited in page 38.

MAO, S. et al. A polygonal double-layer coil design for high-efficiency wireless power transfer. **AIP Advances**, v. 8, n. 5, p. 056631, 2018. Cited in page 74.

MIKKI, S.; ALZAHED, A. M.; ANTAR, Y. M. M. The spatial singularity expansion method for electromagnetics. **IEEE Access**, v. 7, p. 124576–124595, 2019. Cited in page 33.

MOREIRA, M. V. **Avaliação do Espalhamento Eletromagnético por Estruturas Filamentares Utilizando o Método dos Momentos**. Master's Thesis: Centro Federal de Educação Tecnológica de Minas Gerais, 2012. Cited 2 times in page 30 and 31.

PENDRY, J. B. Negative refraction makes a perfect lens. **Phys. Rev. Lett.**, American Physical Society, v. 85, p. 3966–3969, Oct 2000. Cited 3 times in page 3, 62, and 63.

PENDRY, J. B. et al. Magnetism from conductors and enhanced nonlinear phenomena. **IEEE Transactions on Microwave Theory and Techniques**, v. 47, n. 11, p. 2075–2084, 1999. Cited in page 62.

PENDRY, J. B. et al. Extremely low frequency plasmons in metallic mesostructures. **Phys. Rev. Lett.**, American Physical Society, v. 76, p. 4773–4776, Jun 1996. Cited in page 62.

PEREIRA, L. M. D. **Investigação de um Sistema de Transmissão de Energia Elétrica sem Fios Utilizando Acoplamento Indutivo Ressonante**. Master's Thesis: Centro Federal de Educação Tecnológica de Minas Gerais, 2016. Cited in page 53.

POZAR, D. M. **Microwave Engineering**. 4. ed. [S.l.]: John Wiley Sons, 2011. Cited in page 36.

PRESS, W. H. et al. **Numerical Recipes in C++: The Art of Scientific Computing**. 3. ed. [S.l.]: Cambridge University Press, 2007. Cited in page 32.

PRESSLEY, A. **Elementary Differential Geometry**. 2. ed. [S.l.]: Springer, 2012. Cited in page 29.

PRIES, J. et al. A 50-kw three-phase wireless power transfer system using bipolar windings and series resonant networks for rotating magnetic fields. **IEEE Transactions on Power Electronics**, v. 35, n. 5, p. 4500–4517, 2020. Cited in page 3.

RESENDE, U. C. **Análise de antenas refletoras circularmente simétricas com a presença de corpos dielétricos**. PhD Thesis: Universidade Federal de Minas Gerais, 2007. Cited 3 times in page 24, 27, and 28.

RODA, J. **FR-4 opper clad laminate test report**. [S.l.: s.n.], 2018. Cited in page 55.

SHINOHARA, N. (Ed.). **Wireless Power Transfer: Theory, technology, and applications**. [S.l.]: Institution of Engineering and Technology, 2018. (Energy Engineering). Cited 2 times in page 3 and 8.

SMITH, D. R. et al. Gradient index metamaterials. **Phys. Rev. E**, American Physical Society, v. 71, p. 036609, Mar 2005. Cited in page 68.

SMITH, D. R.; PENDRY, J. B. Homogenization of metamaterials by field averaging. **J. Opt. Soc. Am. B**, OSA, v. 23, n. 3, p. 391–403, Mar 2015. Cited in page 64.

SOARES, I.; RESENDE, U.; SIQUEIRA, G. A novel magnetic metasurface lens for wireless power transfer. In: ____. **IEEE Conference on Electromagnetic Field Computation - CEFC 2018**. [S.l.]: IEEE, 2018. Cited in page 69.

SOARES, I. V. **Solução do Espalhamento Eletromagnético por Corpos Condutores Tridimensionais Utilizando o Método dos Momentos**. Bachelor's Degree Final Project: Centro Federal de Educação Tecnológica de Minas Gerais, 2017. Cited in page 24.

SOLYMAR, L.; SHAMONINA, E. **Waves in Metamaterials**. 1. ed. [S.l.]: Oxford University Press, 2009. Cited in page 63.

SONG, M.; BELOV, P.; KAPITANOVA, P. Wireless power transfer inspired by the modern trends in electromagnetics. **Applied Physics Reviews**, v. 4, n. 2, p. 021102, 2017. Cited 3 times in page 2, 7, and 80.

STECKIEWICZ, A.; CHOROSZUCHO, A. Optimization-based synthesis of a metamaterial electric cloak using nonhomogeneous composite materials. **Journal of Electromagnetic Waves and Applications**, Taylor Francis, v. 33, n. 14, p. 1933–1941, 2019. Cited in page 62.

TAN, T. et al. A bidirectional wireless power transfer system control strategy independent of real-time wireless communication. **IEEE Transactions on Industry Applications**, v. 56, n. 2, p. 1587–1598, 2020. Cited in page 3.

VERMA, H. K. et al. A low rcs wideband high gain cp slot antenna loaded with frequency selective surface. **Journal of Electromagnetic Waves and Applications**, Taylor Francis, v. 34, n. 7, p. 940–959, 2020. Cited in page 62.

VESELAGO, V. G. The electrodynamics of substances with simultaneously negative values of ε and μ. **Soviet Physics Uspekhi**, Uspekhi Fizicheskikh Nauk (UFN) Journal, v. 10, n. 4, p. 509–514, apr 1968. Cited in page 61.

WANG, B. et al. Experiments on wireless power transfer with metamaterials. **Applied Physics Letters**, v. 98, n. 25, p. 254101, 2011. Cited in page 68.

WANG, M. et al. Demagnetization weakening and magnetic field concentration with ferrite core characterization for efficient wireless power transfer. **IEEE Transactions on Industrial Electronics**, v. 66, n. 3, p. 1842–1851, 2019. Cited in page 18.

WU, Q. et al. Wireless power transfer based on magnetic metamaterials consisting of assembled ultra-subwavelength meta-atoms. **EPL (Europhysics Letters)**, IOP Publishing, v. 109, n. 6, p. 68005, mar 2015. Cited in page 65.

XU, C. et al. Multi-coil high efficiency wireless power transfer system against misalignment. In: **2018 IEEE MTT-S International Wireless Symposium (IWS)**. [S.l.: s.n.], 2018. p. 1–3. Cited in page 18.

YEO, T. et al. Design of maximum efficiency tracking control scheme for closed-loop wireless power charging system employing series resonant tank. **IEEE Transactions on Power Electronics**, v. 32, n. 1, p. 471–478, 2017. Cited in page 18.

YU, G. X. et al. Transformation of different kinds of electromagnetic waves using metamaterials. **Journal of Electromagnetic Waves and Applications**, Taylor Francis, v. 23, n. 5-6, p. 583–592, 2009. Cited in page 65.

ZHANG, C.; LIN, D.; HUI, S. Y. R. Ball-joint wireless power transfer systems. **IEEE Transactions on Power Electronics**, v. 33, n. 1, p. 65–72, 2018. Cited in page 18.

ZHANG, Y. **Key Technologies of Magnetically-Coupled Resonant Wireless Power Transfer**. 1. ed. [S.l.]: Springer, 2018. Cited 5 times in page 11, 13, 14, 15, and 16.

ZHANG, Y.; ZHAO, Z. Frequency splitting analysis of two-coil resonant wireless power transfer. **IEEE Antennas and Wireless Propagation Letters**, v. 13, p. 400–402, 2014. Cited in page 17.

ZHANG, Y.; ZHAO, Z.; CHEN, K. Frequency splitting analysis of magnetically-coupled resonant wireless power transfer. In: **2013 IEEE Energy Conversion Congress and Exposition**. [S.l.: s.n.], 2013. p. 2227–2232. Cited in page 18.

ZHANG, Y.; ZHAO, Z.; CHEN, K. Frequency-splitting analysis of four-coil resonant wireless power transfer. **IEEE Transactions on Industry Applications**, v. 50, n. 4, p. 2436–2445, 2014. Cited in page 17.

ZHOU, W. et al. A wideband strongly coupled magnetic resonance wireless power transfer system and its circuit analysis. **IEEE Microwave and Wireless Components Letters**, v. 28, n. 12, p. 1152–1154, 2018. Cited in page 8.

ZIOLKOWSKI, R. W.; HEYMAN, E. Wave propagation in media having negative permittivity and permeability. **Phys. Rev. E**, American Physical Society, v. 64, p. 056625, Oct 2001. Cited in page 62.